High wave-vector magnon excitations in ultrathin Fe(111) films grown on Au/W(110) and Fe(001) films grown on Ir(001)

DISSERTATION

zur Erlangung des akademischen Grades

doctor rerum naturalium
(Dr. rer. nat.)
genehmigt durch

Naturwissenschaftlichen Fakultät II - Chemie und Physik
der Martin-Luther-Universität Halle-Wittenberg

vorgelegt von
Herrn Tzu-Hung Chuang
geboren am 20.08.1982 in Taipeh, Taiwan

Gutachter:

1. Prof. Dr. J. Kirschner
2. Prof. Dr. G. Schmidt
3. Prof. Dr. H. Wende

Verteidigungsdatum: 04. 03. 2013

Abstract

In this work, high wave-vector magnon excitations in Fe(111) and Fe(001) ultrathin films are studied using spin-polarized electron energy loss spectroscopy (SPEELS).

To study the role of the lattice structure on the magnon dispersion relation, a metastable phase of Fe composed of a 2 ML Fe film with (111) surface orientation grown on 2 ML Au(111)/W(110) is investigated. The results are compared to the ones of 2 ML Fe(110)/W(110). It is observed that the magnons in Fe(111)/Au(111)/W(110) are softer than the ones in Fe(110)/W(110). First-principles adiabatic spin dynamics calculations show that the softening is due to the fact that the magnetic interactions in Fe are strongly coupled to the lattice structure. The electronic structure is influenced while changing the interlayer spacings and the configuration of the atoms within the lattice. The influence on the electronic structure has a direct consequence on the magnon dispersion relation.

The effect of the Au overlayer on the properties of magnons, e.g. magnon dispersion relation and lifetime, is investigated. A Au overlayer (with a thickness of 1 and 2 ML) is added on top of a 2 ML Fe(110) grown on W(110). It is found that the magnon energies are not effected by the overlayer but the intrinsic linewidth of the magnon peaks is increased, meaning that the magnon lifetime is decreased in the presence of Au overlayer. This observation implies that the Au overlayer provides an additional channel for damping of collective excitations into single particle Stoner excitations.

Investigation of the Fe(001) surface is carried out on epitaxial Fe(001) films grown on Ir(001). The advantage of the Fe/Ir(001) system is that Fe films can be epitaxially grown on Ir(001) up to 10 ML with an uniform film strain and with a negligible in-plane magnetic anisotropy. This would allow us to probe the magnon dispersion relation along different crystallographic axes and also as a function of film thickness. For the first time, the magnon dispersion relation is obtained on a typical ferromagnetic Fe(001) film (with a thickness of 6 ML) over the whole surface Brillouin zone. The results show that the magnon dispersion relation along different symmetry directions is different. It is found that the exchange couplings have a tendency to be antiferromagnetic in each layer, but the layers are strongly ferromagnetically coupled. By comparing the experimental and the theoretical results, we conclude that the strain-induced distortion in the Fe film and the hybridization between the film and the substrate are both crucial to understand this behavior.

The thickness-dependent measurements show that the magnon dispersion relation does not change drastically while changing the film thickness in the regime where the film is uniformly strained (the Fe thickness range of 5-10 ML). The observation is in agreement with our theoretical calculations. The magnon energies stay also nearly unchanged in the vicinity of the thickness of the room temperature ferromagnetic order (5 ML).

Zusammenfassung

In dieser Arbeit wurden Magnonen mit hohen Wellenvektoren in ultradünnen Fe(111) und Fe(001) Filmen mittels spinpolarisierten Elektronenenergieverlustspektroskopie (SPEELS) studiert.

Um die Rolle der atomaren Struktur auf die Magnonendispersionsrelation zu studieren, wurde eine 2 Monolagen (ML) dicke Fe Schicht auf W(110) mit und ohne Au(111)-Puffer-Schicht untersucht. Es wurde beobachtet, dass die Au-Schicht zu einer Abschwächung den Magnonen-Energie führt. Die Ab-initio-Rechnungen zeigen, dass die magnetischen Eigenschaften von Fe sehr stark mit der atomaren Struktur verknüpft sind. Die Änderungen in der atomaren Struktur ändert die elektronische Struktur und dadurch wird die Magnonen-Energie stark reduziert.

Die Einflüsse der Au-Deckschicht auf die Magnonendispersionsrelation und die Lebensdauer wurden untersucht. Eine Au-Deckschicht mit einer Schichtdicke von 1 und 2 ML wurde auf 2 ML Fe(110)/W(110) aufgebracht. Es wurde beobachtet, dass die Magnonen-Energie nicht durch die Au-Schicht beinflusst wird. Es wurde aber herausgefunden, dass die Au-Deckschicht zu einer zusätzlichen Dämpfung der Magnonen in der Fe-Schicht führt.

Untersuchung der Fe(001)-Oberfläche wurde auf epitaktischen Fe(001)-Filmen auf Ir(001) durchgeführt. Zum ersten Mal wurde die Magnonendispersionsrelation auf einem ferromagnetischen Fe(001)-Film mit einer Schichtdicke von 6 ML über die gesamte Oberflächen-Brillouinzone gemessen. Die Ergebnisse zeigen, dass die Magnonendispersionsrelation entlang verschiedener Symmetrie-Richtungen unterschiedlich ist. Es wurde herausgefunden und mit Hilfe Ab-initio-Rechnungen diskutiert, dass obwohl die Austauschkopplungen in jeder Lage eine Tendenz zu einem antiferromagnetischen Zustand haben, sind die Lagen stark ferromagnetisch gekoppelt. Durch Vergleich der experimentellen Ergebnisse mit den theoretischen Rechnungen kommen wir zu dem Schluss, dass die Wachstum induzierte Verzerrung in dem Fe-Film und die elektronischen Hybridisierungen zwischen dem Film und dem Substrat zu diesem Verhalten führt.

Die schichtdickenabhängigen Messungen zeigen, dass die Magnonendispersionsrelation nicht stark von der Schichtdicke abhängig ist (im Schichtdickenbereich von 5-10 ML). Diese Beobachtung wurde mit Hilfe der theoretischen Rechnungen verstanden und diskutiert.

Contents

1 Introduction 1

2 Magnetic excitations 5
- 2.1 Theoretical description of magnetic excitations . . . 5
  - 2.1.1 Description within the Heisenberg model . . . 7
  - 2.1.2 Description within the itinerant electron model . . . 12
- 2.2 Electron scattering . . . 15
- 2.3 Principles of SPEELS . . . 17

3 Experimental Techniques 19
- 3.1 The ultra high vacuum system . . . 19
  - 3.1.1 Low Energy Electron Diffraction . . . 20
  - 3.1.2 Magneto-Optic Kerr Effect . . . 22
- 3.2 Spin-Polarized Electron Energy Loss Spectroscopy . . . 23
  - 3.2.1 SPEEL-spectrometer . . . 23
  - 3.2.2 The GaAs-photocathode . . . 25
- 3.3 Sample preparation and characterization . . . 28
  - 3.3.1 Fe/Au/W(110) . . . 28
  - 3.3.2 Fe/Ir(001) . . . 32

4 Results 35
- 4.1 The Fe/Au/W(110) system . . . 35
- 4.2 The Au/Fe/W(110) system . . . 39
- 4.3 The Fe/Ir(001) system . . . 40
  - 4.3.1 MOKE measurements . . . 41
  - 4.3.2 SPEELS measurements: 6 ML Fe . . . 43
  - 4.3.3 SPEELS measurements: 4-5 ML Fe . . . 46
  - 4.3.4 SPEELS measurements: 1-4 ML Fe . . . 46
  - 4.3.5 SPEELS measurements: 5-10 ML Fe . . . 48
  - 4.3.6 SPEELS measurements: 10-27 ML Fe . . . 50

5 Discussion 53
- 5.1 The Fe/Au/W(110) system . . . 53
  - 5.1.1 Estimation of the effective exchange parameters . . . 53
  - 5.1.2 Description based on the first-principle spin dynamics calculations 57
- 5.2 The Au/Fe/W(110) system . . . 61

5.3 The Fe/Ir(001) system 64
5.3.1 A typical ferromagnetic film: 6 ML Fe/Ir(001) 64
5.3.2 Thickness dependence within the uniformly strained region: 6-10 ML Fe 69
5.3.3 A typical relaxed ferromagnetic film: 27 ML Fe 70

6 Conclusions and outlook **75**

Chapter 1

Introduction

The investigation of magnetic properties of thin films and surfaces has led to important technological applications, such as giant magnetoresistive read heads or magnetic random access memory (MRAM). The switching time of a MRAM cell is determined by the spin dynamics mechanism. Elementary magnetic excitations, magnons, are the quasi-particles, which describe the spin dynamics in solids. Magnons are also of great importance to understand the magnetic ordering phenomenon at a finite temperature [1, 2].

Magnons in ultrathin ferromagnetic films have been studied by ferromagnetic resonance (FMR) [3, 4] and Brillouin light scattering (BLS) [5, 6]. However, both methods have the same limitation; only small wave-vector magnons can be investigated. High wave-vector magnons are of particular interest, since they are governed by the exchange interaction, and they occur on the scales of femtoseconds and nanometers [7, 8, 9]. High wave-vector magnons in bulk Fe have been studied by inelastic neutron scattering (INS) [10, 11], but the weak interaction of neutrons with matter makes the experiment less sensitive such that only very weak signal can be observed for the measurements on ultrathin films [12]. It has been demonstrated that the magnons can be locally excited by inelastic scanning tunneling spectroscopy (ISTS) [13, 14, 15], but it has a limitation in the range of available wave-vectors.

It has been demonstrated that spin-polarized electron energy loss spectroscopy (SPEELS) is a powerful technique to study the high wave-vector magnons in an ultrathin ferromagnetic film up to the surface Brillouin zone boundary. The signature of high wave-vector magnon excitations has been first observed by Kirschner, *et al.* [7] on an ultrathin Fe film. Subsequent studies on Fe thin films have been performed [17, 18]. The excitations have appeared as broad peaks without showing any characteristic dispersion relation. Later on the magnon dispersion relation has been successfully probed along the $\bar{\Gamma}$-$\bar{\mathrm{H}}$ direction on a 2 monolayer[1] (ML) thick Fe(110)/W(110) film [9, 19]. It is found that the exchange interaction in 2 ML Fe(110) is weaker than the one of the bulk Fe. The magnon excitations in a ferromagnetic monolayer have also been studied experimentally [20]. It is found that the magnons are extremely soft. The work has stimulated lots of theoretical investigations [21, 22, 23, 24]. The softening is found to be due to the chemical hybridization and temperature effects [23]. A nonmonotonic thickness dependence of magnon energy in Fe(110) films has been observed indicating

---

[1] The definition of monolayer is given in section 3.3.

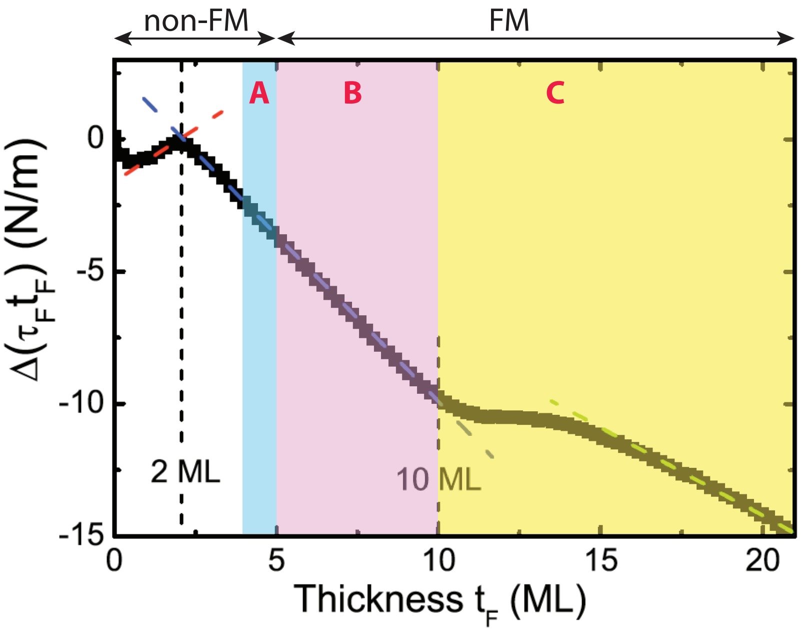

Figure 1.1: Stress measurement during the deposition of an Fe film on Ir(001). The figure is taken from Zhen Tian's dissertation [16]. The SPEELS measurements are divided into three regions based on the lattice structure and the magnetic properties. (A) Transition region from non-ferromagntic (non-FM) to ferromagnetic (FM) film. (B) Ferromagnetic films with a uniform strain. (C) Ferromagnetic film with relaxed structure.

that the hybidization with substrate and the atomic relaxations are both crucial for magnon energies [25].

A simultaneous investigation of phonons and magnons on a prototype oxide surface [an oxygen passivated O/Fe(001)-$p(1\times1)$ surface] has been performed [26]. The influence of the Dzyaloshinskii-Moriya interaction on the magnon dispersion relation and the magnon lifetime has been demonstrated [27, 28].

So far the magnon dispersion relation in ultrathin Fe films has been only observed in Fe(110) films grown on W(110) and along the $\bar{\Gamma}$-$\bar{\mathrm{H}}$ direction [9, 20, 25]. SPEELS measurements performed on the Fe(001)/GaAs(001) and Fe(001)/Ag(001) systems have shown broad peaks and no dispersion relation has been observed [29, 30].

In this work, the magnon dispersion relation in ultrathin Fe(111) and Fe(001) films is measured by SPEELS within the whole surface Brillouin zone. The system for the investigation of Fe(111) surface is chosen to be 2 ML Fe(111)/2 ML Au(111)/W(110). By introducing a 2 ML Au film between the Fe film and W(110) substrate, the surface structure of Fe is changed to (111). The question of interest in this case is: How does the magnon dispersion relation respond to the change of the lattice structure of the film? We compare the results to the ones of the 2 ML Fe(110) film grown on W(110) and comment on the role of the surface structure on the magnon excitations. The obtained magnon dispersion relation is discussed in the Heisenberg model and compared to the first-principles adiabatic spin dynamics calculations based on density-functional theory (DFT) performed by Arthur Ernst at Max Planck Institute of Microstructure Physics.

In addition, the properties of magnons, such as their energy and lifetime, are studied in Au/Fe/W(110) as a function of the Au overlayer. The influence of the non-magnetic Au overlayer on the magnon excitations is discussed.

For the investigation of Fe(001) surface we chose a series of epitaxial Fe(001) films grown on Ir(001). Fe(001) films with a thickness of up to 10 ML grow pseudomorphically on Ir(001) with a constant in-plane film strain [16, 31, 32]. The results of the stress measurement performed by Tian, *et al.*, are shown in Fig. 1.1. The linear-like stress curve between 2 ML and 10 ML exhibits nearly constant slope indicating that the Fe film is uniformly strained. The room temperature ferromagnetic hysteresis loop is observed only above 5 ML [16]. The films show a negligible in-plane magnetic anisotropy. This would allow one to saturate the magnetization of the film along any in-plane direction and probe the magnons perpendicular to that. Deák *et al.* predict that the magnetic ground state of Fe films on Ir(001) for the film thickness below 4 ML is a complex non-collinear structure [33]. However, a direct experimental proof of this prediction is still missing. The questions, which we would like to address within this work, are as following: (*i*) How does the magnon dispersion relation on an Fe(001) surface look like? (*ii*) How does the lattice strain influence the magnon dispersion relation? (*iii*) How do the magnon energies change while changing the film thickness and going across the thickness of room temperature ferromagnetic order? (*iv*) Can one measure the magnetic excitations in the films with no ferromagnetic order (below 4 ML)?

Since there is a rich physics in the Fe/Ir(001) system. we divide our experiments into four parts. (I) For simplicity we start with an epitaxially grown ferromagnetic film with a nominal thickness of 6 ML (region B in Fig. 1.1). We also discuss the effect of the film thickness on the magnon dispersion relation within this region (5-10 ML). (II) We probe the magnon dispersion relation for thinner films and go across the onset of room temperature ferromagnetic order (region A in Fig. 1.1). (III) We also measure the SPEEL-spectra for 1-4 ML Fe and carefully trace the signal of magnetic excitations. (IV) Finally, we probe the magnon dispersion relation on the surface of a thick Fe film (19-27 ML). We also comment on the properties of the films in the intermediate regime (10-19 ML) where the films relax from a body-centered tetragonal (bct) to a body-centered cubic (bcc) structure (region C in Fig. 1.1).

This work is organized as following. In Chapter 2, an introduction to magnetic excitations and their theoretical description is given. It also includes a short introduction to the principle of the electron scattering and SPEELS. In Chapter 3, the experimental techniques are presented including the SPEEL-spectrometer and other characterization tools. The sample preparation and characterization are also shown in Chapter 3. In Chapter 4, the experimental results of SPEELS measurements are presented. The discussion of the results and a comparison to the theoretical calculations are given in Chapter 5. Finally, the conclusions are summarized in Chapter 6.

Chapter 2

Magnetic excitations

In this chapter, the basic concepts are discussed. The chapter is divided into three sections. In the first section, two theoretical descriptions of magnetic excitations are introduced. This section focuses on the magnons, since these are the subject of this work. Descriptions based on the Heisenberg model and the itinerant electron picture are discussed. In the second section, an introduction to the electron scattering process is given. It is dedicated to the magnetic excitations probed by inelastic electron scattering experiments. In the last section, the principles of SPEELS are introduced.

2.1 Theoretical description of magnetic excitations

Magnetic excitations in solids that involve a reversal of an electron spin are divided into two types; single particle and collective excitations. In the case of spin-dependent single particle excitations, which are referred to as Stoner excitations, the spin of a single electron is reversed. In the case of collective excitations, which are referred to as spin waves, the spin flip is distributed over the entire ensemble of electrons.

Similar to other collective phenomena in solids, such as collective lattice vibration and the collective charge oscillation, spin waves are quantized. The quantized lattice vibrations are phonons and the ones of charge oscillations are plasmons. In literature, the quantum of spin waves is often called magnon. In fact the magnons refer to a more general term including single particle Stoner excitations as well as collective excitations. A magnon carries a wave vector $\vec{\mathrm{q}}$, an energy ε, an angular momentum of $1\hbar$, and a magnetic moment of $1\mathrm{g}\mu_B$, which could be considered as a spin reversal in the system. In this work, we use the term "magnons" as a representative quasi-particle of both spin waves and Stoner excitations.

Since a spin itself produces a dipolar magnetic field, one may think that two spins could be coupled by a dipole-dipole interaction, which ranges over a long distance. But this interaction is relatively weak (It leads to magnetic order at temperatures below 1 K [34]). Since magnetic order is observed at much higher temperature, a stronger interaction between spins is expected. It was found by Heisenberg that the strong interaction between spins is caused by the exchange interaction, which is an outcome of the Pauli exclusion principle and the fact that electrons with the same spin character are indistinguishable [35]. It leads to a symmetrization requirement that the total wave function of a two electron system should be antisymmetric under the exchange of the two

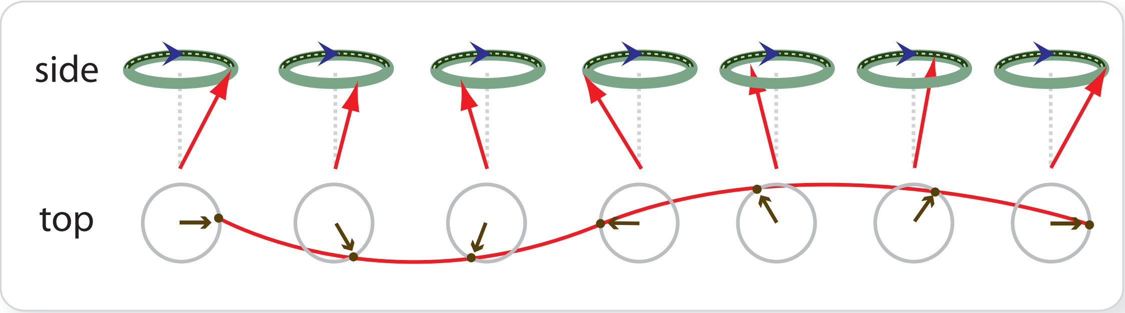

Figure 2.1: The side and the top view of a spin wave in a classical picture. Each spin is slightly canted out of its equilibrium position and precesses around it. The wave-vector of the spin wave determines the phase relation between the neighboring spins.

identical electrons. However, the wave function of electrons can be written as a product of the spatial part and the spin part. Therefore, the symmetry of the wave function in spin space affects the one in the real space. The spatial wave function with different symmetries results in the different spatial distributions of the electrons and accordingly in different electrostatic energies due to the Coulomb interaction. Although the driving force is the strong electrostatic force rather than a weak dipole-dipole interaction, it only ranges over a short distance because the exchange interaction is based on the possibility that two electrons can physically exchange which requires an overlap of the wave function of the electrons.

Magnons have a characteristic dispersion relation, which relates their energy to the wave-vector. In different wave-vector regimes, different magnetic interactions determine the magnon energy. As discussed above, the exchange interaction is typically much stronger than other magnetic interactions. However, in the sufficiently small wave vectors, the long-ranged dipolar interaction could be dominant due to the short-ranged character of the exchange interaction [36]. In $3d$-ferromagnets, for wave vectors below 10^{-3} Å^{-1}, the dipole-dipole interaction is prevailing. For wave vectors above 10^{-2} Å^{-1}, the exchange interaction can be safely assumed the only interaction determining the magnon energy [36].

For different regimes, different theoretical methods are applied to describe the magnons. In the regime in which exchange interaction is dominating, a microscopic description is needed since the wavelength is comparable to the atomic distance in a crystal. The wave-vector studied in this work is typically from 0.4 Å^{-1} to 1.2 Å^{-1}, which corresponds to the wavelength from 5 Å to 16 Å. Therefore, the following theoretical descriptions will then focus on the exchange dominated regime. Two different approaches have been developed: the classical Heisenberg model based on the localized magnetic moments approximation and the itinerant electron model, where the moments are carried by delocalized electrons.

2.1.1 Description within the Heisenberg model

In the Heisenberg model, magnons are treated as a synchronic precession of the spin moments in the magnetic ordered system based on the localized moment picture. This is schematically shown in Fig. 2.1. Each spin is slightly tilted out of its equilibrium position and precesses around it with a constant phase difference between the neighboring spins. The wave vector of the magnon determines the phase relation. The energy due to the exchange interaction can be described by the Heisenberg Hamiltonian:

$$\mathrm{H} = -\sum_{\mathrm{ij}} \mathrm{J}_{\mathrm{ij}} \vec{\mathrm{S}}_{\mathrm{i}} \cdot \vec{\mathrm{S}}_{\mathrm{j}}, \tag{2.1}$$

where J_{ij} is the exchange coupling constant between the spins $\vec{\mathrm{S}}_{\mathrm{i}}$ and $\vec{\mathrm{S}}_{\mathrm{j}}$. The positive J_{ij} indicates a ferromagnetic coupling.

The exchange interaction is determined by the overlap of the electron wave functions. In the case of $3d$ transition metals, the d electrons are relatively localized, so the overlap decays very fast with the increase of the distance between two sites [37]. Therefore, in this model, one may only consider the exchange interaction between the first nearest neighbors and the second nearest neighbors. This will be taken into account in the discussion concerning the magnon dispersion relation of Fe thin films.

In the following, the spins are treated as classical vectors to derive the magnon dispersion relation in the Heisenberg Hamiltonian (Eq. 2.1). Here, we only consider the spin moment since the orbital moment is assumed to be quenched in the crystal [38]. Therefore, each atom carries the magnetic moment $\vec{\mu}_{\mathrm{i}} = -\mathrm{g}\mu_{\mathrm{B}}\vec{\mathrm{S}}_{\mathrm{i}}$. The energy of the magnetic moment $\vec{\mu}_{\mathrm{i}}$ in a magnetic field $\vec{\mathrm{B}}$ is given by $-\vec{\mu}_{\mathrm{i}} \cdot \vec{\mathrm{B}}$. The exchange coupling between neighbors can be taken as an effective field $\vec{\mathrm{B}}_{\mathrm{i}}^{\mathrm{effect}}$. Consequently, according to Eq. 2.1,

$$\vec{\mathrm{B}}_{\mathrm{i}}^{\mathrm{effect}} = -\frac{2}{\mathrm{g}\mu_{\mathrm{B}}} \sum_{\mathrm{j}} \mathrm{J}_{\mathrm{j}} \vec{\mathrm{S}}_{\mathrm{j}}. \tag{2.2}$$

The factor 2 results from the fact that the sum in Eq. 2.1 runs twice over the pair of spins. In the effective field $\vec{\mathrm{B}}_{\mathrm{i}}^{\mathrm{effect}}$, the spin $\vec{\mathrm{S}}_{\mathrm{i}}$ experiences a torque $\vec{\tau}_{\mathrm{i}} = \vec{\mu}_{\mathrm{i}} \times \vec{\mathrm{B}}_{\mathrm{i}}^{\mathrm{effect}}$ which makes the spin precess. The sum of the torques defines the rate of the change of the angular momentum $\hbar\vec{S}$:

$$\hbar\frac{\mathrm{d}\vec{\mathrm{S}}_{\mathrm{i}}}{\mathrm{dt}} = \vec{\tau}_{\mathrm{i}} = -\mathrm{g}\mu_{\mathrm{B}} \sum_{\mathrm{j}} \vec{\mathrm{S}}_{\mathrm{i}} \times \vec{\mathrm{B}}_{\mathrm{i}}^{\mathrm{effect}} = 2\sum_{\mathrm{j}} \mathrm{J}_{\mathrm{j}} (\vec{\mathrm{S}}_{\mathrm{i}} \times \vec{\mathrm{S}}_{\mathrm{j}}). \tag{2.3}$$

We define the direction of the z-axis as parallel to the magnetization axis, and assume that the magnetic moments only slightly deviate from the z-axis. Therefore, the expansion of the Eq. 2.3 can be expressed as

$$\hbar\frac{\mathrm{dS}_{\mathrm{i}}^{\mathrm{x}}}{\mathrm{dt}} = 2\sum_{\mathrm{j}} \mathrm{J}_{\mathrm{j}} (\mathrm{S}_{\mathrm{i}}^{\mathrm{y}}\mathrm{S}_{\mathrm{j}}^{\mathrm{z}} - \mathrm{S}_{\mathrm{j}}^{\mathrm{y}}\mathrm{S}_{\mathrm{i}}^{\mathrm{z}}) \tag{2.4}$$

and

$$\hbar\frac{\mathrm{dS}_{\mathrm{i}}^{\mathrm{y}}}{\mathrm{dt}} = 2\sum_{\mathrm{j}} \mathrm{J}_{\mathrm{j}} (\mathrm{S}_{\mathrm{j}}^{\mathrm{x}}\mathrm{S}_{\mathrm{i}}^{\mathrm{z}} - \mathrm{S}_{\mathrm{i}}^{\mathrm{x}}\mathrm{S}_{\mathrm{j}}^{\mathrm{z}}). \tag{2.5}$$

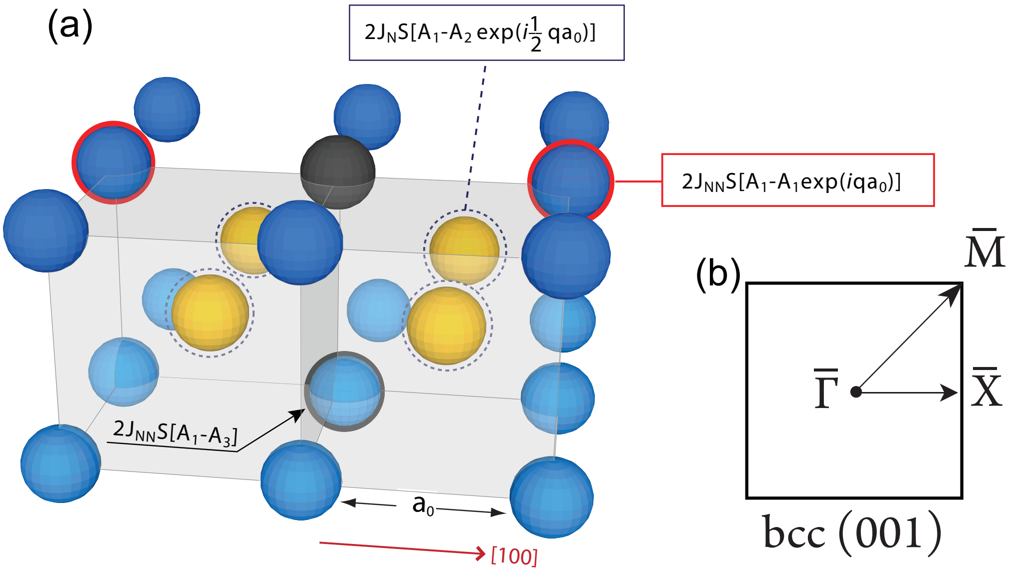

Figure 2.2: (a) The illustration of Eq. 2.7 for a bcc crystal with (001) surface. The blue balls represent the first and the third layer and the yellow balls are at the second layer. The wave-vector, $\vec{q}$, is along the [100] direction. (b) The surface Brillouin zone of a bcc(001) crystal.

We can assume $\mathrm{S^z}$ is approximately the same as S, which is the value of the spin moment of $\vec{\mathrm{S}}_\mathrm{i}$ and $\mathrm{S^x}$, $\mathrm{S^y}$ are much smaller than S. In addition, the two equations can be coupled by choosing $\mathrm{S^+ = S^x} + i\mathrm{S^y}$. We then obtain

$$i\hbar\frac{\mathrm{dS_i^+}}{\mathrm{dt}} = 2\mathrm{S}\sum_\mathrm{j}\mathrm{J_j(S_i^+ - S_j^+)}. \tag{2.6}$$

In order to derive the dispersion relation of magnons, Eq. 2.6 can be solved by using the ansatz $\mathrm{S^+ = A_i exp}(i(\vec{\mathrm{q}}\cdot\vec{\mathrm{R}}_\mathrm{i} - \omega\mathrm{t}))$, where $\vec{\mathrm{q}}$ and ω denote the wave vector and the angular frequency of magnons, respectively. $\mathrm{A_i}$ is the amplitude of the magnon at the position $\vec{\mathrm{R}}_\mathrm{i}$. Inserting $\mathrm{S^+}$ into Eq. 2.6 and dividing the result by $\mathrm{exp(i(}\vec{\mathrm{q}}\cdot\vec{\mathrm{R}}_\mathrm{i} - \omega\mathrm{t}))$, we then obtain

$$\hbar\omega\mathrm{A_i} = \sum_\mathrm{j} 2\mathrm{J_jS(A_i - A_j}e^{i(\vec{\mathrm{q}}\cdot(\vec{\mathrm{R}}_\mathrm{j}-\vec{\mathrm{R}}_\mathrm{i}))}). \tag{2.7}$$

Equation 2.7 can be used as a starting point to derive the magnon dispersion relation in an arbitrary crystalline structure. In this work, magnon excitations in bcc-Fe films with (001) surface and fcc-Fe precursor with (111) surface are investigated. Thus, as an example, we first calculate the magnon dispersion relation of a semi-infinite bcc crystal with (001) surface along the [100]-direction.

In a bcc crystal, there are 8 nearest neighbors in the bulk at $(\frac{a_0}{2}, \frac{a_0}{2}, \frac{a_0}{2})$, where a_0 is the lattice constant, and 6 second nearest neighbors at $(a_0, 0, 0)$ (see Fig. 2.2). The amplitude of the magnons is constant in the same layer and differs between each layers. Therefore, we introduce a layer index n, where $n = 1$ represents the surface or the topmost layer. Here, we will consider both the nearest neighbors and the second nearest neighbors. $\mathrm{J_N}$ denotes the exchange coupling constant between the nearest

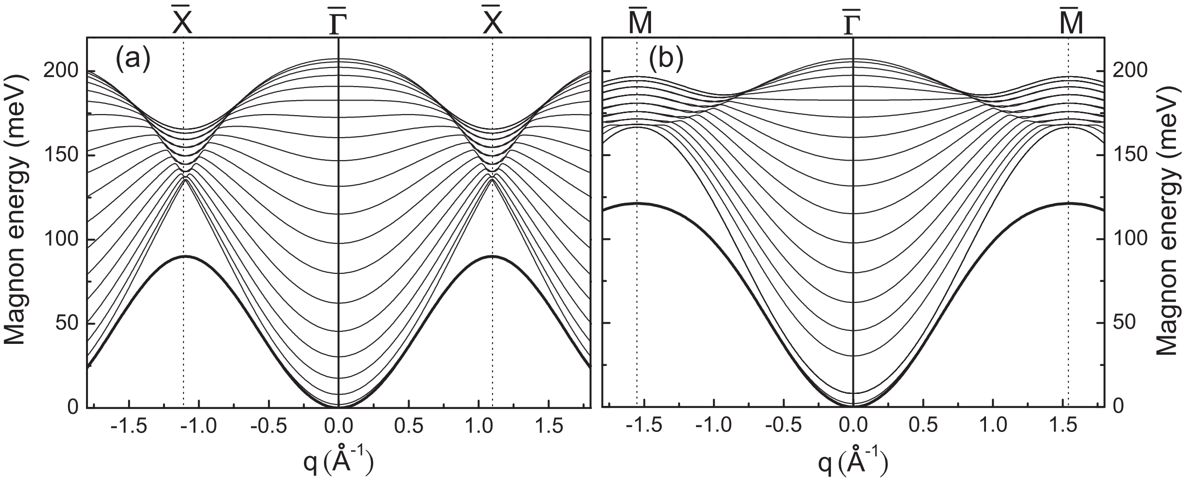

Figure 2.3: The magnon dispersion relation calculated within the Heisenberg model considering only the first and the second nearest neighbors for a 20 ML slab of bcc crystal with a (001)-surface along (a) [100]- ($\bar{\Gamma}$-$\bar{\mathrm{X}}$) and (b) [110]- ($\bar{\Gamma}$-$\bar{\mathrm{M}}$) directions. In these calculations, the exchange constants are J_NS= 6.8 meV and $J_{NN}S$= 4.1 meV for the nearest and the second nearest neighbors. The lattice constant is a_0= 2.866 Å. The lowest curves are the surface acoustic modes.

neighbors, and $\mathrm{J_{NN}}$ denotes the one between the second nearest neighbors. In the following, $\alpha = \cos(\frac{\mathrm{qa_0}}{2})$ and $\beta = \cos(\mathrm{qa_0})$. Then, we derive from Eq. 2.7:

$$n = 1 : \hbar\omega \mathrm{A_1} = \{8\mathrm{J_NS} + 2\mathrm{J_{NN}S}(3 - 2\beta)\}\mathrm{A_1} + \{-8\mathrm{J_NS}(\alpha)\}\mathrm{A_2} + \{-2\mathrm{J_{NN}S}\}\mathrm{A_3} \tag{2.8}$$

$$\begin{aligned} n = 2 : \hbar\omega \mathrm{A_2} &= \{-8J_NS(\alpha)\}A_1 + \{16J_NS + 2J_{NN}S(3 - 2\beta)\}A_2 \\ &\quad + \{-8J_NS(\alpha)\}A_3 + \{-2J_{NN}S\}A_4 \end{aligned} \tag{2.9}$$

$$\begin{aligned} n > 2 : \hbar\omega \mathrm{A_n} &= \{-2J_{NN}S\}A_{n-2} + \{-8J_NS(\alpha)\}A_{n-1} \\ &\quad + \{16J_NS + 2J_{NN}S(4 - 2\beta)\}A_n + \{-8J_NS(\alpha)\}A_{n+1} \\ &\quad + \{-2J_{NN}S\}A_{n+2} \end{aligned} \tag{2.10}$$

These equations can be summarized in the form:

$$\begin{pmatrix} a_1 & b & c & & & & 0 \\ b & a_2 & b & c & & & \\ c & b & a_n & b & c & & \\ & c & b & a_n & b & c & \\ 0 & . & . & . & . & . & . \end{pmatrix} \begin{pmatrix} A_1 \\ A_2 \\ A_3 \\ . \\ . \\ A_n \\ . \end{pmatrix} = 0. \tag{2.11}$$

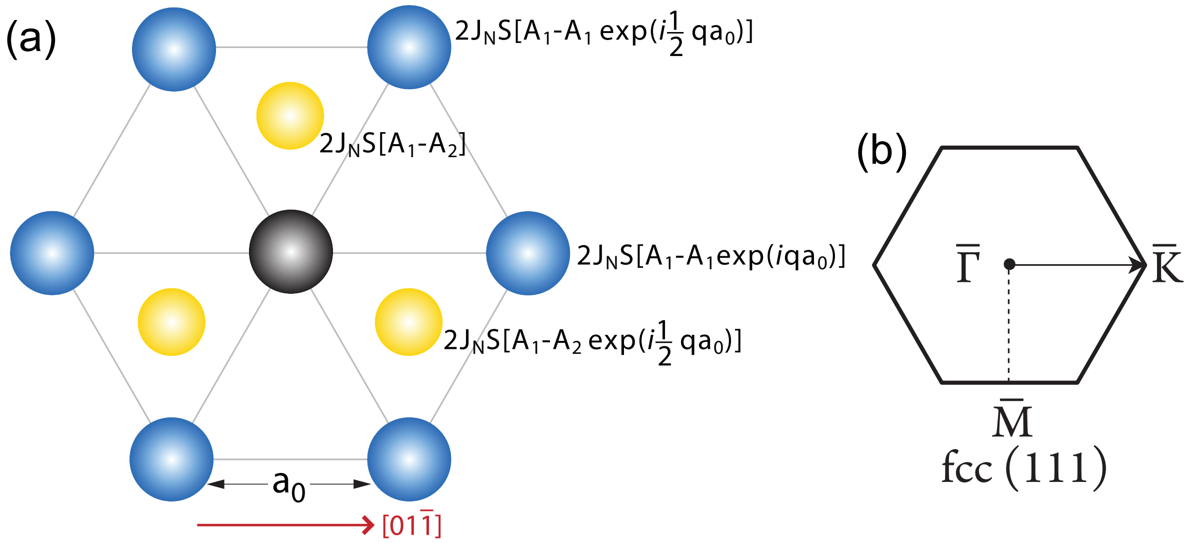
(a)
2J$_N$S[A$_1$-A$_1$ exp($i\frac{1}{2}$ qa$_0$)]
2J$_N$S[A$_1$-A$_2$]
2J$_N$S[A$_1$-A$_1$exp($i$qa$_0$)]
2J$_N$S[A$_1$-A$_2$ exp($i\frac{1}{2}$ qa$_0$)]
a$_0$
[01$\bar{1}$]
(b)
$\bar{\Gamma}$
$\bar{K}$
$\bar{M}$
fcc (111)

Figure 2.4: (a) The illustration of Eq. 2.7 for a 2 atomic layer thick ferromagnetic film with fcc(111) surface. The blue balls represent the first layer and the yellow balls are at the second layer. The wave-vector, $\vec{q}$, is along the [01$\bar{1}$] direction. (b) The surface Brillouin zone of an fcc(111) crystal.

Here, $a_n = -\hbar\omega + 16J_NS + 2J_{NN}S(4-2\beta)$, $b = -8J_NS(\alpha)$, $c = -2J_{NN}S$, $a_1 = a_n - 8J_NS - 2J_{NN}S$, $a_2 = a_n - 2J_{NN}S$. They are linear equations with the variables $A_1 ... A_n$ which represent the magnon amplitude in each layer. The magnon energy $\hbar\omega$ is the eigenvalue of this matrix. For obtaining the dispersion relation, the eigenvalues are numerically calculated for each $\vec{q}$. The similar procedure applies to the other in-plane direction ([110]-direction). In Fig. 2.3, the magnon dispersion calculated for a 20 ML slab of a bcc(001) crystal along (a) [100]- ($\bar{\Gamma}$-$\bar{X}$) and (b) [110]- ($\bar{\Gamma}$-$\bar{M}$) directions is presented. In the calculations, the exchange constants are J_NS= 6.8 meV and $J_{NN}S$= 4.1 meV for the nearest and the second nearest neighbors. The lattice constant is set to be a_0= 2.866 Å, which is the bulk Fe value. The reason for choosing these exchange parameters is because later on we will discuss the experimental results obtained on a relaxed Fe(001) film grown on Ir(001) substrate. These parameters are the best fit to the experiment. For the system of 20 ML, 20 dispersion curves can be obtained for this system. For any given $\vec{q}$, 20 eigenvectors can be obtained with respect to the 20 eigenvalues, respectively. Each eigenvector consists of the magnon amplitudes ($A_1 ... A_n$) in each atomic layer. They reveal the precession amplitudes of the spins in these 20 layers.

The magnon branch, in which the magnon energy goes to zero when $\vec{q} = 0$, is called acoustic branch. For all other modes, the magnetic moments in some layers precess in an out-of-phase condition compared to the magnetic moments in other layers. Therefore, these modes always have a finite magnon energy at $\vec{q} = 0$. They are called optical modes.

For the investigation of Fe(111) surface, the system we chose is the 2 ML Fe(111)/2 ML Au(111)/W(110). The detailed reason will be discussed in section 3.3. In this system, only two layers of Fe are considered in the Heisenberg model. An analytical description of the magnon mode can be obtained. In Fig. 2.4, the center atom and its

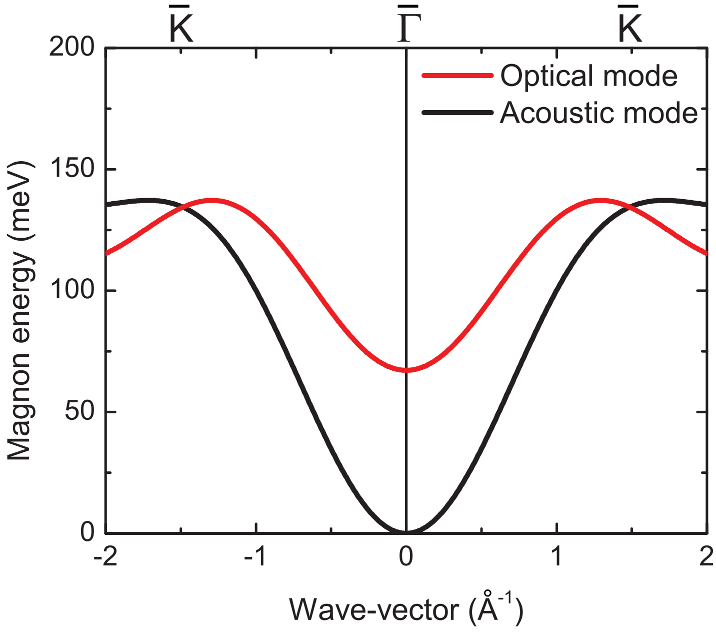

Figure 2.5: The magnon dispersion relation calculated for a two-layer slab of fcc(111) structure based on the nearest neighbor Heisenberg model. The exchange constants are $J_N S$= 5.6 meV for only considering the first nearest neighbors. The lattice constant is a_0= 2.82 Å. The acoustic and optical modes are shown as black and red curves, respectively. These are the dispersion curves calculated from Eq. 2.16 and Eq. 2.17. The wave-vector is along the $[01\bar{1}]$ direction.

9 nearest neighbors are in a film consists of 2 atomic layers in (111) structure. Starting from the Eq. 2.7, and doing the summation of nine terms in Fig. 2.4, one gets the expression as:

$$\hbar\omega \mathrm{A_1} = \{2\mathrm{J_N S}[9 - 4\alpha - 2\beta]\}\mathrm{A_1} - \{2\mathrm{J_N S}[2\alpha + 1]\}\mathrm{A_2} \tag{2.12}$$

for the first atomic layer. Similarly, for the second layer we have:

$$\hbar\omega \mathrm{A_2} = -\{2\mathrm{J_N S}[2\alpha + 1]\}\mathrm{A_1} + \{2\mathrm{J_N S}[9 - 4\alpha - 2\beta]\}\mathrm{A_2}. \tag{2.13}$$

Eq. 2.12 and Eq. 2.13 can be combined as:

$$\hbar\omega \begin{pmatrix} A_1 \\ A_2 \end{pmatrix} = \begin{pmatrix} 2J_N S[9-4\alpha-2\beta] & -2J_N S[2\alpha+1] \\ -2J_N S[2\alpha+1] & 2J_N S[9-4\alpha-2\beta] \end{pmatrix} \begin{pmatrix} A_1 \\ A_2 \end{pmatrix}. \tag{2.14}$$

In Eq. 2.14, the magnon energy $\hbar\omega$ can be taken as the eigenvalue of the coefficient matrix on the right side. In this case, an analytical expression for $\hbar\omega$ can be obtained. This requires:

$$\begin{vmatrix} -\hbar\omega + 2J_N S[9-4\alpha-2\beta] & -2J_N S[2\alpha+1] \\ -2J_N S[2\alpha+1] & -\hbar\omega + 2J_N S[9-4\alpha-2\beta] \end{vmatrix} = 0. \tag{2.15}$$

The solutions of Eq. 2.15 are:

$$\hbar\omega = 4\mathrm{J_N S}[4 - \cos(\mathrm{qa_0}) - 3\cos(\frac{1}{2}\mathrm{qa_0})] \tag{2.16}$$

and

$$\hbar\omega = 4\mathrm{J_N S}[5 - \cos(\mathrm{qa_0}) - \cos(\frac{1}{2}\mathrm{qa_0})]. \tag{2.17}$$

They describe the acoustic and optical modes of magnons in the two-atomic layer film with (111)-surface orientation. The two modes are plotted in Fig. 2.5 for $J_N S$= 5.6 meV and a_0 = 2.82 Å.

The Heisenberg model is valuable because of its simplicity. It is not expected to be applicable to an itinerant electron system. However, it has been shown that the results obtained on Co are described surprisingly well by this model [8, 39, 40, 41]. But other findings can only be understood in an itinerant electron description. Therefore, an introduction to magnetic excitations in an itinerant electron model is given in the next subsection.

2.1.2 Description within the itinerant electron model

For the 3*d*-magnetic metals, the conduction electrons have to be considered as freely moving in a periodic potential. This leads to a description of electrons which are arranged in bands. Each electron is located in k-space rather than at a localized position in the real space (crystal). The successful description of magnetism in itinerant electron system originated from Stoner [42, 43]. Under the Stoner criterium, it is energetically favorable to arrange itinerant electrons in exchange split bands. This results in a higher occupation of states for electrons of one spin direction compared to the other one. Hence, the net spin moments are not zero and the system is magnetic. The interaction responsible for the magnetic order is the exchange interaction. The Stoner criterium is fulfilled for Fe, Co, and Ni. It explains why these elements have ferromagnetic order, but other 3*d*-metals do not.

The magnetic excitations allowed in the model are the Stoner excitations. In these excitations, an electron of a given spin hops from an occupied state below the Fermi-level (E_F) into an empty state above E_F with opposite spin, leaving a hole behind. In the Stoner model, no interaction between the excited electron and the hole is considered. This results in an overestimation of the minimum energy for magnetic excitations. The consideration of low energy collective excitations within the itinerant electron model are needed to describe the experimentally observed Curie temperature. Collective excitations have been introduced by Slater for an itinerant electron insulator, where all spins are all aligned parallel to each other except one [44]. It has been found that the lowest energy of such system are of collective nature. This state can be described by the superposition of single particle states and represents the correlated motion of the electron and the hole with opposite direction [45]. The correlated electron-hole pair has a spin moment of 1gμ_B and a defined wave-vector. It is found that its magnetic properties are similar to the magnon excitations in the localized model [44].

At high wave-vectors and energies, Stoner excitations are possible in the system. A correlated electron-hole pair which is created in the region where Stoner excitations are possible can easily decay into the uncorrelated states. In this case, the collective excitations are not well-defined spin waves with a long living lifetime. They are strongly damped [46].

The general concept of magnetic excitations in itinerant ferromagnets is illustrated

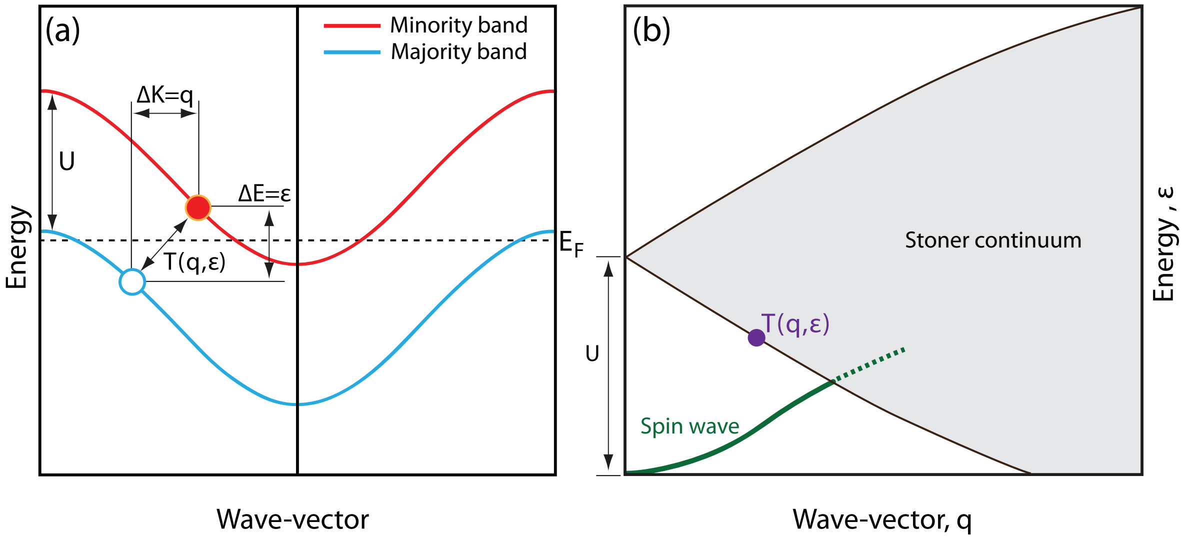

Figure 2.6: Schematic illustration of Stoner excitations of the majority-hole with minority-electron states in a weak ferromagnet. (a) A Pair of exchange split bands with the splitting parameter U (it is assumed to be constant in the entire Brillouin zone). The Stoner excitation T(q,ε) is a state with a majority hole (blue open circle) under the Fermi-level and a minority electron (red solid circle) above the Fermi-level. (b) The gray region shows the Stoner continuum calculated for the band shown in (a). At q=0, the creation of a Stoner excitation costs an energy which is equal to U. To give a general idea, a possible spin wave dispersion relation is also presented in (b) as a green line. In the intersection between spin wave dispersion relation and the Stoner continuum, spin waves strongly decay into the Stoner excitations.

in Fig. 2.6. In Fig. 2.6 (a), a simple representation of one pair of exchange split bands is presented. The exchange splitting is assumed to be identical to U over the whole Brillouin zone. Due to a weak ferromagnet, the majority band is not completely filled, and the minority band is empty except for the part near the Brillouin zone center. In the itinerant electron system, Stoner excitations are the electron-hole pair excitations with electrons and holes in the bands of opposite spins. The majority-hole with minority electron state is illustrated as the excited state T(q,ε) in Fig. 2.6 (a). Instead of the dispersion relation, the relation of energy ε and momentum q for the Stoner excitations shows a continuum in the energy-momentum space. The state T(q,ε) corresponds to the dot in Fig. 2.6 (b). The energy and wave-vector transfer needed to excite an electron from an occupied majority state to an unoccupied minority state is shown in Fig. 2.6 (b) as a gray region. In this gray region, spin-dependent single particle excitations are possible.

Since the band splitting is assumed to be uniform over the Brillouin zone, the energy distribution of the Stoner excitations converges to one point, q=0. This corresponds to the Stoner state with the majority hole locates vertically under the minority electron in Fig. 2.6. The energy of these states is equal to the band splitting U. A possible acoustic spin wave mode is also shown in Fig. 2.6 (b) as a green line. When the spin wave branch enters the Stoner continuum, it is strongly damped. Similar to the spin wave excitations, this kind of Stoner state corresponds to a spin-flip of a majority electron in the system. In the range of small wave-vector and low energy range, it is not allowed to have single-particle Stoner excitations. In this case, the Stoner excitations of wave-vector q can produce collective excitations, or spin waves, of wave-vector q at low energies.

The real situation is only partly described in Fig. 2.6. For example, realistic band structures in real $3d$ transition metals consist of more than one band across the Fermi-level. For the investigation of magnons at surfaces by electron scattering, additional effects may be considered. It has been theoretically predicted that in inelastic electron scattering the creation of free electron like Stoner excitations is likely a creation of d-electron Stoner excitation [47]. Moreover, the wave-vector perpendicular to the surface is not conserved due to the lack of translational invariance. This leads to the fact that even at the small wave-vector, magnons can decay into Stoner excitations [48, 49, 50, 51]. The Stoner continuum in a real metal may be quite different from the one shown in Fig. 2.6.

The elementary magnetic excitations in ferromagnets can be classified as spin waves and Stoner excitations. The theory of the spin wave states in a metal has been developed by Herring and Kittel [2, 52]. The general finding is that collective excitations exist in an itinerant electron system and they are identical to the well-defined spin waves in a localized model in the limit of low wave-vector and low energies. In this limit, a quadratic dispersion relation of the excitations was found [2, 52].

However, this approach throws no light on the relation between spin wave theory and collective electron theory. The relation between localized and collective modes has been discussed by Edwards *et al.* [53, 54, 55, 56, 57, 58] that spin waves could be described as a number of exciton-like excitations, where an electron of minority spin is bound to a hole of majority spin. Spin-wave states may be derived from any low-lying band-type state of a ferromagnetic metal. A typical low-lying state differs from the ground state by a number of independent single particle excitations. The wave function of the spin wave is a linear superposition of particle hole states. As it is mentioned above, at low wave-vector region, the configuration of the electronic bands does not allow Stoner excitations. In this case, the coherent superposition of the Stoner states can produce a collective modes at low energies.

In addition to spin waves, a spectrum of single particle Stoner excitation can also be obtained. Mills *et al.* [59, 60, 61] discuss the spin excitations of a simple model of an ultrathin ferromagnetic film, where the magnetic moment bearing electrons are itinerant in character. The one-band Hubbard model is treated in mean-field theory. Muniz, Costa, and Mills [62, 63, 64, 65] use an itinerant model of electrons as the basis. The bands are described within an empirical tight-binding scheme, and the ferromagnetic ground state is generated from on-site intra-atomic Coulomb interactions, described in mean-field theory. The random phase approximation is employed to describe the spin excitations through analysis of the wave-vector and frequency dependence of the dynamic transverse susceptibility.

Since the properties of collective magnetic modes and single electron spin flip are sensitive to the electronic structure, a state-of-the-art ab initio technique is important to make a quantitative prediction. A proper description of the hybridization of these two types of excitations is necessary to describe correctly the Landau damping of magnons. It has been demonstrated by Buczek *et al.* [24, 66, 67, 68] that an adequate tool for the parameter-free microscopic studies of the energies and lifetimes of magnetic excitations is the calculation of the dynamic magnetic spin susceptibility based on the linear response density functional theory [69].

2.2 Electron scattering

Since SPEELS is an experimental technique based on the spin-dependent electron scattering, here we give a brief introduction to it. The discussion in this section is limited to the low energy ($\approx$ 10 eV) electrons scattered from crystalline metallic surfaces. The surface sensitivity of electron spectroscopy is due to the small inelastic mean free path of low energy electrons. This originates from the strong interaction of the electrons with the solid, which is mediated by few energy loss mechanisms including phonon, plasmon, and magnon excitations. This is the main reason why electrons have been used extensively in almost all kinds of surface studies [70]. At low energies, the possible excitations are phonon excitations, vibrations of adsorbates on the surface, electron-hole pair excitations, and spin wave excitations. The first three excitations have been studied by electron energy loss spectroscopy (EELS) for decades [71]. The surface sensitivities of EELS can be used to study the vibrational excitations of tiny amounts of adsorbates on surfaces. Here, we focus on the magnetic excitations by inelastic scattering. These excitations can be analyzed by taking an energy spectrum of the scattered electrons.

The individual loss mechanism is also reflected in the angular distribution of the inelastically scattered electrons. Around the direction of the specular reflection, one finds the so-called dipolar cone. These are electrons which have the energy loss with a rather small momentum transfer. They are scattered from long-ranged electric dipolar fields caused by charge density fluctuation due to elementary excitations in the solid. These excitations may be optical phonons, plasmons, or the vibrational excitations of adsorbates. Due to the long range interaction of the dipolar field, the scattering typically takes place long before the electron reached the surface. Therefore, it is sufficient to describe this scattering by macroscopic quantities [71].

Besides the dipolar scattering with small momentum transfer, another scattering at rather high scattering angle is also found and corresponds to a large momentum transfer. This is the regime of so-called impact scattering. The impact scattering process is caused by short-range interactions within the surface. The description of the impact process demands a truly microscopic model [71]. In contrast to the dipolar scattering mechanism, the impact scattering requires the electrons to enter the solid before any energy loss event can occur. Because of the close distance between the incoming electrons and the electrons in the sample, exchange processes are possible in this regime. The dominant elementary excitation in this regime is the electron-hole pair excitations due to electronic interband transitions.

The complete process of inelastic scattering of the spin-polarized electrons is rather complicated. Detailed information could be found in Ref. [72, 73, 74]. Here we only assume a simple situation: an electron with a given energy, $\mathrm{E_i}$, and spin direction (up $\uparrow$ and down $\downarrow$) is shot onto a ferromagnetic surface. The scattered electrons are analyzed with their energy and spin direction. Here only in the case of the incidence of spin-down electrons is shown. The case of the incidence of spin-up electrons is similar. Four

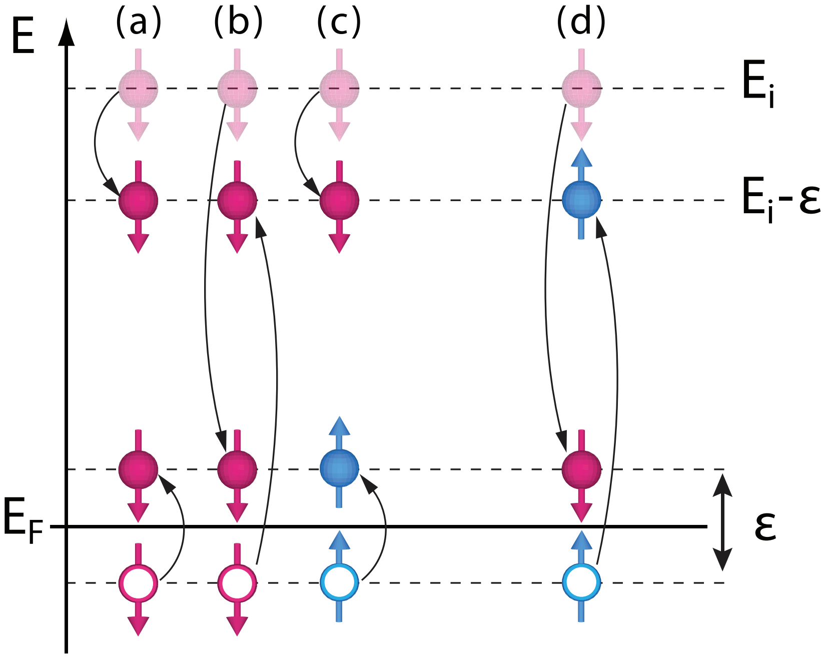

Figure 2.7: Schematic representation of inelastic exchange scattering processes associate with electron-hole pair generation for the incidence of spin down electrons. The solid balls represent the electrons with up (blue) and down (red) spins. The open circles denote the holes left in the system. E_F and E_i are the Fermi energy and incident electron energy, respectively. ε is the energy loss of electrons in the scattering process. (a) and (b) show that the incident spin-down electrons are scattered by the same spin-down electrons without and with the exchange of electrons. (c) and (d) show the scattering by the spin-up electrons without and with the exchange of electrons. The spin of the outgoing electrons is not changed in (a), (b) and (c), which are indicated as non spin-flip processes. Only in (d), the spin of the scattered electron is flipped as compared to the spin orientation of the incident electron. An incident electron with minority character occupies a state above the Fermi level, and an electron with majority character from a state below the Fermi level is scattered out.

configurations of the inelastic exchange scattering process for the incidence of spin-down electrons are shown in Fig. 2.7. A spin-down electron with the energy of E_i is shot onto the surface and the electron with the energy of $E_i - \varepsilon$ is scattered out with either spin-down orientation ((a)-(c)) (non-flip process) or spin-up orientation (d) (flip process). ε is the energy loss of electrons in the scattering process. In Fig. 2.7 (a) (c), the incident spin-down electron transfers the energy ε to the other spin-down (spin-up) electron below the Fermi level and excite it to the state above Fermi level and scattered out without any exchange process. In (b), the incident spin-down electron occupies a state above Fermi level and transfer the energy to the other one and the other spin-down electron is scattered out with an exchange process. Only in (d), a spin-flip process with the exchange of electrons is shown. A detail discussion is in the following section.

2.3 Principles of SPEELS

In the SPEELS experiment, a spin-polarized electron with a well-defined kinetic energy is shot onto the sample and scattered from the remanently magnetized surface. First, the primary electron enters the solid and occupies an electronic state in the empty part of the band structure above the vacuum level (see Fig. 2.7 (d)). Since the sample is ferromagnetic, both the occupied and unoccupied bands are spin-split due to the exchange interaction. The electron then thermalizes down to the Fermi energy via elementary excitations. In the vicinity of the Fermi level, the spin-splitting is important and leads to different densities of states for the majority and minority electrons. As a feature of a ferromagnet, the empty minority density of states is always higher than the majority one. Then, with a certain probability, the energy is transferred to an electron in an occupied spin state. This electron is then lifted above the vacuum level. It leaves the crystal with a kinetic energy $\mathrm{E_i}$- ε towards the detector. After the scattering process the electronic system of the solid is left with an electron above and a hole below the Fermi level (see the red solid circle and blue open circle in Fig. 2.7). The energy loss corresponds to the creation energy of the electron-hole pair. It should be noted that the spin-flip between the spins of incident and scattered electrons occurs due to an exchange of the incident electron with one of the sample electrons instead of a real spin reversal [7, 75]. The interaction is of a pure Coulomb nature. The process occurs within a few attoseconds and without any energy dissipation.

In the experiment, a channeltron was used to measure the intensity of electrons scattered from the sample under a particular angle and with a certain energy transfer. For the inelastic scattering, electrons lose or gain energy by creating or annihilating excitations at the surface. Assuming that an electron only experiences one scattering at the surface, the energy ε of the excitations is given by $\varepsilon = E_i - E_f$, where E_i and E_f denote the energy of the incident and scattered electrons, respectively. Since the in-plane momentum of the electrons is conserved during the scattering, the in-plane wave-vector of the excitation is given by:

$$\mathrm{q} = -\Delta \mathrm{K}_{||} = \mathrm{K}^{\mathrm{i}}_{||} - \mathrm{K}^{\mathrm{f}}_{||} = \mathrm{K}^{\mathrm{i}} \sin\theta - \mathrm{K}^{\mathrm{f}} \sin(\theta_0 - \theta), \tag{2.18}$$

which is illustrated in Fig. 2.8. $\vec{\mathrm{q}}$ is the wave-vector of the excitation. $\Delta\mathrm{K}_{||}$ is defined as the change of the wave-vector parallel to the surface. The wave vectors of incident and outgoing electrons are represented by $\vec{\mathrm{K}}^{\mathrm{i}}$ and $\vec{\mathrm{K}}^{\mathrm{f}}$. Their in-plane components are $\vec{\mathrm{K}}^{\mathrm{i}}_{||}$ and $\vec{\mathrm{K}}^{\mathrm{f}}_{||}$, respectively. θ and θ_0 are the incident angle and the angle between the two beams. Here we confine our discussion in the first Brillouin zone, so the reciprocal lattice vector $\vec{\mathrm{G}}_{||}$ does not appear in Eq. 2.18. As a result, by altering θ and keeping θ_0 as a constant, the magnons with various wave-vector transfers can be excited.

In addition, in the case of the creation of a magnon, the angular momentum of a ferromagnetic system is reduced by $1\hbar$. Due to the conservation of the angular momentum in the scattering process, the spin momentum of the scattered electron must be increased by $1\hbar$ compared to the incident electron. This condition can be only fulfilled by the case that the incident electron with minority character and the scattered electron with majority character. Since the majority electrons cannot increase their spin momentum anymore, only the minority electron is allowed to create magnons in ferromagnetic system. Vice versa, the annihilation of a magnon is only possible in the

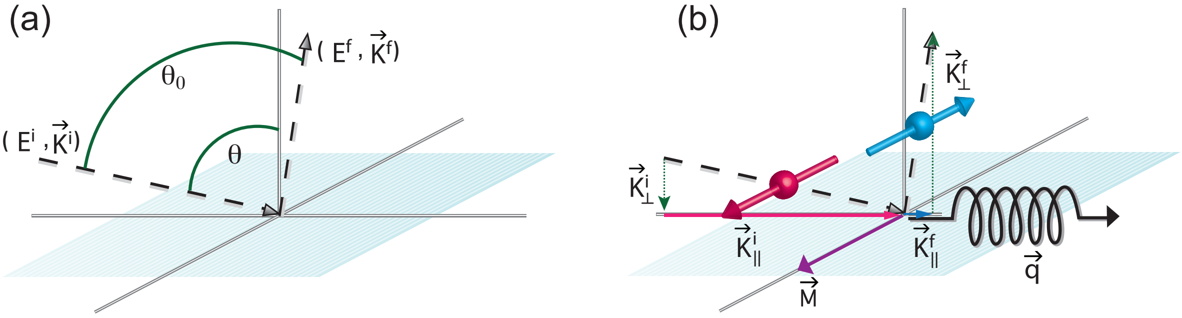

Figure 2.8: (a) The scattering geometry of the SPEELS experiment for the positive in-plane wave-vector transfer. θ_0 is the angle between the incident and outgoing direction, and θ is the angle of the incidence to the surface normal. (b) $\vec{\mathrm{K}}^{\mathrm{i}}$ and $\vec{\mathrm{K}}^{\mathrm{f}}$ denote the wave-vectors of the incident and outgoing electrons, whose in-plane components are $\vec{\mathrm{K}}^{\mathrm{i}}_{||}$ and $\vec{\mathrm{K}}^{\mathrm{f}}_{||}$. The magnetization direction, $\vec{\mathrm{M}}$, is perpendicular to the scattering plane and parallel (antiparallel) to the spin directions.

case that the incoming electron is of majority character and the outgoing electron is of minority character. By this selection rule, magnons are the only excitations in electron scattering that gives a 100% spin-polarized loss peak and more importantly the sign of the spin asymmetry of the excitation peak in the loss and gain region has to be opposite.

For a thin film composed of n layers, the Heisenberg model predicts n modes. However, it will be shown in this work that only one mode (acoustic surface mode) is observed in the SPEELS measurement. The first reason may be due to the fact that for the acoustic mode the moments precess in phase. The transverse components of spins are added to each other. In contrary, for the optical modes the moments precess out-of-phase. Thus, the transverse components of the spins are cancelled out [76]. The second reason is that the small cross-section of the excitations and the strong damping effect on the high energy modes. The third possible reason is that the acoustic surface mode has the largest amplitude at the surface. Since SPEELS is strongly surface sensitive, only the acoustic surface mode can be observed. However, recent experiments performed by Schneider *et al.* [77] show a signature of two bands on 8 ML Co/Cu(001) using a newly-developed high resolution spectrometer.

Chapter 3

Experimental Techniques

The control of the surface properties of the sample and its cleanliness is a necessity for surface sensitive experiments. To meet these requirements, the experiments were performed in ultra high vacuum (UHV) chambers specially designed for this purpose. In the first part of this chapter, the UHV system used for this study is illustrated. The structural, chemical, and magnetic properties are measured in-situ in the chamber by low energy electron diffraction (LEED), Auger electron spectroscopy (AES), and magneto-optic Kerr effect (MOKE). The spin-polarized electron energy loss spectroscopy set-up is described in section 3.2. Details concerning preparation and characterization of the samples are discussed in section 3.3.

3.1 The ultra high vacuum system

The experiments are performed in an UHV system. In Fig. 3.1, a sketch of the UHV system in top view is shown. The set-up is mainly composed of three chambers and a manipulator. The cathode chamber is used to prepare the GaAs-photocathodes. The analysis chamber is used to prepare the samples by the molecular beam epitaxy (MBE) and to characterize their chemical, structural, and magnetic properties by AES, medium energy electron diffraction (MEED), LEED, and MOKE. The latter two characterization techniques will be discussed in the following. The SPEEL-spectrometer is integrated in the SPEELS chamber. Samples are prepared in the analysis chamber, and they can be transferred between the analysis chamber and the SPEELS chamber by the manipulator. The transfer of the sample is always along the main axis of the system, which is the central axis of the SPEELS and the analysis chamber.

In a typical SPEELS measurement, the film is prepared and magnetized in the analysis chamber. At the same time, a GaAs photocathode is prepared by the deposition of Cs in an oxygen atmosphere (10^{-8} mbar) and then transferred to the SPEELS chamber as the source of the spin-polarized electrons. After the sample is transferred from analysis chamber to the SPEELS chamber and placed at the scattering position, the SPEELS measurements are then started. The base pressure is in the low 10^{-11} mbar range in the SPEELS chamber during the measurement and in the medium 10^{-11} mbar range in the analysis and cathode preparation chamber.

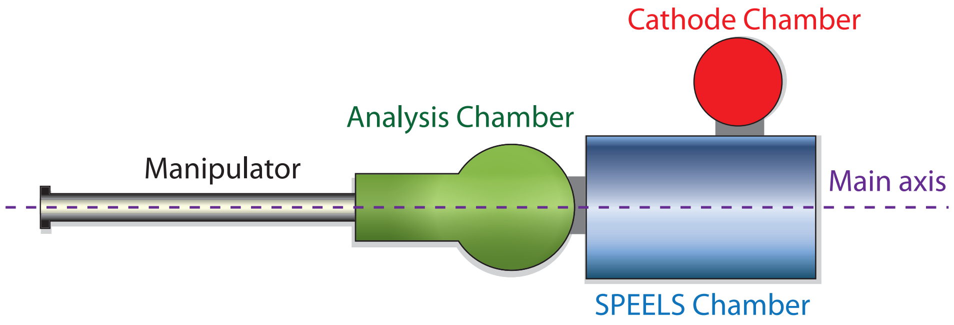

Figure 3.1: The top view of our UHV system. Different colors represent different parts of the UHV system. It is mainly composed of one manipulator and three chambers, which are the analysis chamber (green), the SPEELS chamber (gray), and the cathode chamber (red). Samples can be transferred between the analysis chamber and the SPEELS chamber by the manipulator. The GaAs-photocathode is transferred between the cathode chamber and SPEELS chamber by an UHV wobble stick.

3.1.1 Low Energy Electron Diffraction

LEED is a technique for the determination of the surface structure of crystalline materials by bombardment with a collimated beam of low energy electrons (10-400 eV) and observation of diffracted electrons as spots on a fluorescent screen. A sketch of the LEED experimental set-up is shown in Fig. 3.2 (a). Qualitatively, analysis of the position of the pattern gives information on the symmetry of the surface structure. The wavelengths of the electrons with an energy between 10 eV and 400 eV is comparable to the lattice constants of crystals. The penetration depth is about 5-10 Å, which results in a high surface sensitivity. In the presence of an adsorbate on the substrate the qualitative analysis may reveal the information about the size and rotational alignment of the adsorbate unit cell with respect to the substrate unit cell. Quantitatively, the intensities of diffracted beams are recorded as a function of incident electron beam energy to generate the so-called IV-LEED spectra. In principle, by comparing to the theoretical curves, these may provide accurate information on atomic positions on the surface.

Because of the nature of the low energy electrons, surface crystallography using LEED requires complicated theoretical descriptions considering the strong electron-ion-core scattering and the multi-scattering procedure. However, the *average* vertical lattice spacing of the surface layers can be extracted from a quantitative analysis of IV-LEED spectra of the (00) spot. The sample is rotated to deviate from normal to the incident electron beam by a small angle θ as seen in Fig. 3.2 (b). By tuning the incident electron energy to fulfill the Bragg condition (see Fig. 3.2 (c)), the intensity of the specular beam will reach a maximum for:

$$2d\cos\theta = n\lambda (n = 1, 2, 3, ...), \tag{3.1}$$

where d is the interlayer spacing, λ is the wavelength of the electron, and n is the interference mode. Since the angle θ is small, $\cos\theta \approx 1$. Therefore,

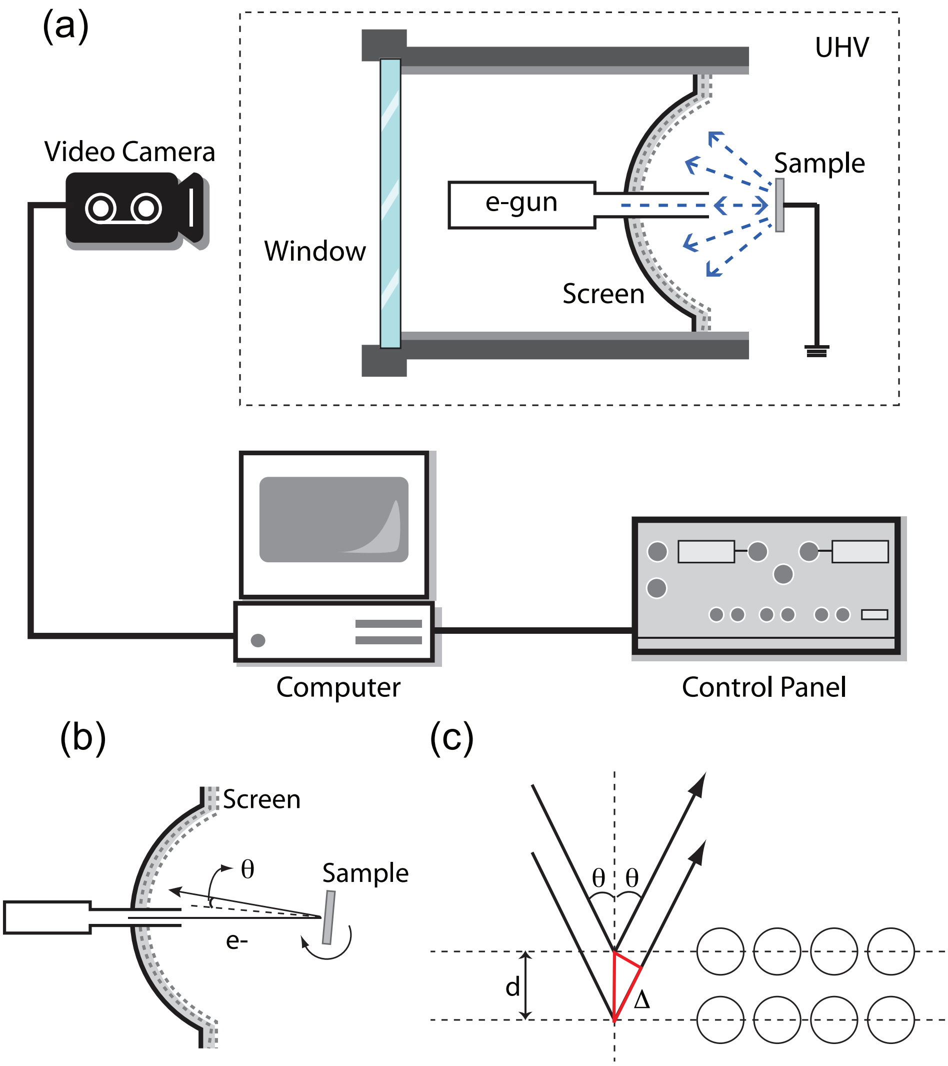

Figure 3.2: (a) A sketch of IV-LEED measurement. The electron energy is controlled by a program via the control panel. The images of the diffraction patterns on a fluorescent screen are captured by a video camera and transferred to a computer. (b) The sample is rotated by a small angle θ from normal configuration for extracting the intensity of the (00) spot. (c) The intensity maxima of (00) beam fulfills Bragg diffraction condition, where d is the interlayer spacing and Δ is the optical path difference.

$$\lambda \approx \frac{2d}{n}. \tag{3.2}$$

The electron kinetic energy is modified by the internal potential of the material V_0 when the electrons penetrate into the surface layers. Therefore, the electron energy E could be expressed as :

$$E = \frac{h^2}{2m\lambda^2} + V_0, \tag{3.3}$$

where h is the Planck constant and m is the electron mass. By substituting Eq. 3.2 into Eq. 3.3,

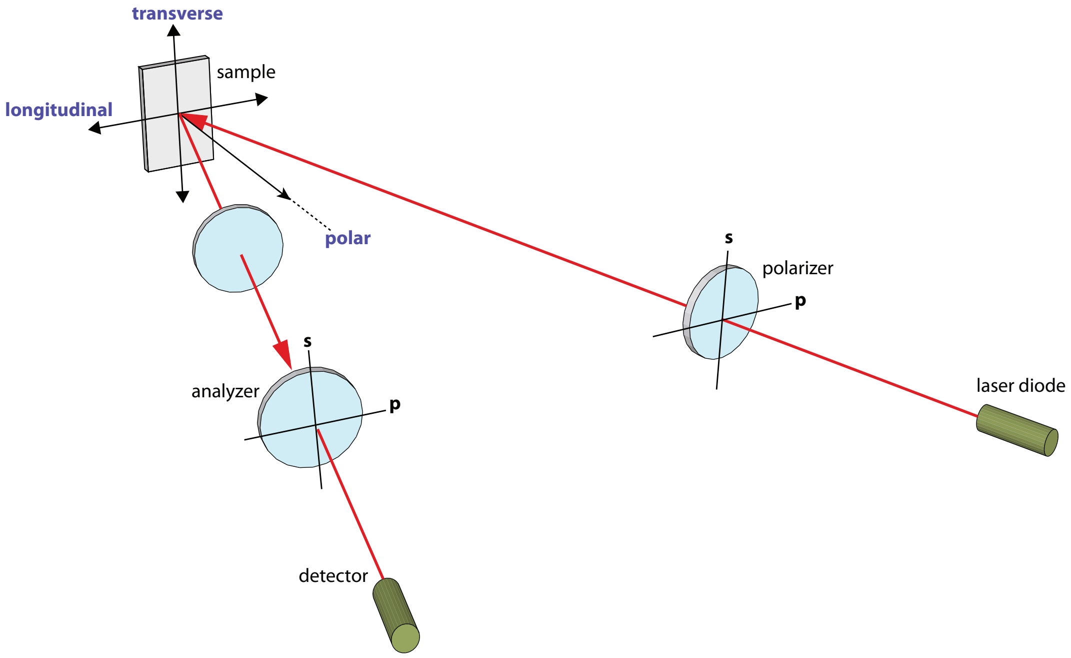

Figure 3.3: A sketch of the MOKE measurement with longitudinal, transverse, and polar geometry.

$$E = \frac{h^2}{8md^2}n^2 + V_0. \tag{3.4}$$

Thus, the interlayer lattice spacing d can be obtained from the slope by fitting the linear relation between the electron energy E and the square of the interference order, n^2. The IV-LEED analysis of the Fe films grown on 2 ML Au/W(110) will be illustrated in section 3.3.

3.1.2 Magneto-Optic Kerr Effect

It has been found that the polarization state of the light is changed when reflected from a surface of magnetic material. When linearly polarized light reflects from a magnetic film, its polarization becomes elliptic (Kerr ellipticity) and the principal axis is rotated (Kerr rotation). The amount of rotation and ellipticity is proportional to a component of the magnetization of the film. The origin of the magneto-optic effect is attributed to the antisymmetry parts of the dielectric tensor of a medium in a macroscopic picture based on dielectric theory. Microscopically, the electric field of the propagating light couples with the electron spin in the medium through spin-orbit interaction. Visible light only penetrates some 20 nanometer in typical metals. Therefore, with MOKE only the magnetization near the surface is probed. Since we are generally studying ultrathin films (typically tens of angstrom), this is not a real limitation.

The diagram of a MOKE measurement is schematically shown in Fig. 3.3. Three conventional magneto-optic configurations (longitudinal, transverse, and polar MOKE) are defined according to the respective direction of the magnetization to the scattering plane. When the magnetization direction is perpendicular to the reflection surface and parallel to the scattering plane, the effect is called the polar Kerr effect. In the longitudinal effect, the magnetization direction is parallel to both the reflection surface and the scattering plane. When the magnetization is perpendicular to the plane of incidence and parallel to the surface it is said to be in the transverse configuration. The magnetization direction and the magnetic anisotropy of the magnetic films can be studied along three axes by analyzing the hysteresis loops obtained from the measurements with three MOKE geometries.

In this work, only the longitudinal MOKE is measured. For the longitudinal MOKE measurements, the incident laser beam is s-polarized by a linear polarizer. We first adjust the directions of two analyzers to be mutually perpendicular by finding the minimum reflected laser intensity. Then, the background intensity can also be recorded. Afterwards, one of the analyzers is rotated by 1.43° (0.025 rad) away from the original direction. Then, by recording the reflected laser intensity as a function of the magnetic field applied on the sample along two opposite directions, the Kerr ellipticity can be obtained. The results of the MOKE measurements will be presented in section 4.1 and 4.3.

3.2 Spin-Polarized Electron Energy Loss Spectroscopy

In the SPEELS experiments, spin-polarized electrons are scattered from a sample. The energy and momentum transfer of the scattered electrons are analyzed for the two possible spin directions of the incident electrons. The intensity of the scattered electrons are recorded as a function of their energies. In the following subsection, the construction of the SPEELS set-up and the operation of the experiments are described. The principle and the preparation of the GaAs photocathodes are illustrated subsequently.

3.2.1 SPEEL-spectrometer

The SPEEL-spectrometer is composed of two main parts, the electron energy monochromator and the energy analyzer as shown in Fig. 3.4. The monochromator consists of a pre-monochromator and a main monochromator with deflection angle of 90° and 180°, respectively. The energy analyzer is a standard EELS-monochromator with a deflection angle of 146° [78, 79].

The GaAs photocathode is located in front of the 90°-monochromator. A circularly polarized laser beam (red solid line in Fig. 3.4) with the wavelength of 830 nm is applied to the creation of the spin-polarized electrons. The electron beam which leaves the GaAs-photocathode is longitudinal spin-polarized according to the selection rules [70]. Therefore, the emitted electrons have their spins parallel or antiparallel to the direction of the incident laser beam depending on the polarization of the light. The electrostatic potentials do not affect the spin direction. Thus, the total deflection angle of the monochromator should be an odd multiple of 90° in order to have a transverse spin-polarized electron beam with the spin direction perpendicular to the scattering plane. Only the electrons with proper energy can pass through the pre- and main monochromator and then be focused on the sample surface. The magnetization direction is parallel to the main axis as shown as the dashed line in Fig. 3.4. Hence,

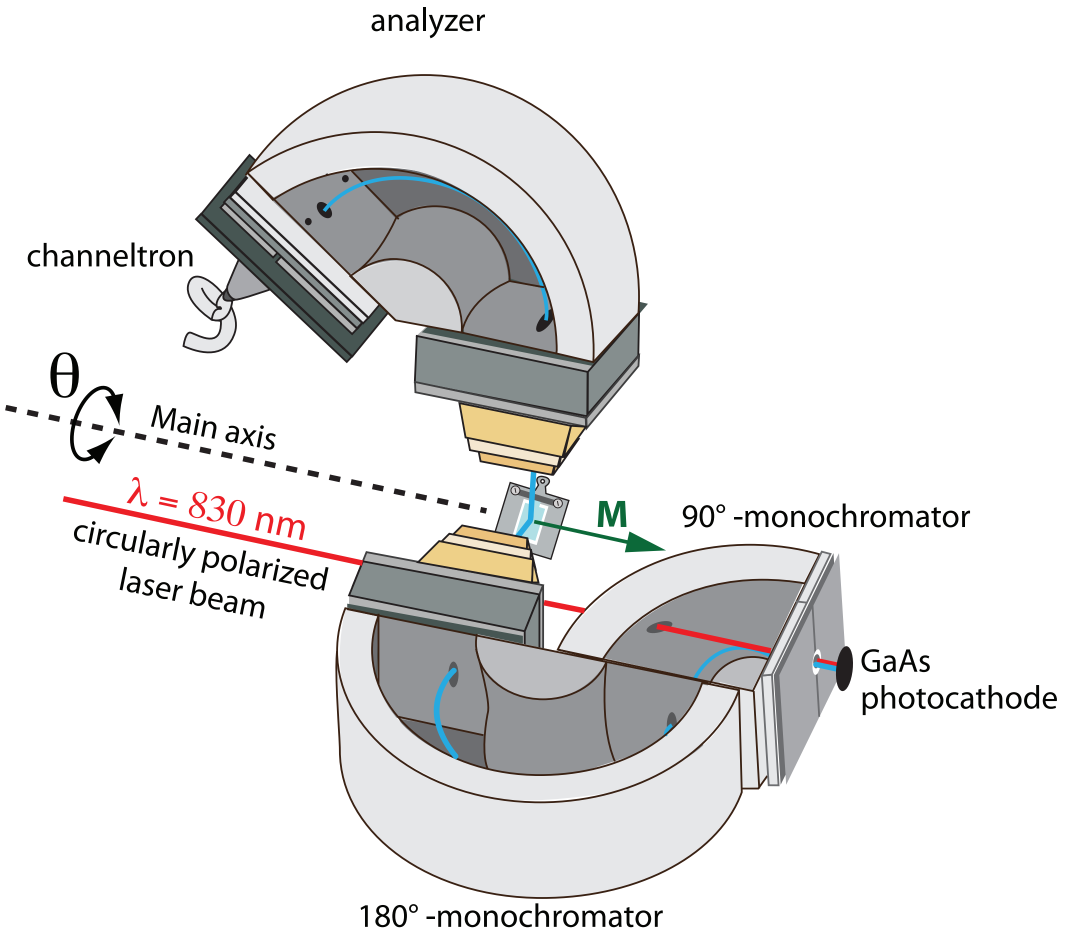

Figure 3.4: An illustration of the spectrometer under operation with a GaAs-photocathode. The circularly polarized light excites a longitudinal spin-polarized electron beam from the cathode. After the electrons traveled through the electrostatic monochromators, the electron beam is transversely polarized, which is parallel to the magnetization (M) direction. Electrons having the proper energy travel through the analyzer into the detector. The electron path is shown as the blue line.

by changing the polarization of the laser beam, the spin direction of electrons can be controlled to be parallel or antiparallel to the magnetization.

The analyzer and the detector are mounted on an arm so that they can be rotated around the main axis in the scattering plane. The accessible range of the angle between the monochromator and the analyzer (θ_0) is from 80° and 280°. We keep θ_0 at 80° in this work. A channeltron is next to the exit slit of the analyzer. The transmitted electrons were counted with the channeltron working in the single electron counting mode. The SPEEL-spectra shown in the following were recorded by setting a loss energy and then counting the number of electrons scattered under this loss for both possible directions of the incident electron spin. The number of electrons was counted for one second for both of the incoming spin directions. Then, the analyzer was set to the next loss energy and so on. Once the full spectra was recorded, the measurement was repeated several times to have better statistics. There is no spin detector connected to the analyzer.

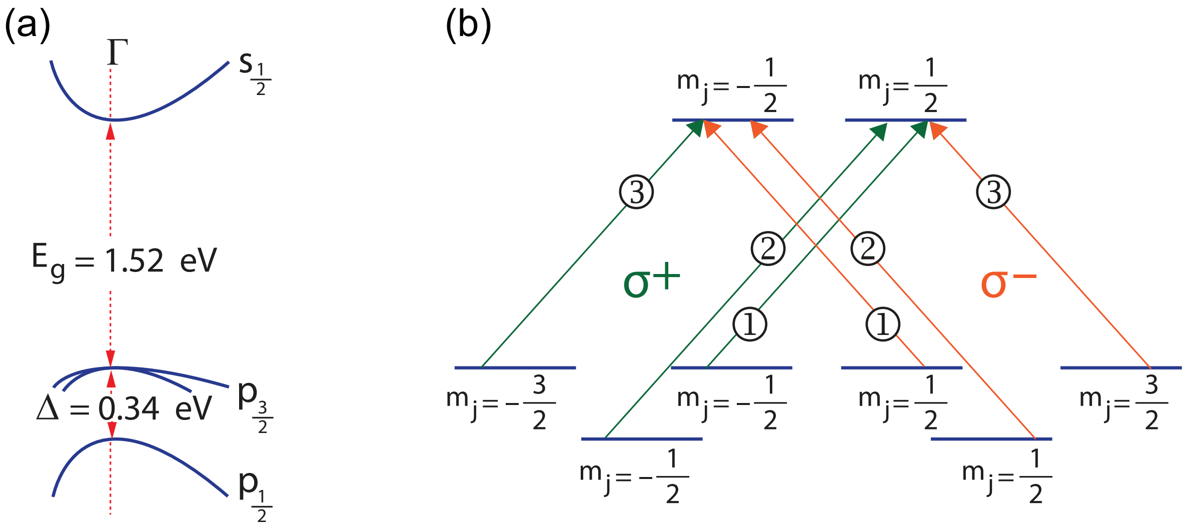

Figure 3.5: (a) Schematic diagram of the energy position of the conduction band and the spin-orbit split valence bands for wave-vectors close to the origin in GaAs. (b) An illustration of the energy states for different quantum numbers m_j and the possible transitions for σ^+ (σ^-)-circular polarized light, shown as green (red) arrows. The numbers on the arrows are the relative transition probabilities.

In the SPEELS measurement, the energy distribution of the scattered electrons are scanned by the analyzer. The energy resolution for a given design of a dispersive element is determined by the kinetic energy of the electrons that are transmitted, which is called pass energy. Therefore, the energy resolution can be changed by applying different potentials to the dispersive elements. A detailed description of the design of this SPEEL-spectrometer is given in Ref. [80].

3.2.2 The GaAs-photocathode

It has been shown almost 40 years ago that GaAs can be used to create spin-polarized photoelectrons [81]. The underlying physical reason is illustrated in Fig. 3.5. The GaAs $p_{\frac{1}{2}}$ and $p_{\frac{3}{2}}$-valence bands lie at different energy level due to the spin-orbit interaction. When a circularly polarized light with proper wavelength is illuminated, transitions from these valence bands into the conduction $s_{\frac{1}{2}}$-band are possible. The relative excitation probabilities from different bands depend on the helicity of the incoming light as shown in Fig. 3.5. Since the $p_{\frac{1}{2}}$ and $p_{\frac{3}{2}}$-bands are split, when the energy of the light is exactly 1.52 eV, the transition from $p_{\frac{1}{2}}$-band are not possible. The conduction band will be populated with more electrons with specific spin direction than the other. The polarization can be defined as $P = \frac{N_\uparrow - N_\downarrow}{N_\uparrow + N_\downarrow}$, where $N_\uparrow$ ($N_\downarrow$) is the number of electrons with spin up (spin-down) character. The transition probability shown in Fig. 3.5 (b) is 50% if illuminating the light with the energy of 1.52 eV. One way to increase the spin polarization is to remove the degeneracy of the two upper valence bands. This can be achieved by adding strain to the GaAs lattice at the surface by growing it epitaxially on the proper substrate [82]. For these strained GaAs photocathodes, the optimum wavelength of the incident light is about 830 nm (∼1.49 eV).

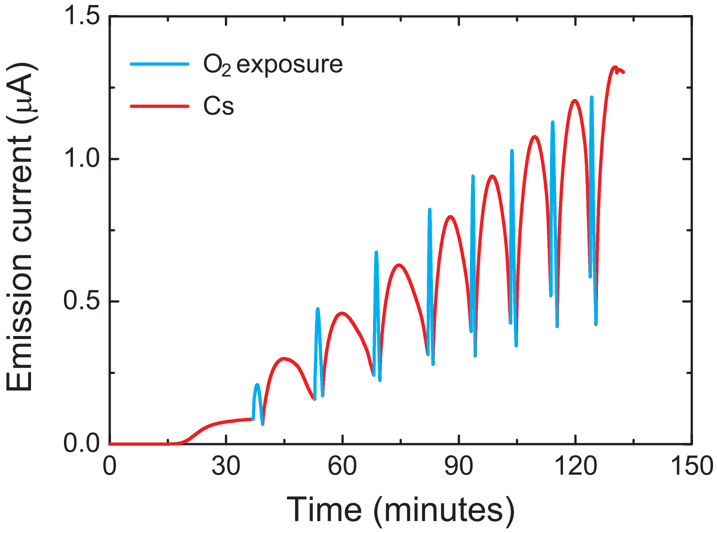

Figure 3.6: Measurement of the photocurrent of a GaAs-photocathode during the preparation. Cs is kept evaporating during the whole preparation. Blue peaks indicate the O_2-exposures with the pressure of about 10^{-8} mbar.

However, for a clean GaAs surface, the work function is too high to allow the electrons to escape. To extract these photoelectrons into vacuum, it is necessary to lower down the work function on the surface. It is reported that by the adsorption of Cs and O on the surface the work function is drastically reduced [81]. The recipe to prepare the GaAs surface is described in the following.

First, the photocathode is heated to about 620 K for 1 hour and then the heating power is increased to about 25 W for 5 minutes. The temperature is increased to about 850 K. After the surface cleaning procedure, the sample is cooled down to about 370 K. Then, the cathode is exposed to Cs and O_2 sequentially. During these sequences, the photocurrent is measured. An example of the measured photocurrent during the preparation is shown in Fig. 3.6. First, Cs is evaporated and then the photocurrent is gradually increased until saturated. Then, the surface is exposed to an O_2 atmosphere of about 10^{-8} mbar. This leads to a strong increase of the photocurrent. The O_2 exposure is stopped when the current dropped to $\frac{1}{3}$ of the maximum value (see the blue peaks). An additional amount of Cs was added until the current dropped to half of its maximum value (see the red peaks).

This procedure is repeated until the maximum value of the photocurrent is saturated. Usually, it takes 5 to 8 cycles. The maximum photocurrent is typically around 1 to 10 μA when illuminating the GaAs with a wavelength of 830 nm laser beam. Typically, we keep the photocurrent as 1 μA during the SPEELS measurement. The reduction of the photocurrent is achieved by reducing the incident laser power. Due to the contaminations on the surface of the cathode, the photocurrent decreases by time. In order to compensate the decay of the current by time and to achieve a stable emission, the laser power is increased by time. When the current is dropped to the value lower than 0.5 μA with maximum laser power, the cathode has to be prepared again.

In order to estimate the polarization of the electrons emitted from the photocathode,

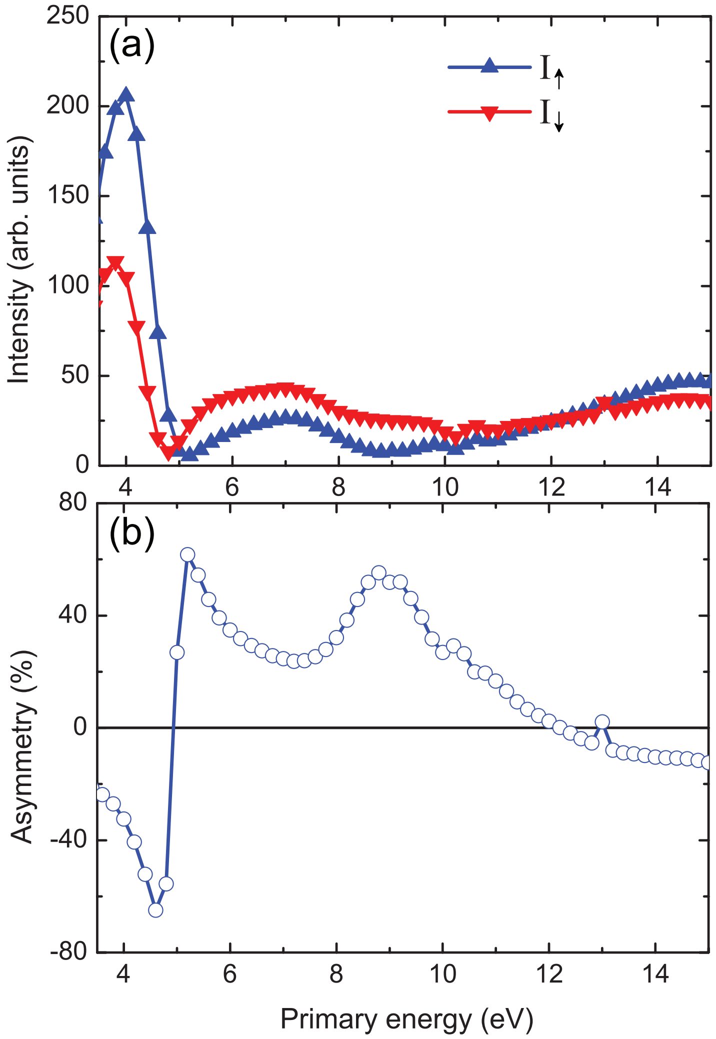

Figure 3.7: (a) Measurement of the elastically scattered electron intensity of the two different spin directions of the incident electrons as a function of the incident electron energy. The beam is scattered from a W(110) crystal. The scattering plane is parallel to the [001]-direction. Because of the high intensity of the elastically reflected electron beam, the channeltron is operated in a continuous current mode. Thus, the intensities are shown in arbitrary units. (b) The asymmetry of the two intensity curves, $A=(I_\downarrow-I_\uparrow)/(I_\downarrow+I_\uparrow)$. The highest asymmetry of 62% is at the incident electron energy of 5.2 eV.

the intensity of the specular beam reflected from a clean W(110) surface is measured as a function of the incident energy. The results are shown in Fig. 3.7. Due to the strong spin-orbit interaction in W(110), the intensity spectra obtained from the incident spin parallel ($I_\uparrow$) and antiparallel ($I_\downarrow$) to the spin of the majority electrons have a large difference depending on the incident energy. The asymmetry is defined as $A = \frac{I_\downarrow - I_\uparrow}{I_\downarrow + I_\uparrow}$. The largest asymmetry is about 62% at 5.2 eV as shown in Fig. 3.7 (b). The measured asymmetry is the product of the beam polarization P and the factor S, where S gives the ideal asymmetry in the case of a totally spin-polarized electron is applied. The maximum value of S is 1. Thus, this sets the lower limit of the spin polarization, which is P=A/S=62%/1 = 62%. On the other hand, the largest value of S for the W surface is never larger than 80% in previous studies [83, 84, 85]. Therefore, the upper limit of the spin polarization is P=A/S=62%/0.8 = 78%. As a result, taking the average of these two values, the spin polarization of the incident electrons in this work is 70±8%.

3.3 Sample preparation and characterization

In this work, the word monolayer (ML) is defined as the unit of the film thickness. It defines an atomic density the same as that of the substrate surface. In the case of W(110), 1 ML=1.41×10^{15} atoms per cm^2. In the case of Ir(001), 1 ML=1.35×10^{15} atoms per cm^2.

Two different surface structures of Fe thin films are investigated in this work. One is 2 ML Fe(111) grown on 2 ML Au(111) on W(110), and the other one is Fe(001) grown on Ir(001). In the first subsection, a special cleaning procedure of W(110) substrate is shown. The Au and Fe films are prepared by molecular beam epitaxy (MBE). In addition, the IV-LEED investigation on a series of Fe films with different thicknesses grown on 2 ML Au/W(110) is performed to probe the interlayer distances of Fe atoms within the films. In section 3.3.2, the characterization of Fe films grown on Ir(001) substrate is presented, including a series of LEED patterns recorded on different thicknesses of Fe films.

3.3.1 Fe/Au/W(110)

The first important step to have epitaxial growth is to prepare a clean substrate. In our cleaning procedure, we use electron bombardment to heat the substrate. A constant high voltage is applied to the sample. A dc current flowing through the filament causes an emission current flowing from the filament to the sample. In order to avoid the heat dissipation into the UHV system, a short time heating (flashing) is applied.

In this work, a single W(110) crystal with the dimension of 8 mm×5 mm×0.3 mm is used. Tungsten is a substrate with high melting point and absence of intermixing with the overlayer. Carbon and oxygen are the most familiar contamination on the tungsten surface. In our lab, a highly efficient cleaning procedure is developed to remove the contaminants [86]. The cleaning procedure consists of two steps.

First, few cycles of low power flash are applied in oxygen atmosphere (6×10^{-8} mbar). The heating power is switched on for 15 seconds and off for 60 seconds. An emission current of about 40 mA and a voltage of V=1.1 kV (Power: P=44 watts) leads to a sample temperature of about 1200 K measured by a pyrometer. This step is used to remove the carbon from the substrate surface by the reaction of the oxygen adsorbed on the surface. The number of cycles depends on the amount of the contaminants on the surface. This can be determined by monitoring the partial pressure of CO inside the chamber, measured by a quadrupole mass spectrometer. Detailed analysis can be found elsewhere [86]. The second step is to apply a single high power flash at vacuum to reach the temperature of 2200 K. This is used to remove the oxygen layer from the surface of the substrate. The emission current is 140 mA with a voltage of V=1.1 kV (Power: P=154 watts). After these two steps, a clean W substrate is prepared. The

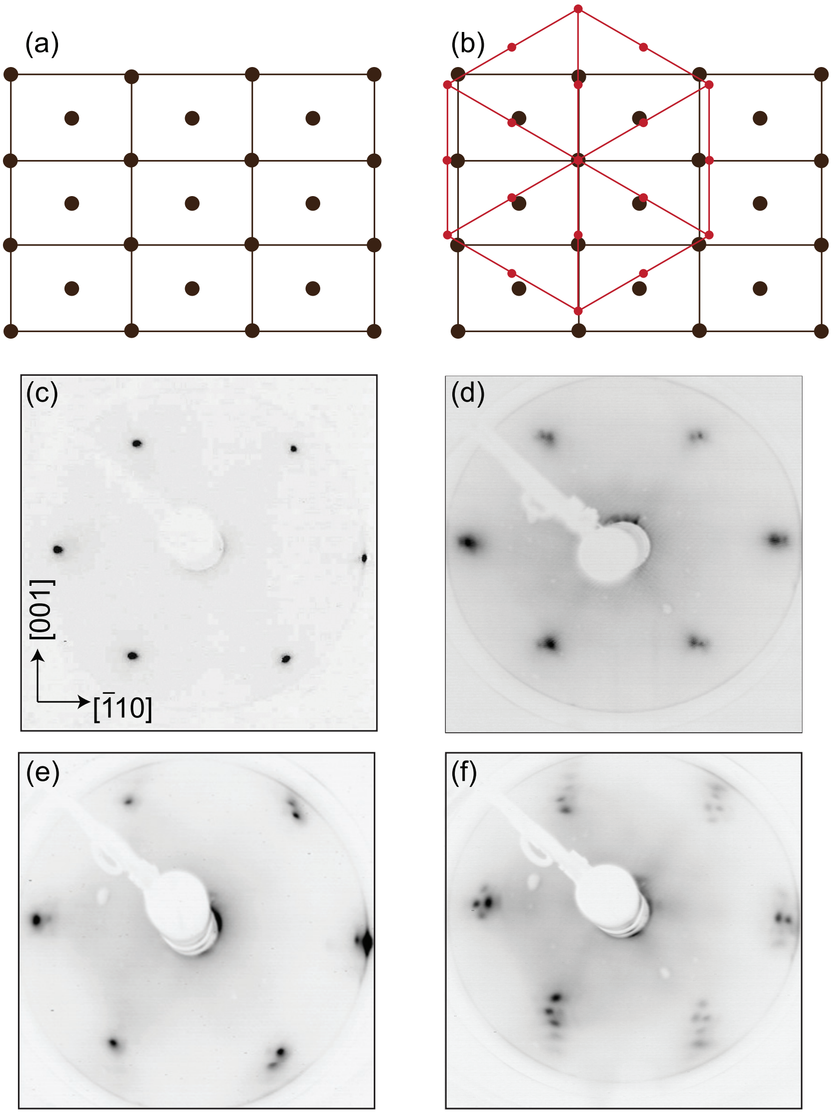

Figure 3.8: A real space representation of (a) W(110) surface and (b) Au(111) surface structure (red hexagonal) on W(110). The LEED images of (c) W(110) and (d) 1 ML, (e) 2 ML, and (f) 3 ML Au grown on W(110). The images are taken at a primary electron energy of 62 eV.

chemical properties of the surface is checked by the Auger electron spectroscopy. The LEED pattern taken from a clean W(110) substrate with a primary electron energy of 62 eV is shown in Fig. 3.8(c).

It is known that an Fe film is pseudomorphically grown on W(110) substrate and form Fe(110) surface up to 2 ML [19]. In order to change the surface structure of Fe, one may choose a substrate with (111) surface orientation. It has been investigated by scanning tunneling microscopy (STM) and LEED experiments that an Fe film is grown pseudomorphically on Au(111) surface at the initial stage of growth [87, 88, 89, 90]. However, it has also been presented that a clean Au(111) crystal has reconstruction on the surface, known as herringbone reconstruction. The surface morphology of the ultrathin Fe overlayer is strongly influenced by the reconstruction. Moreover, the mag-

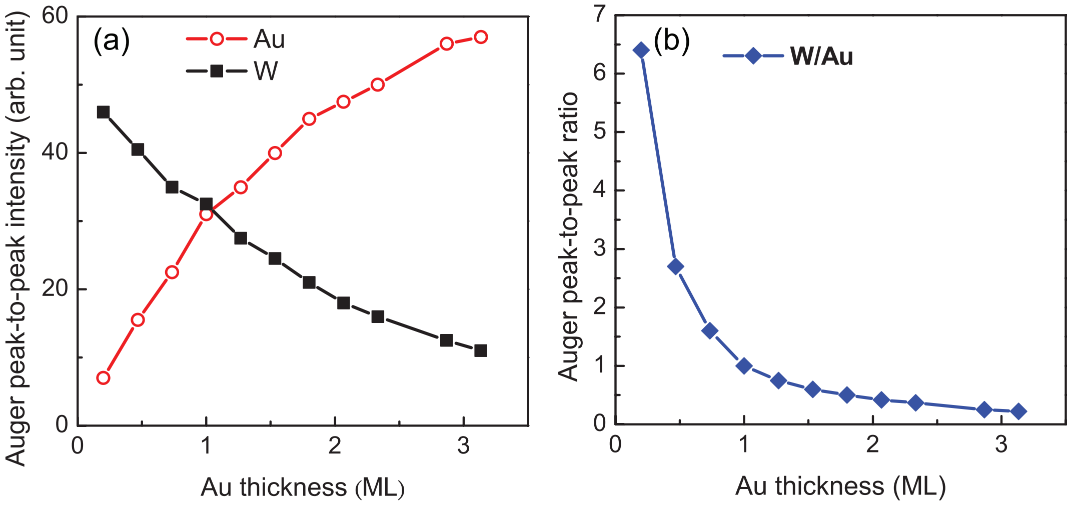

Figure 3.9: (a) The W (black) and Au (red) Auger peak to peak intensity and (b) their ratio (blue) as a function of Au thickness grown on W(110).

netic easy axis of an Fe film grown on Au(111) crystal has been reported to be in the out-of-plane direction at the initial stage of growth, where Fe is grown as fcc-like structure [90, 91, 92]. In our present SPEELS set-up, we only have the sensitivity in the in-plane magnetization direction. Therefore, due to a better surface quality and having the in-plane magnetic easy axis, we choose the method of inserting an ultrathin buffer layer with (111)-surface orientation to change the Fe surface structure.

Tungsten has a body-centered cubic (bcc) structure and bcc(110) surface is composed of rectangular unit cells as shown in Fig. 3.8(a). The LEED image of a clean W(110) substrate is shown in Fig. 3.8(c) with a primary electron energy of 62 eV. The gold crystal has a face-centered cubic (fcc) structure and the most similar surface to W(110) is the Au(111) surface. In our experiment, the Au and Fe films are prepared by MBE at 500 K and 300 K, respectively, with the base pressure better than 8×10^{-11} mbar. The Au film does not grow pseudomorphically on W(110) and forms its own Au(111) surface as verified by our LEED patterns taken from 1 ML, 2 ML, and 3 ML Au grown on W(110) (see Fig. 3.8(d)-(f)). The splitting of spots is not obvious in the case of only 1 ML Au grown on W(110) showing that the Au atoms are still effected by the W substrate and grown as a similar surface structure as W(110). The splitting becomes more pronounced when the thickness of the Au layer is above 2 ML, which is an indicatiion that the Au film is relaxed to its own structure. The additional spots in Fig. 3.8(f) for 3 ML Au on W(110) are produced by the double scattering between the Au layers and W substrate. A similar observation is also reported by Bauer *et al.* [93]. The characteristic change of the LEED pattern with the corresponding Au thicknesses is in agreement with the one reported in the Ref. [93]. One may argue that the splitting of LEED spots may originate from the island growth of the Au film on W substrate. We exclude this possibility by the Auger electron spectroscopy investigations.

In Fig. 3.9 (a), the Auger peak intensity of Au and W are shown as a function of the Au thickness. The Au signal increases as the thickness of Au layer increases, and the substrate signal decreases accordingly. It is noticed that three breaks on the red curve are observed due to the completion of each Au layer. Their peak to peak ratio

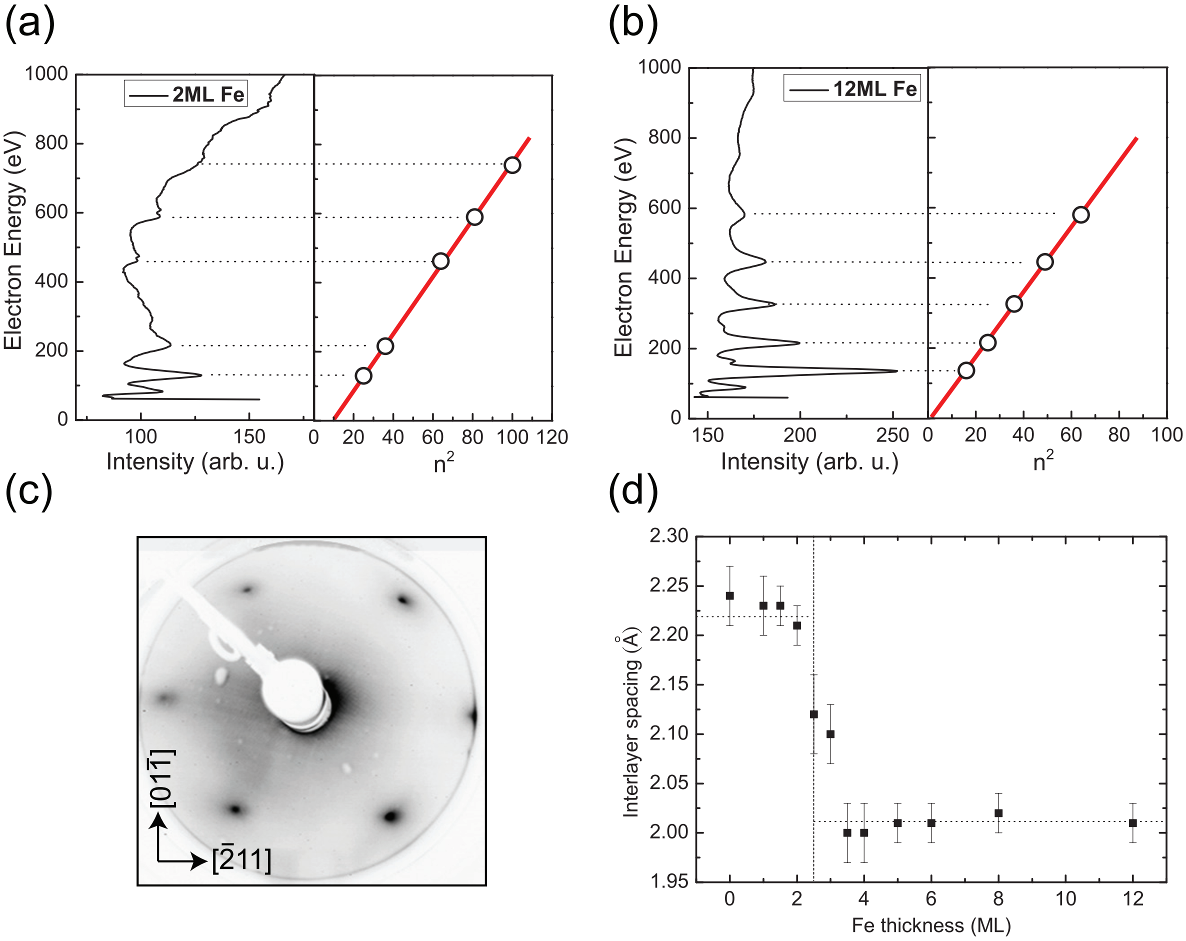

Figure 3.10: IV-LEED experiments on different thicknesses of Fe films grown on 2 ML Au/W(110). The intensity of (0,0) spot as a function of incident electron energy measured on (a) 2 ML Fe and (b) 12 ML Fe. The E-n^2 relations are fitted with a linear slope to extract the values of the interlayer spacings. (c) The LEED image taken from 2 ML Fe on 2 ML Au/W(110) of a primary electron energy of 65 eV. (d) Average interlayer spacings as a function of the Fe film thickness.

(see Fig. 3.9 (b)) approaches to zero when thickness of Au is thicker than 3 ML. This is an indication that Au film is most probably grown in a layer by layer mode. The possibility of the island growth can be excluded.

The magnetic properties of Fe films grown on Au layers with different thicknesses on W(110) have been studied by spin polarized low energy electron microscopy [94, 95]. It is shown that the Fe thickness for the onset of ferromagnetic order depends on the thickness of underlying Au film. The easy axis direction also depends on the Au thickness. It is parallel to the W[1$\bar{1}$0] direction at the onset of magnetization for one and two ML of Au. For the thicker films, the easy axis is parallel to the [001] direction. Since in the SPEELS measurement the scattering plane is also parallel to W[001] direction, a thicker Au film (> 2 ML) is not suitable for our experiments. Therefore, we choose the Au layer to be 2 ML. In this case, we will have an Fe layer with (111) surface orientation and an easy axis parallel to [1$\bar{1}$0].

In order to provide an insight into the structure of the Fe film on 2 ML Au/W(110), we performed IV-LEED experiments. The average interlayer distance for different Fe thicknesses is measured by monitoring the intensity of (0,0) spot as a function of the incident electron energy as shown in Fig. 3.10(a) and (b) for the Fe thickness of 2 ML and 12 ML, respectively. The LEED image taken from the 2 ML Fe grown on 2 ML Au on W(110) with a primary electron energy of 65 eV is also shown in Fig. 3.10(c). The (1×1) pattern is an indication of pseudomorphic growth of Fe films on Au(111) surface. However, it is noticed that the pattern is not perfectly hexagonal (111) pattern but a slightly distorted one. This may be due to the distortion of the 2 ML Au film grown on W(110). Similar observation has been reported by Bauer, *et al.* [93].

As discussed in sec. 3.1.1, after choosing the proper interference numbers for the corresponding intensity peaks and plotting the E-n^2 relation, we can obtain the interlayer spacings by fitting the relation as a linear function according to the Eq. 3.4. The interlayer spacing can be obtained from the slope of the linear fit. The obtained results of interlayer spacing are shown in Fig. 3.10(d). The interlayer spacing starts decreasing when the thickness is above 2 ML. At the thickness above 4 ML, the interlayer distance is relaxed to the value of the one in bcc Fe(110). Since our aim is to grow Fe in (111) orientation, we limit our SPEELS experiments to the investigation of 2 ML Fe/2 ML Au/W(110).

3.3.2 Fe/Ir(001)

To prepare a clean Ir substrate, a similar cleaning procedure as the one of W substrate is used. Since Ir substrate is not strongly reactive to oxygen, carbon is the main contaminant on the Ir surface. Few cycles of low power flash are applied in oxygen atmosphere (6×10^{-8} mbar). The heating power is switched on for 20 seconds and off for 60 seconds with an emission current of about 65 mA and a voltage of V=1.1 kV (Power: P=71.5 watts). Then, a single high power flash is applied with the emission current of 140 mA with a voltage of V=1.1 kV (Power: P=154 watts). By cycles of low power flash in the oxygen atmosphere and subsequent high power flash in the vacuum, carbon is removed from the surface.

In the following investigation, we will probe the magnon dispersion relation along the Fe[100]- and Fe[110]-direction. However, we do not have the access to azimuthally rotate the sample in the chamber. Therefore, we prepare two Ir(001) substrates with different cutting directions (see Fig. 3.11 (f)). Their LEED images are shown in Fig. 3.11(a) and (b). An Ir(001) surface usually has Ir(001)-(5×1) reconstruction. The reconstruction appears in two mutually orthogonal domains. One of the methods to get Ir(001)-(1×1) surface is using hydrogen adsorption. With hydrogen adsorption and subsequent annealing, the extra atoms in the surface layer can be lifted and form the metastable Ir(001)-(1×1) surface structure. The detailed recipe has been presented in Ref. [16, 96, 97]. However, since we are investigating a relatively thick film (> 4 ML), the substrate surface reconstruction is not important to our study. LEED patterns obtained from 6 ML Fe films grown on the reconstructed Ir(001) substrate are shown in Fig. 3.11(c) and (d). A sharp (1×1) pattern is observed indicating a good periodic surface structure.

Ir(001) is an interesting substrate to study Fe growth on a fcc(001) substrate. Its in-plane parameter ($a_{||}$=2.715 Å) is right in between the corresponding parameters for

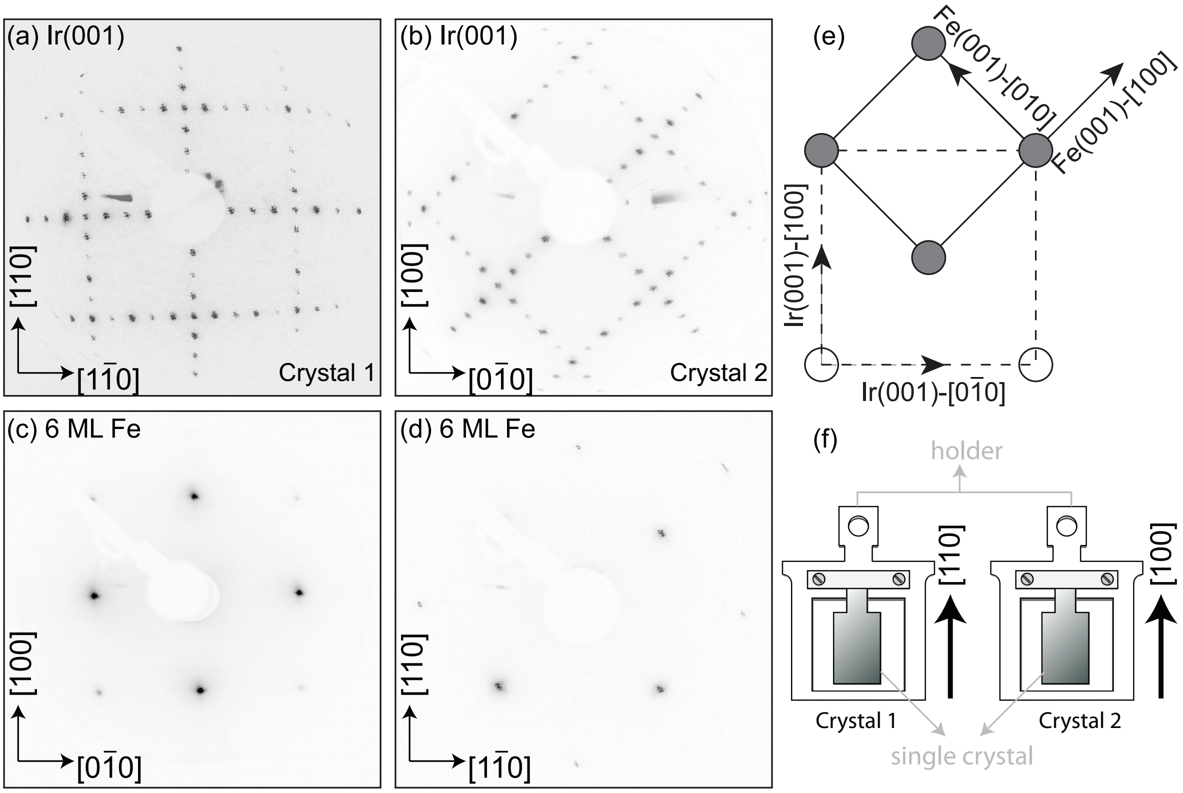

Figure 3.11: (a)-(b) LEED patterns of Ir(001) with (5×1+1×5) surface reconstruction. (c)-(d) LEED patterns of 6 ML Fe on Ir(001). All images are taken with a primary electron energy of 100 eV. Before recording the LEED patterns, Fe films are annealed at 900 K. The real space representation of the bcc-Fe(001) lattice on fcc-Ir(001) is illustrated in (e). (f) A sketch of the crystals and holders used in this work. Both crystals are with the same (001) surface but with different cutting directions.

bcc-Fe (2.866 Å) and fcc-Fe (2.527 Å) [98, 99]. It has been shown by Tian, *et al.* [16, 31, 32] that Fe grows pseudomorphically on Ir(001) as bct lattice structure for 2 ML to 10 ML. In Fig. 3.12, a series of LEED patterns of Fe films with various thicknesses grown on Ir(001) are shown. All films are annealed at 900 K to improve the surface quality. For the film thickness lower than 10 ML, the patterns are similar and the diffraction spots are clear and sharp. In agreement with the previous study, the Fe films are pseudomorphically grown up to around 10 ML. With increasing film thickness, extra satellite spots start to appear around the original spots. The satellite spots may originate from the extra periodic atom arrangement along the [100]-directions of Fe(001) surface (the [110]-directions of Ir(001)). It is also observed that the distance between each spot is slightly decreased comparing Fig. 3.12 (a) to (f). It indicates that the lattice parameter is longer when the film is relaxed, which is in agreement with the literature that the film is relaxed from pseudomorphically grown film ($a_{||}$=2.715 Å) to the bulk-like film ($a_{||}$=2.866 Å). The perpendicular lattice spacing of Fe layer on Ir(001) has been obtained by IV-LEED measurements [16, 31]. The magnetic properties of Fe/Ir(001) system are investigated by means of MOKE measurements. It will be presented and discussed in section 4.3.1.

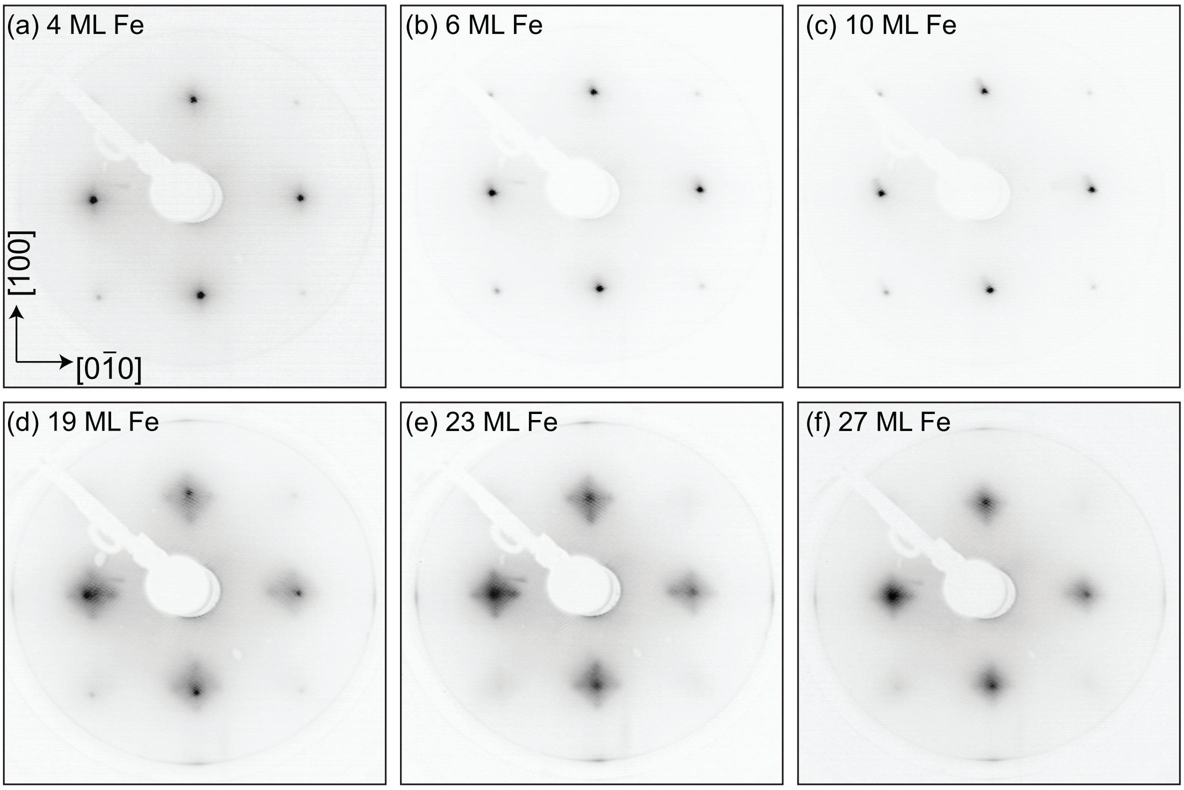
(a) 4 ML Fe
[100]
[0$\bar{1}$0]
(b) 6 ML Fe
(c) 10 ML Fe
(d) 19 ML Fe
(e) 23 ML Fe
(f) 27 ML Fe

Figure 3.12: Selection of LEED patterns of (a) 4 ML, (b) 6 ML, (c) 10 ML, (d) 19 ML, (e) 23 ML, and (f) 27 ML Fe films grown on Ir(001). All images are taken at a primary electron energy of 100 eV. The films are annealed at 900 K before the LEED experiments.

Chapter 4

Results

Investigation of high wave-vector magnons in ultrathin Fe films has been so far restricted to Fe(110) films grown on W(110) only [9, 20, 25]. In the SPEELS measurements on the Fe(001)/GaAs(001) system only broad peaks without any obvious dispersion have been observed [29]. For the case of Fe(001)/Ag(001), the measurement has only been performed on a thick (20 ML) Fe film and only a specific wave-vector has been measured [30]. The observed peak at relative high energy region (1-3 eV) is attributed to the exchange splitting. In this chapter, the experimental results of magnon excitations at Fe(111) and Fe(001) surfaces, measured by spin-polarized electron energy loss spectroscopy within the whole surface Brillouin zone, are presented. In section 4.1, the results obtained on 2 ML Fe(111) on 2 ML Au(111)/ W(110) are shown. The results of the measurements on 2 ML Fe(110)/W(110) with a Au overlayer are discussed in section 4.2. In section 4.3, measurements on Fe(001) films grown on Ir(001) are presented including the results obtained on 6 ML Fe along two different crystallographic axes, namely [100]- and [110]-directions ($\bar{\Gamma}$-$\bar{\mathrm{X}}$ and $\bar{\Gamma}$-$\bar{\mathrm{M}}$ in the reciprocal space) and the ones measured on other Fe thicknesses ranging from 5 to 27 ML along the $\bar{\Gamma}$-$\bar{\mathrm{X}}$ direction. A detailed discussion of the experimental results will be given in Chapter 5.

4.1 The Fe/Au/W(110) system

According to the IV-LEED experiments shown in section 3.3.1, Fe films relax from fcc Fe(111) to bcc Fe(110) structure if the thickness of the film is above 2 ML. Therefore, we restrict our SPEELS measurements to the samples composed of 2 ML Fe grown on 2 ML Au/W(110) in order to investigate the role of surface structure on the magnon excitations.

We perform longitudinal MOKE measurements at 300 K with the field along the W[$1\bar{1}0$]-direction (Fe[$\bar{2}11$]-direction) and then magnetize the film along the same direction before the SPEELS measurement. The lattice geometry is shown in Fig. 4.1 (a). A typical hysteresis loop recorded on a 2 ML Fe on 2 ML Au/W(110) is presented in Fig. 4.1 (b). The rectangular-like hysteresis loop shows that the easy axis of the Fe thin films is parallel to the direction of the applied field. The SPEEL-spectra are obtained at the remanent state. No external magnetic field is applied during the SPEELS measurements. The scattering plane is parallel to the W[001]-direction (Fe[$01\bar{1}$]-direction). Typical SPEEL-spectra measured on 2 ML Fe grown on 2 ML Au/ W(110) are shown

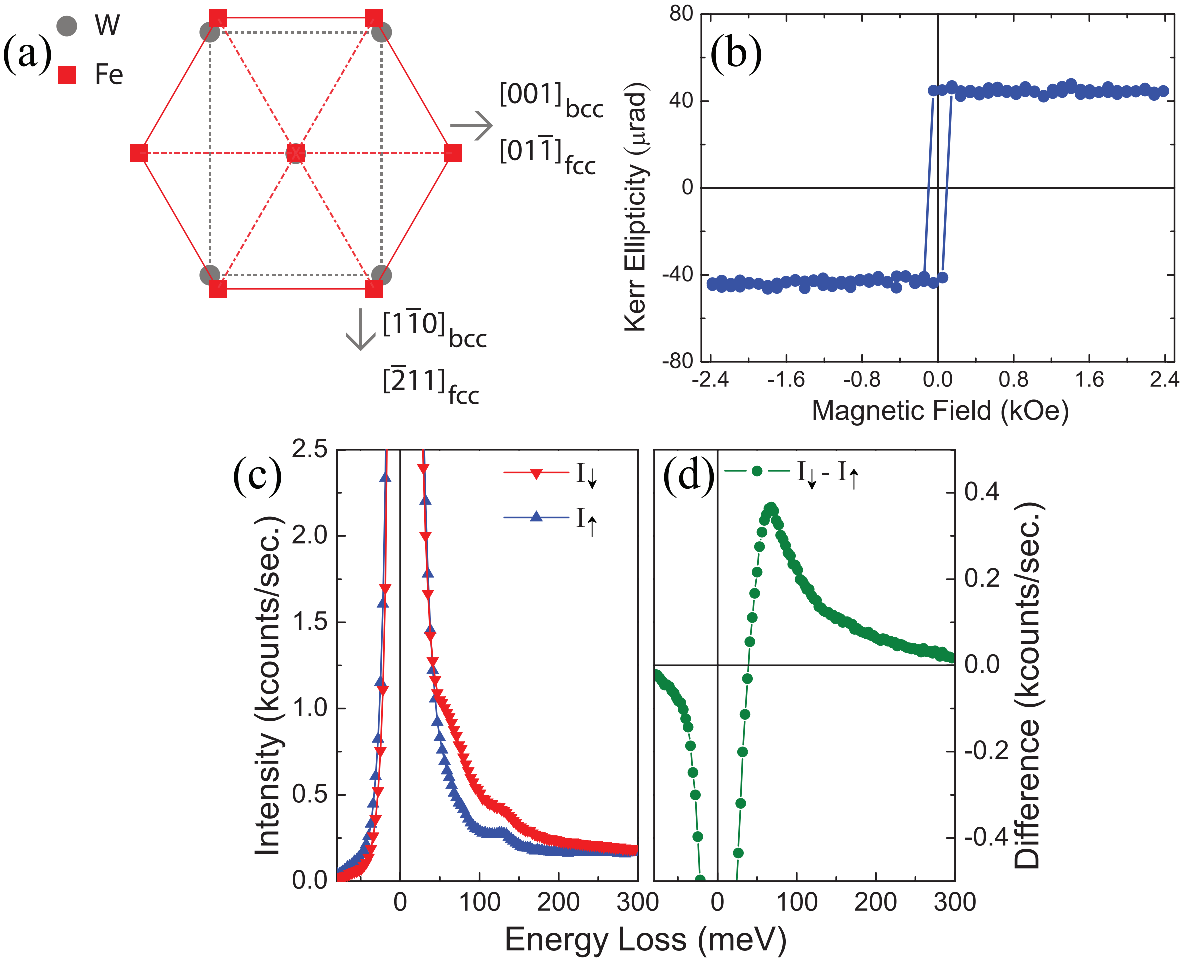

Figure 4.1: (a) A two-dimensional representation of the lattice geometry of fcc Fe(111) and bcc W(110) in real space. (b) The MOKE hysteresis loop obtained on 2 ML Fe/2ML Au/W(110) with a magnetic field applied along the Fe$_{fcc}$[$\bar{2}$11]-direction. (c) Typical SPEEL-spectra recorded on 2 ML Fe/2ML Au/W(110) at an in-plane wave-vector transfer of $\Delta K_{||}$=0.75 Å^{-1}. The incident electron energy is 3.96 eV, and the total energy resolution is about 14.9 meV. The intensity spectrum I$_{\downarrow}$ (I$_{\uparrow}$) is obtained using the incident electrons with the spin antiparallel (parallel) to the spin of majority electrons in the Fe film. The difference spectrum (I$_{\downarrow}$-I$_{\uparrow}$) is shown in (d). All the data are recorded at 300 K.

in Fig. 4.1 (c). I$_{\downarrow}$ (I$_{\uparrow}$) indicates the intensity of the scattered electrons when incoming electrons have the spin polarization antiparallel (parallel) to the spin of majority electrons in the Fe films. The in-plane wave-vector transfer ($\Delta K_{||}$) is 0.75 Å^{-1}, and the incident electron energy is 3.96 eV in this measurement with the energy resolution of around 14.9 meV. As mentioned in section 2.3, due to the conservation of total angular momentum, the incident electrons of minority character are allowed to excite magnons. Therefore, the peak at 68 meV in the minority channel (I$_{\downarrow}$) is due to the magnon excitation. In addition, the peaks at around 130 meV in both I$_{\downarrow}$ and I$_{\uparrow}$ spectra in Fig. 4.1 (c) are due to the vibrational excitations of hydrogen atoms adsorbed on the sample surface [71]. In the energy gain region (region with negative energy in Fig. 4.1 (c)), the

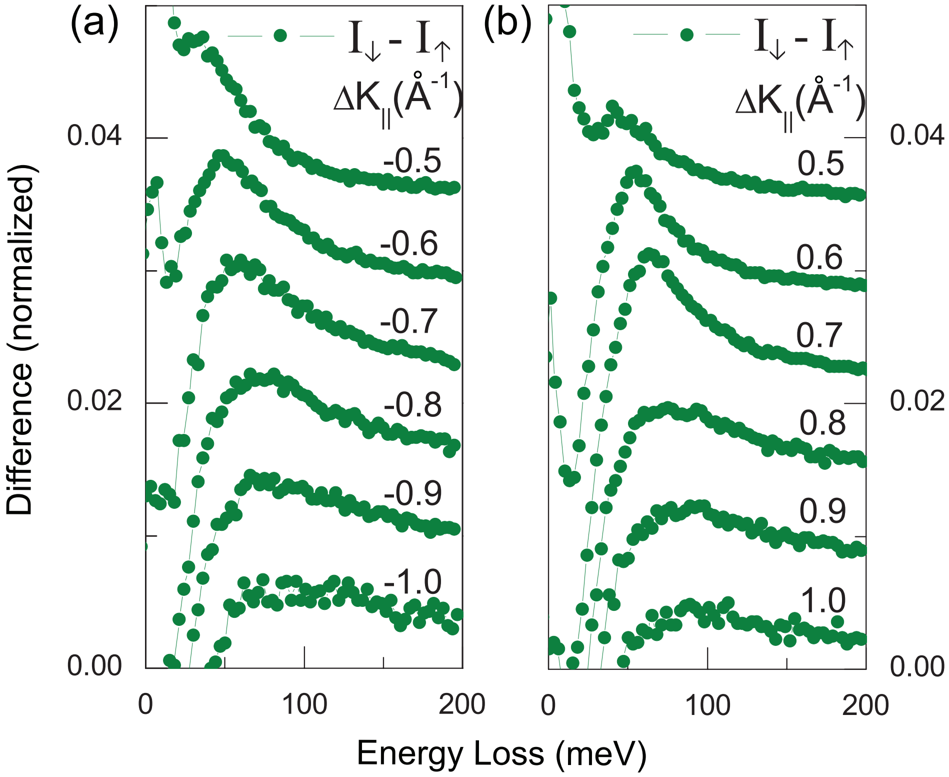

Figure 4.2: A series of difference spectra ($I_\downarrow$-$I_\uparrow$) measured on 2 ML Fe/2 ML Au/W(110) at different wave-vector transfers ($\Delta K_{||}$) from (a) -0.5 to -1.0 $Å^{-1}$ and (b) +0.5 to +1.0 $Å^{-1}$. For each $\Delta K_{||}$, the $I_\uparrow$ and $I_\downarrow$ are normalized to the sum of the quasi-elastic peaks ($I_\downarrow$+$I_\uparrow$). The difference spectra are obtained from the normalized $I_\uparrow$ and $I_\downarrow$ spectra. The incident electron energy is 3.96 eV with the energy resolution of around 14.9 meV. The experiments are performed at 300 K.

$I_\uparrow$ spectrum is higher than the $I_\downarrow$ spectrum. This is attributed to the annihilation of the thermally excited magnons. In this case, only the incident electrons with majority character can annihilate magnons (see section 2.3 for more discussion).

The difference spectrum ($I_\downarrow$-$I_\uparrow$) is shown in Fig. 4.1 (d). In this spectrum, the spin-independent excitations, such as vibrational losses, are drastically reduced. The magnon excitations can be clearly identified in the difference spectrum. The analysis of the peak position and linewidth provides us the information on the magnon energy and lifetime, respectively [39]. The area under the excitation peak is regarded as the magnon intensity. Because of the exchange process during the scattering, the quasi-elastic peaks in the $I_\uparrow$ and $I_\downarrow$ spectra are often not identical. This fact results in a pronounced peak in the difference spectrum (Fig. 4.1 (d)) at zero energy loss. Since the intensity of the quasi-elastic peak is much higher than the one of the magnons signal, this sets a low energy limit to the loss energies that can be explored in the experiments depending on the energy resolution. In our SPEELS measurements, typical energy resolution is around 10 to 15 meV. Recently a high resolution spectrometer has developed in Jülich based on 143° deflectors [100, 101]. Magnons signal can be resolved down to $\Delta K_{||}$=0.2 $Å^{-1}$ and magnon energies of 15 meV with resolution of 7 meV. However, the set-up is

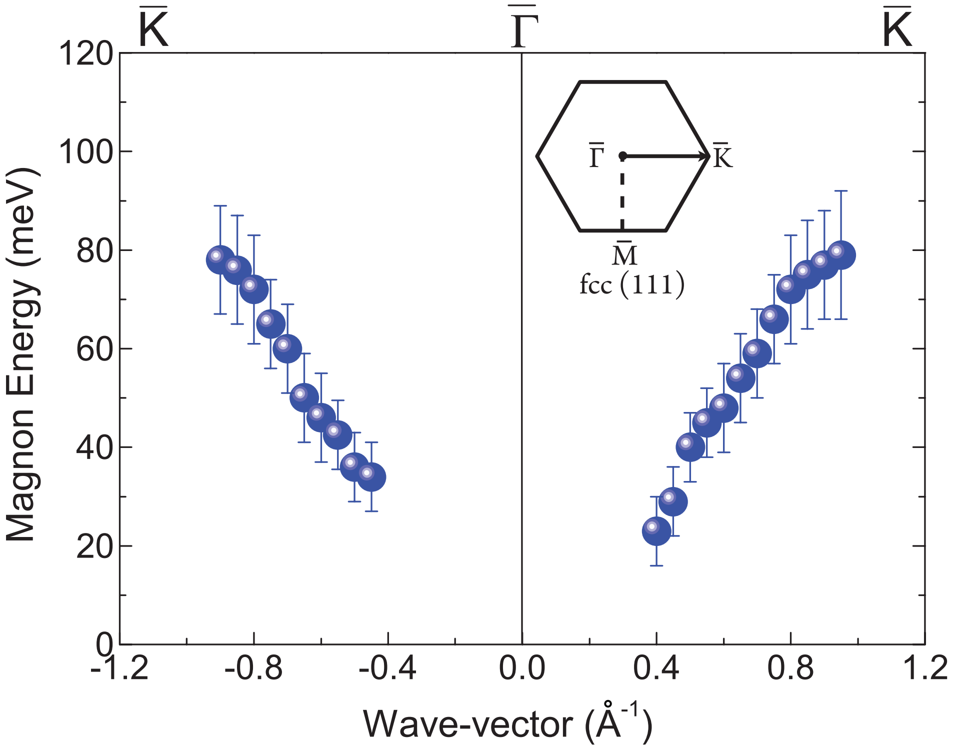

Figure 4.3: The magnon dispersion relation of a 2 ML Fe film grown on 2 ML Au/W(110) measured by SPEELS along the $\bar{\Gamma}$-$\bar{\mathrm{K}}$ direction. The data points represent the energy position of the maxima of the difference spectra shown in Fig. 4.2. The surface Brillouin zone boundary of an fcc crystal with (111)-surface is shown in the inset.

still not spin-resolved.

The magnon dispersion relation can be obtained by a series of SPEELS measurements with various in-plane wave-vector transfers, $\Delta K_{||}$. Two sets of difference spectra ($\mathrm{I}_{\downarrow}$- $\mathrm{I}_{\uparrow}$) with the in-plane wave-vector transfers, $\Delta K_{||}$, from -0.5 Å^{-1} to -1.0 Å^{-1} and from +0.5 Å^{-1} to +1.0 Å^{-1} are shown in Fig. 4.2 (a) and Fig. 4.2 (b), respectively. In order to have a clear comparison for different $\Delta K_{||}$, the intensity spectra are normalized. For a certain $\Delta K_{||}$, the maximum of the quasi-elastic peak in the sum ($\mathrm{I}_{\downarrow}$+$\mathrm{I}_{\uparrow}$) spectrum is taken as the normalization factor. The difference spectra are divided by this factor and shown as normalized difference spectra in Fig. 4.2. The magnon peak shifts from 40 to 90 meV as $\Delta K_{||}$ increases from 0.5 Å^{-1} to 1.0 Å^{-1}. A similar change can be observed while changing $\Delta K_{||}$ from -0.5 Å^{-1} to -1.0 Å^{-1}. The clear dispersion relation is the signature of the collective excitations. It is also found that the magnon peaks become much broader at high wave-vector transfers than at lower ones. This is mainly due to the strong damping of collective excitations to the spin-dependent single particle electron-hole pair excitations, *i.e.* Stoner excitations, as mentioned in section 2.1.2.

By plotting the magnon energies as a function of the wave-vector transfers, one obtains the magnon dispersion relation as shown in Fig. 4.3. The magnon dispersion relation is probed along the $\mathrm{Fe}_{fcc}[01\bar{1}]$-direction (the $\bar{\Gamma}$-$\bar{\mathrm{K}}$ direction in the reciprocal space). The conventional notation of the surface Brillouin zone boundary in an fcc crystal with (111)-surface is shown in the inset of Fig. 4.3. The surface Brillouin zone boundary along the $\bar{\Gamma}$-$\bar{\mathrm{K}}$ direction locates at 1.49 Å^{-1} for the pseudomorphically grown 2 ML Fe film on 2 ML Au(111) surface. The magnons are strongly damped into Stoner excitations at high wave-vector transfers. Hence, the magnon energies become difficult to define in the difference spectra for the wave-vector transfers higher than $\Delta K_{||}$=1.0 Å^{-1} (see Fig. 4.2). Therefore, the data points in this measurement stop at 1.0 Å^{-1}. The large uncertainty of the energy for the high wave-vector data points is due to the low intensity and broad energy distribution. The magnon dispersion relation is compared to the one measured on 2 ML Fe directly grown on W(110) [9]. This comparison will be discussed in detail in section 5.1.

4.2 The Au/Fe/W(110) system

SPEELS measurements on 2 ML Fe on W(110) have been performed and the full dispersion relation has been obtained [9, 19]. Here we perform the same experiments but with various thicknesses of Au overlayer. The main idea of this study is to investigate the role of a non-magnetic overlayer on the magnon excitation in the ferromagnetic film.

Fe films grow pseudomorphically on W(110) from the initial stage of growth up to 2 ML [19]. Therefore for this investigation we chose a 2 ML thick film. The sample is magnetized along the Fe[1$\bar{1}$0]-direction before the SPEELS measurements and measured at the remanent state. Typical SPEEL-intensity spectra measured on a 2 ML Fe film grown on W(110) are shown in Fig. 4.4 (a), and the ones measured on a system composed of 1 ML Au overlayer on 2 ML Fe grown on W(110) are presented in Fig. 4.4 (b). The scattering plane is parallel to the Fe[001]-direction. The in-plane wave-vector transfer ($\Delta K_{||}$) in both figures are 0.6 Å^{-1}, and the incident electron energy is 4 eV with the energy resolution of around 17 meV. Clear peaks at 55 meV, which are attributed to the magnon excitations, are shown in the minority channel ($\mathrm{I}_{\downarrow}$) in both figures. In the energy gain region, a clear shoulder in the majority channel ($\mathrm{I}_{\uparrow}$) represents the annihilation of the thermally excited magnons. The peaks at around 130 meV in both channels ($\mathrm{I}_{\downarrow}$ and $\mathrm{I}_{\uparrow}$) are due to the vibrational excitations of hydrogen atoms adsorbed on the sample surface [71]. In the Fig. 4.4 (b), there is a peak at around 60 meV in the majority channel ($\mathrm{I}_{\uparrow}$). This is caused by the oxygen adsorption on the sample surface since the measurement was performed around 3 hours later than the one in Fig. 4.4 (a) [71].

The difference spectra ($\mathrm{I}_{\downarrow}$-$\mathrm{I}_{\uparrow}$) are shown as green circles in Fig. 4.4. Both difference spectra have the same peak position at 55 meV (the same magnon energy). However, the peak width is clearly different. The broadening of the peak is a consequence of the shorter lifetime. In Fig. 4.5, a series of difference spectra measured on 2 ML Fe grown on W(110) with 0, 1, and 2 ML of Au overlayer at in-plane wave-vector transfers of $\Delta K_{||}$=0.6 Å^{-1} and $\Delta K_{||}$=0.5 Å^{-1} are shown. In order to have a better comparison of the peak width, they are scaled into the same peak intensity. The magnon energy stays nearly constant with increasing the thickness of Au overlayer, but the peak width increases at both wave-vector transfers. It implies that the lifetime of the magnons excited in the ferromagnetic Fe layer is getting shorter as the thickness of Au overlayer

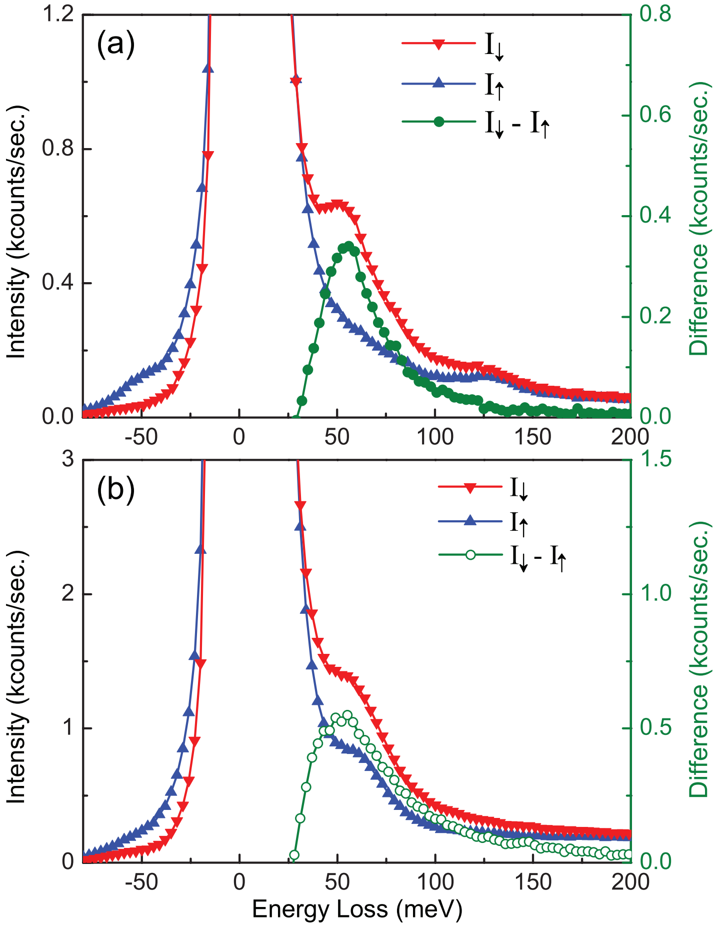

Figure 4.4: SPEEL-spectra measured on (a) 2 ML Fe/W(110) and (b) 1 ML Au/2 ML Fe/W(110) at an in-plane wave-vector transfer of $\Delta K_{||}$=0.6 Å^{-1}. The experiments are performed at 300 K. The incident electron energy is 4 eV, and the total energy resolution is about 17 meV. The intensity spectrum $I_{\downarrow}$ ($I_{\uparrow}$) is obtained using the incident electrons with the spin antiparallel (parallel) to the spin of majority electrons in the Fe film. The difference spectra ($I_{\downarrow}$-$I_{\uparrow}$) are shown as green circles.

increases [19]. The peak width of the spectra at $\Delta K_{||}$=0.5 Å^{-1} is smaller than the one at $\Delta K_{||}$=0.6 Å^{-1}, which is consistent with the results of the previous measurements by Zhang [19]. To extract the intrinsic linewidth of the magnons, one may fit the measured difference spectra by using a convolution of a Gaussian and a Lorentzian function. The Gaussian represents the instrumental broadening and the Lorentzian represents the intrinsic magnon signal. We will provide a quantitative representation of the magnon wave packets in time and space in section 5.2.

4.3 The Fe/Ir(001) system

Fe(001) films with a thickness of up to 10 ML grow pseudomorphically on Ir(001) with a constant in-plane film strain [16, 31, 32]. The room temperature ferromagnetic hysteresis loop is observed only above 5 ML [16]. Here we present our experimental

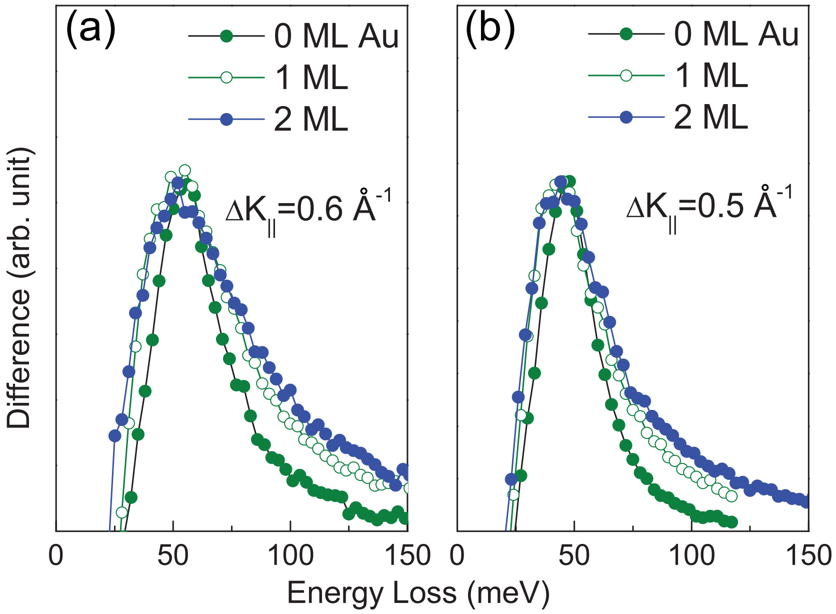

Figure 4.5: Difference spectra ($I_{\downarrow}$-$I_{\uparrow}$) obtained for various thicknesses of Au overlayer on 2 ML Fe/W(110) at in-plane wave-vector transfers of (a) $\Delta K_{||}$=0.6 Å^{-1} and (b) $\Delta K_{||}$=0.5 Å^{-1}. The intensities are rescaled into the same peak value in order to have a better comparison of the linewidths. The experiments are performed at 300 K.

results within 5 sections. First, the MOKE results measured on different thicknesses of Fe are presented. Then, the results of the SPEELS measurements on different film thicknesses [(*i*) 6 ML, (*ii*) 4-5 ML, (*iii*) 5-10 ML, and (*iv*) 10-27 ML Fe] are shown and discussed separately.

4.3.1 MOKE measurements

Longitudinal MOKE measurements are performed at room temperature on different thicknesses of Fe grown on Ir(001). The measurements are performed after the sample is annealed at about 900 K to improve the surface quality. The magnetic field is applied along the Fe[$0\bar{1}0$]-direction. The hysteresis loops are only obtained when the thickness is above 5 ML as seen in Fig. 4.6 (a). The Kerr ellipticity is plotted for different Fe thicknesses. The black squares are the Kerr ellipticities in saturation, and the red circles are the ones in remanence. According to the stress measurement performed by Tian, *et al.* [16, 32], in the region of 10 ML to 20 ML the Fe structure is relaxing from a bct structure to a bcc one. This fact is also revealed in the hysteresis loops. In Fig. 4.6 (b)-(e), the hysteresis loops obtained on different thicknesses of Fe are illustrated. From 5 ML to 10 ML, a rectangular-like hysteresis loop is obtained. No perpendicular magnetization is observed [16], indicating an in-plane easy magnetization axis. In addition, in the case of 6 ML Fe, the MOKE measurements are performed both with the fields applied along the Fe[$1\bar{1}0$]- and the Fe[$0\bar{1}0$]-direction as shown in Fig. 4.6 (c). Both loops show the easy-axis measurements. It indicates that the system has a very small magnetic anisotropy. Starting from 13 ML to 19 ML, the shape of the loops changes (see Fig. 4.6 (d)). The S-like loops indicate that the easy magnetization

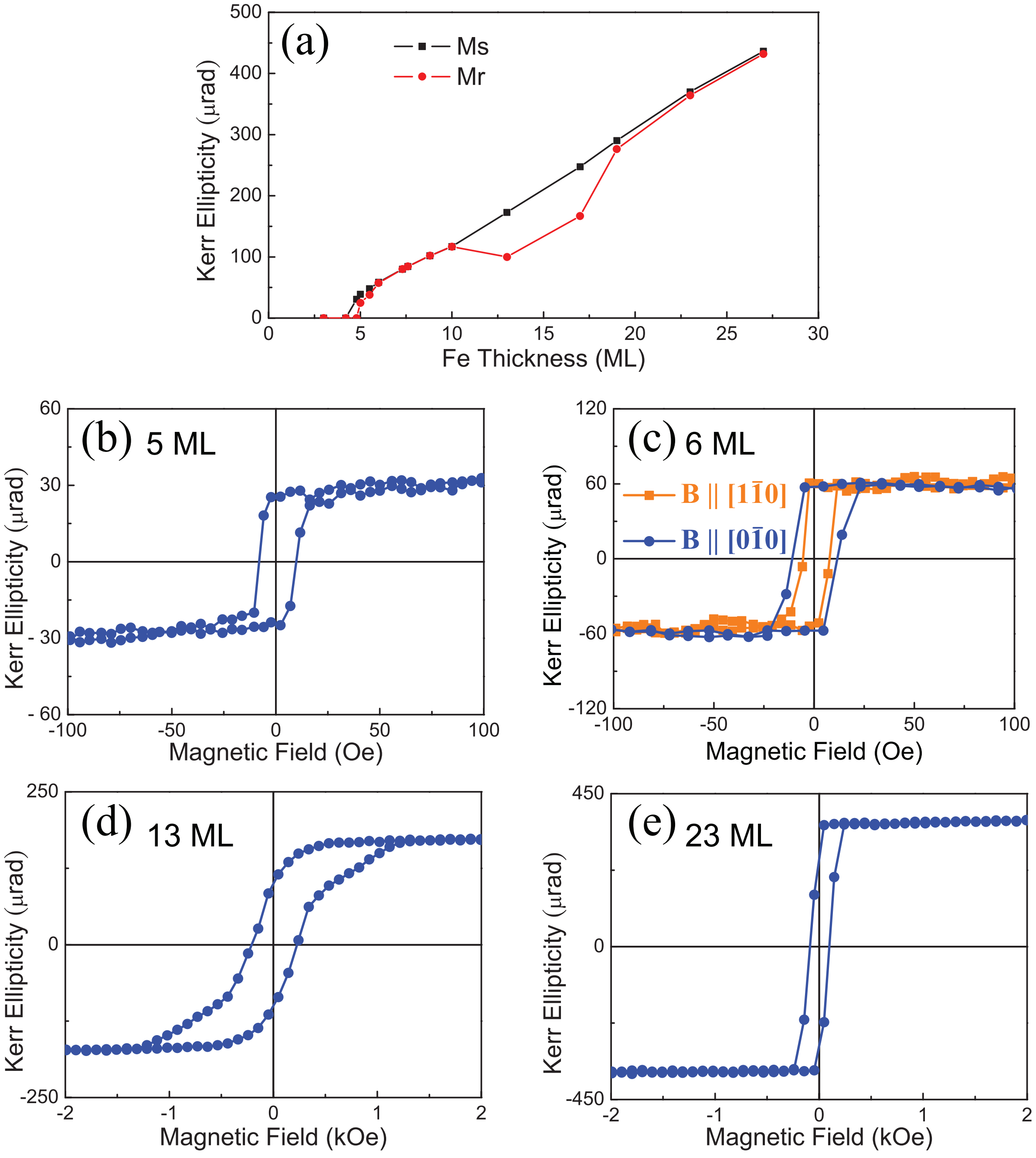

Figure 4.6: Longitudinal MOKE measurements on Fe films grown on Ir(001) with different thicknesses at 300 K. (a) Kerr ellipticity as a function of the Fe thickness in saturation (Ms) (black squares) and in remanence (Mr) (red circles). The hysteresis loops obtained on (b) 5 ML Fe, (c) 6 ML Fe, (d) 13 ML Fe, and (e) 23 ML Fe. All loops are obtained after annealing the sample at about 900 K. The magnetic field is applied along the [0$\bar{1}$0]-direction for the blue circles and along the [1$\bar{1}$0]-direction for the orange squares.

direction is changed. Since we did not observe this feature in the film without annealing, the anisotropy may be changed due to the annealing of the film. This indicates that the magnetic anisotropy of Fe films in this region from 13 to 19 ML grown on Ir(001) is sensitive to the annealing temperature. When the thickness is above 23 ML, the loops change back to the rectangular ones indicating the easy axis measurement as seen in Fig. 4.6 (e). According to the literature, the Fe films grow pseudomorphically as bct structure on Ir(001) from 2 ML to 10 ML [16, 31, 32]. Therefore, it is a great opportunity to measure the magnon dispersion relation on a series of Fe films in the pseudomorphically grown region from 5 ML to 10 ML and the relaxation region where the thickness is thicker than 10 ML. Furthermore, since it is still a mystery why there is no magnetic signal below 5 ML Fe at room temperature (4 ML at 180 K [16]), it is also interesting to investigate the magnon excitations in the transition region, where the thickness is thinner than 5 ML.

4.3.2 SPEELS measurements: 6 ML Fe

MOKE measurements are performed on 6 ML Fe grown on Ir(001) at 300 K with the field applied along the $[1\bar{1}0]$ and $[0\bar{1}0]$ directions as seen in Fig. 4.6 (c). Two similar rectangular hysteresis loops indicate that the magnetic anisotropy of the films is small. The sample is magnetized along the Fe$[0\bar{1}0]$- (or Fe$[1\bar{1}0]$-) direction before the SPEELS measurements and measured at the remanent state. The scattering plane is parallel to the Fe[100]- (or Fe[110]-) direction. Typical SPEEL-spectra measured on a 6 ML Fe film grown on Ir(001) at an in-plane wave-vector transfer of $\Delta K_{||}$=0.8 Å^{-1} are shown in Fig. 4.7. The measurement are performed along Fe[100] ($\bar{\Gamma}$-$\bar{\text{X}}$) in Fig. 4.7 (a) and Fe[110] ($\bar{\Gamma}$-$\bar{\text{M}}$) in Fig. 4.7 (b). The incident electron energy is 6 eV with the energy resolution of 16.9 meV. Along both directions, the magnon peak is pronounced in the energy loss region of the minority channel. The magnon energies could be more easily identified in the difference spectra ($I_\downarrow$-$I_\uparrow$). The peak position indicates the excitation energy.

Series of difference spectra with various wave-vector transfers ranging from $\Delta K_{||}$=0.5 Å^{-1} to $\Delta K_{||}$=0.8 Å^{-1} are shown in the Fig. 4.8 (a) for the probing direction along the $\bar{\Gamma}$-$\bar{\text{X}}$ direction and in the Fig. 4.8 (b) for the direction along the $\bar{\Gamma}$-$\bar{\text{M}}$ direction. The difference spectra show clear dispersion along both directions. However, the magnon energies are different starting from $\Delta K_{||}$=0.7 Å^{-1}. Therefore, magnon dispersion relation along different directions is not the same. In addition, the intensities of difference spectra in Fig. 4.8 (a) are larger than the ones in Fig. 4.8 (b). This is because experiments are performed on different substrates with two crystal cutting directions and the optimization condition of the electron beam is not exactly the same. Therefore, the intensity cannot be directly compared.

By plotting the magnon energies as a function of the wave-vector transfer, the magnon dispersion relation is obtained for both probing directions (see Fig. 4.9). The magnon dispersion relation of 6 ML Fe on Ir(001) over the whole surface Brillouin zone is experimentally measured along the $\bar{\Gamma}$-$\bar{\text{X}}$ and $\bar{\Gamma}$-$\bar{\text{M}}$ directions. This is the first experimentally measured magnon dispersion relation on Fe(001) surface and also for the first time along different symmetry directions. The length of $\bar{\Gamma}$-$\bar{\text{X}}$ is 1.16 Å^{-1}, and the one of $\bar{\Gamma}$-$\bar{\text{M}}$ is 1.64 Å^{-1}, assuming the in-plane lattice constant of Fe is 2.72

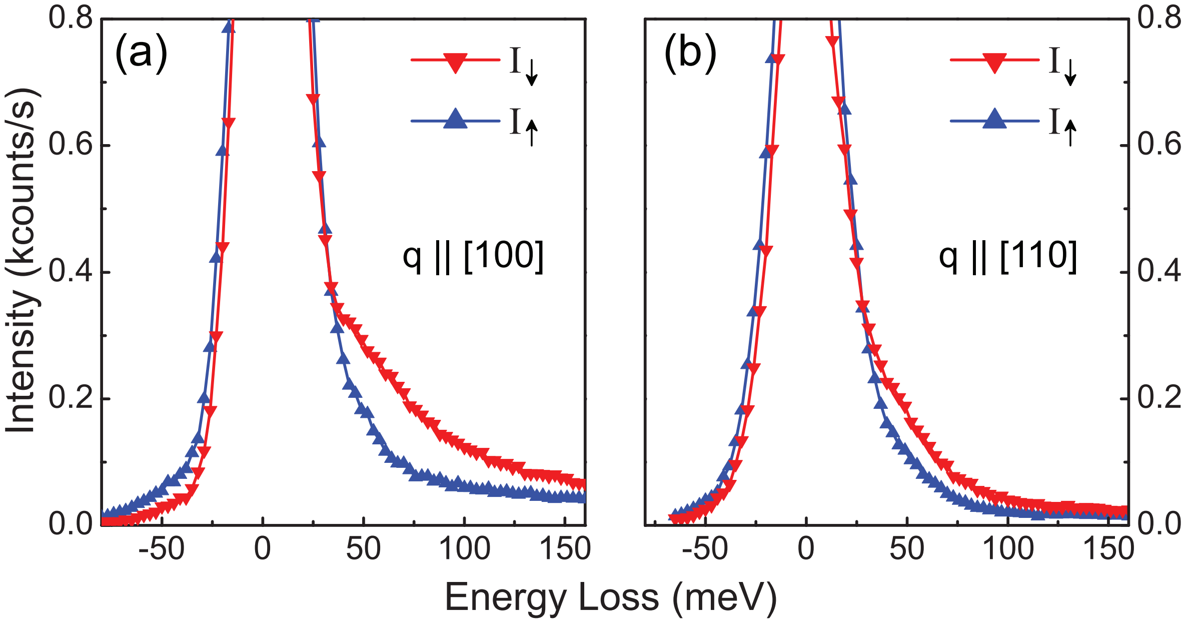

Figure 4.7: Typical SPEEL-spectra recorded on 6 ML Fe/Ir(001) at an in-plane wave-vector transfer of $\Delta K_{||}$=0.8 Å^{-1} probed along the (a) Fe[100]- and (b) Fe[110]-directions. The experiments are performed at 300 K. The incident electron energy is 6 eV, and the total energy resolution is about 16.9 meV. The intensity spectrum $I_{\downarrow}$ ($I_{\uparrow}$) is obtained using the incident electrons with the spin antiparallel (parallel) to the spin of majority electrons in the Fe film.

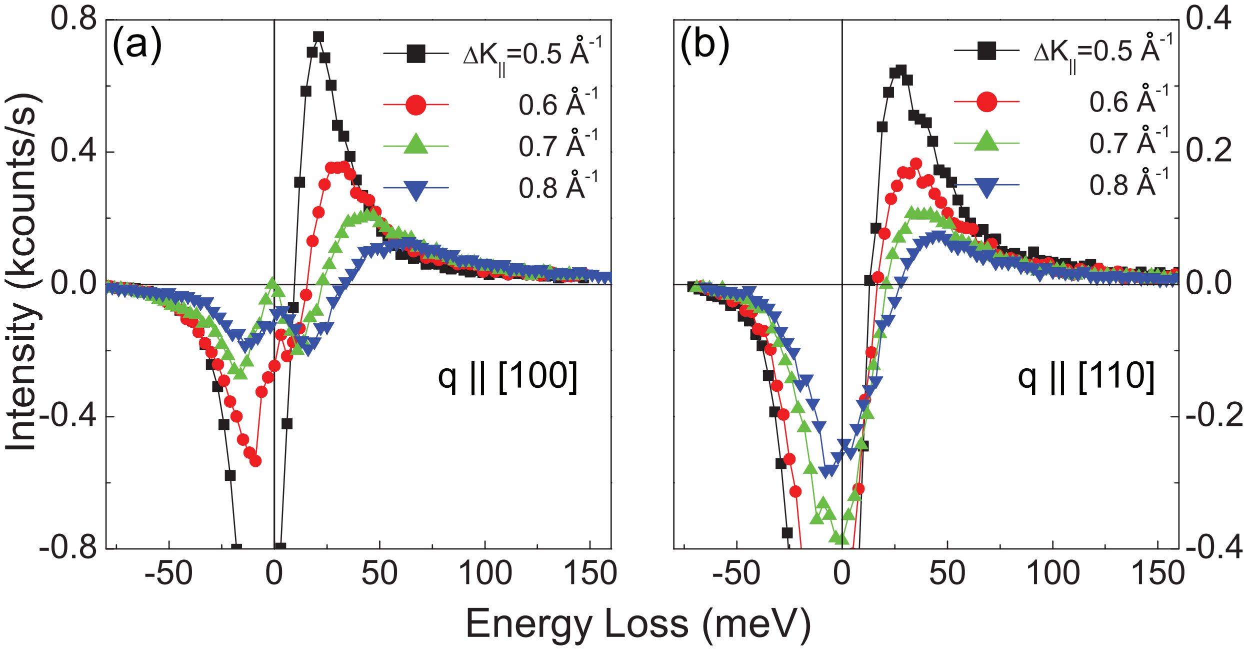

Figure 4.8: Series of difference spectra ($I_{\downarrow}$-$I_{\uparrow}$) at in-plane wave-vector transfers from $\Delta K_{||}$=0.5 Å^{-1} to $\Delta K_{||}$=0.8 Å^{-1} probed along the (a) Fe[100]- ($\bar{\Gamma}$-$\bar{X}$) and (b) Fe[110]- ($\bar{\Gamma}$-$\bar{M}$) directions.

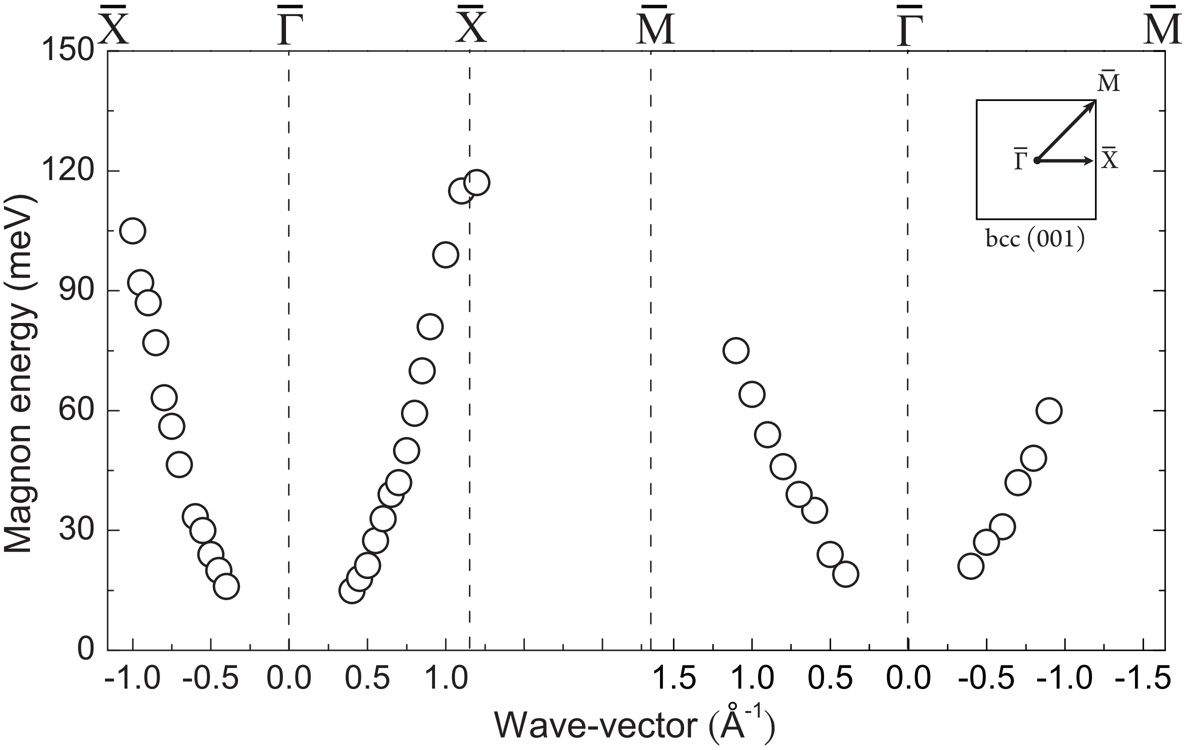

Figure 4.9: The magnon dispersion relation of 6 ML Fe grown on Ir(001) measured within the whole surface Brillouin zone. The experiments are performed at 300 K. The surface Brillouin zone boundary of a bcc crystal with (001)-surface is shown in the inset. The zone boundary along the $\bar{\Gamma}$-$\bar{X}$ direction is at 1.16 Å^{-1}, and the one along the $\bar{\Gamma}$-$\bar{M}$ direction is at 1.64 Å^{-1}.

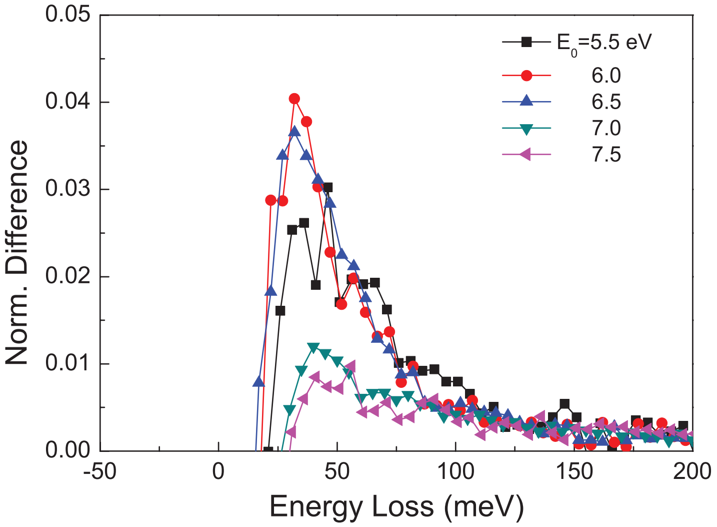

Figure 4.10: Normalized difference spectra measured on 6 ML Fe/Ir(001) at an in-plane wave-vector transfer of $\Delta K_{||}$=0.6 Å^{-1} with a series of incident electron energies from 5.5 eV to 7.5 eV. The normalization factor is the respective intensity of the quasi-elastic peak in the I_{sum} ($I_{\downarrow}$+$I_{\uparrow}$) spectrum.

Å (since Fe grows pseudomorphically on Ir(001) substrate up to 10 ML). The data points of the measurement along the $\bar{\Gamma}$-$\bar{\mathrm{M}}$ direction are only up to $\Delta K_{||}$=1.1 Å^{-1}. The reason is that the intensity of the difference spectra is too low for $\Delta K_{||} > 1.1$ Å^{-1}. To overcome this limitation, one may increase the incident electron energy to lower down the scattering angle. However, the magnon intensity also strongly depends on the incident electron energy as seen in Fig. 4.10. By measuring the magnon intensity as a function of the incident electron energy from 5.5 eV to 7.5 eV, it is found that the highest magnon intensity appears at E_0=6 eV. The magnon intensity strongly decreases when increasing the incident energy. Therefore, it is difficult to get the information for higher wave-vector transfers close to the $\bar{\mathrm{M}}$-point. In addition, the dispersion relation along $\bar{\mathrm{X}}$-$\bar{\mathrm{M}}$ is not measurable by using our present experimental set-up since it requires the accessibility of rotating the sample in the sample plane.

The first step of analyzing these results is to take a simple Heisenberg model and try to describe the experimentally measured dispersion relation. This will be discussed in detail in section 5.3.

4.3.3 SPEELS measurements: 4-5 ML Fe

The room temperature ferromagnetic hysteresis loop only appears when the thickness is above 5 ML as seen in Fig 4.6. In Fig. 4.11, the SPEEL-spectra obtained on 4.2 ML, 4.8 ML, and 5 ML Fe grown on Ir(001) at an in-plane wave-vector transfer of $\Delta K_{||}$=0.8 Å^{-1} are presented. The incident electron energy is 6 eV with the energy resolution of around 15 meV. The respective results of longitudinal MOKE measurements are shown in the inset. In the difference spectrum, the intensity is almost zero for the measurement on a 4.2 ML Fe film as shown in Fig. 4.11 (a). For the measurement on a 4.8 ML Fe film (see Fig. 4.11 (b)), the $I_{\downarrow}$ channel is slightly deviated from $I_{\uparrow}$ channel in the energy loss region. In other words, the ferromagnetic magnon signal appears, but the intensity is still very weak.

When the thickness reaches 5 ML, a clear shoulder appears in the $I_{\downarrow}$ channel in the energy loss region indicating the evident magnon excitations (see Fig. 4.11 (c)). The magnon energy stays at the same value as the one on 4.8 ML Fe. A typical ferromagnetic hysteresis loop obtained on the 5 ML Fe/Ir(001) is also shown in the inset of Fig. 4.11 (c). The difference spectra obtained on 4.8 ML, 5 ML, and 6 ML Fe at $\Delta K_{||}$=0.8 Å^{-1} are compared in Fig. 4.11 (d). The magnon energy is slightly increased by about 6 meV when the thickness is increased from 5 ML to 6 ML. Meanwhile, the magnon intensity is largely enhanced. The SPEELS measurements on non-ferromagnetic films (1-4 ML Fe) are shown in the following subsection.

4.3.4 SPEELS measurements: 1-4 ML Fe

As it is discussed in section 4.3.1, no ferromagnetic signal could be observed by MOKE for the Fe films of less than 4 ML in thickness. The SPEELS measurements are performed on 1 to 4 ML Fe. The difference spectra show no signature of ferromagnetic magnons.

In Fig. 4.12, normalized I_{sum} ($I_{\downarrow}$+$I_{\uparrow}$) measured on 1 to 4 ML Fe at an in-plane wave-vector transfer of $\Delta K_{||}$=0.6 Å^{-1} are shown as solid diamonds. The difference

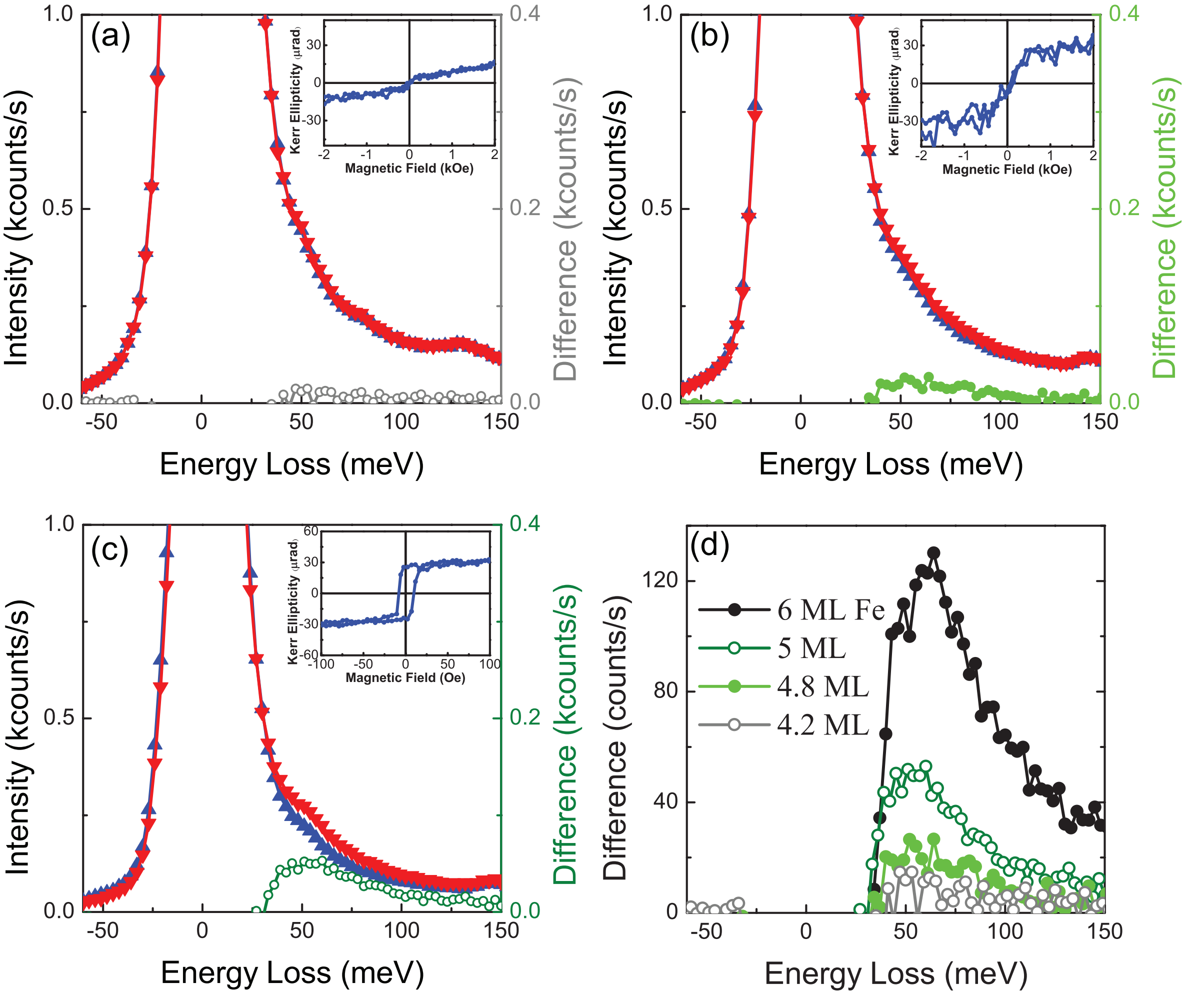

Figure 4.11: SPEEL-spectra $I_\downarrow$ (red), $I_\uparrow$ (blue), and their difference for (a) 4.2 ML, (b) 4.8 ML, and (c) 5 ML Fe grown on Ir(001) at an in-plane wave-vector transfer of $\Delta K_{||}$=0.8 Å^{-1}. The experiments are performed at 300 K. The scattering plane is parallel to the Fe[100]-direction. All data are obtained using the incident electron energy of 6 eV with the energy resolution of about 15 meV. The hysteresis loops obtained by the longitudinal MOKE measurements with the field applied along the [0$\bar{1}$0]-direction are shown in the insets. The difference ($I_\downarrow$-$I_\uparrow$) spectra at $\Delta K_{||}$=0.8 Å^{-1} for 4.8 ML, 5 ML, and 6 ML are plotted together for comparison in (d).

spectrum ($I_\downarrow$-$I_\uparrow$) measured on 5 ML Fe is also shown as open circles for the indication of the energy position of the magnon excitations in the ferromagnetic films. In I_{sum} spectra, the peaks at around 50, 78, and 130 meV are the vibrational excitations of the adsorption of oxygen, carbon monoxide, and hydrogen, respectively, coming from the residual gasses in the chamber. The peaks show a weak dispersion when changing the wave-vector. Moreover, they become more pronounced when keeping the sample longer in UHV. We see a tail-like feature in the energy loss range of 20-40 meV, which is marked as a gray-shaded region in Fig. 4.12. In the shaded gray region, the tail of the spectrum seems to get larger when increasing the film thickness. However, there is no separate peak or spin contrast, it is difficult to define these excitations. As the

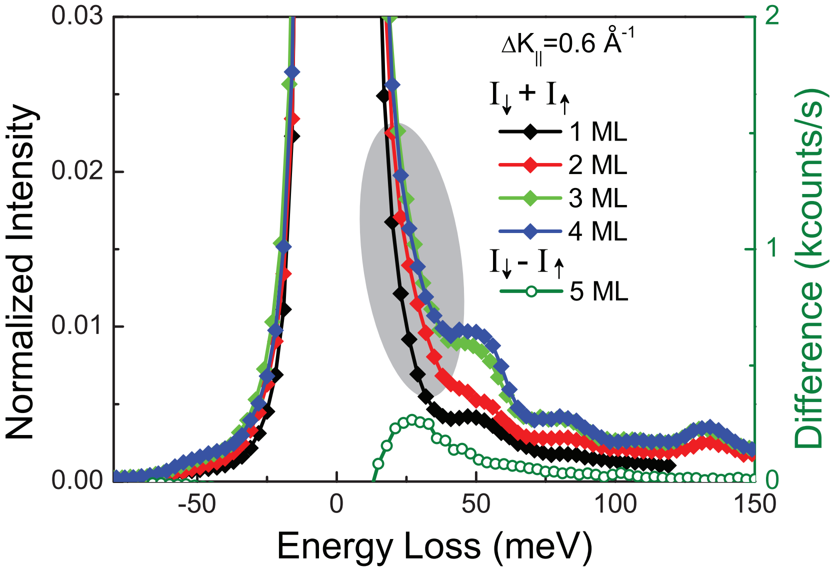

Figure 4.12: Normalized SPEEL-spectra I$_\downarrow$+I$_\uparrow$ measured on 1-4 ML Fe (solid diamonds), and the difference spectrum (I$_\downarrow$-I$_\uparrow$) obtained on 5 ML Fe grown on Ir(001) (open circles) at an in-plane wave-vector transfer of $\Delta K_{||}$=0.6 Å^{-1}. The experiments are performed at 300 K.

intensity of the quasi-elastic peak in each measurement is different [370k (for 1 ML), 300k (for 2 ML), 220k (for 3 ML), and 260k (for 4 ML) counts/sec.], one cannot make a definite conclusion.

4.3.5 SPEELS measurements: 5-10 ML Fe

Normalized difference spectra obtained on various thicknesses of Fe are shown in Fig. 4.13 (a) for the case of $\Delta K_{||}$=0.6 Å^{-1} and in Fig. 4.13 (b) for the case of $\Delta K_{||}$=0.8 Å^{-1}. The normalization factor is the respective intensity of the quasi-elastic peak in I$_\downarrow$+I$_\uparrow$ spectrum. At $\Delta K_{||}$=0.6 Å^{-1}, the magnon energies are almost the same from 6 ML to 10 ML. At $\Delta K_{||}$=0.8 Å^{-1}, the excitation energy in 10 ML Fe becomes slightly lower than the one in 6 and 8 ML (see Fig. 4.13 (b)).

In Fig. 4.13 (c), the magnon dispersion relation probed on 5.5 ML to 10 ML Fe along the $\bar{\Gamma}$-$\bar{\mathrm{X}}$ direction is shown. The dispersion relation stays similar up to the zone boundary within the uniformly strained region. The magnon intensity of 5 ML Fe is much weaker than the one of 5.5 ML since the remanence is much smaller. In this case, the error bars in the magnon energies are large, and hence we only take the data measured on 5.5 ML Fe. Although the dispersion relation is very similar within the error bars in the uniformly strained region, the magnon energies are slightly departed from the one of 6 ML for the case of 5.5 ML and 10 ML. The magnon energies of 5.5 ML Fe are all lower than the ones of 6 ML, especially close to the zone boundary (see the red triangles in Fig. 4.13 (c)). This indicates that the exchange interaction on 5.5 ML surface is slightly weaker than the one on 6 ML. The magnon energies of 10 ML Fe at lower wave-vectors are slightly higher than the ones of 6 ML (see the diamonds in Fig. 4.13 (c)), but the energies are slightly lower at $\Delta K_{||}$=0.8 Å^{-1} (see Fig. 4.13 (b)).

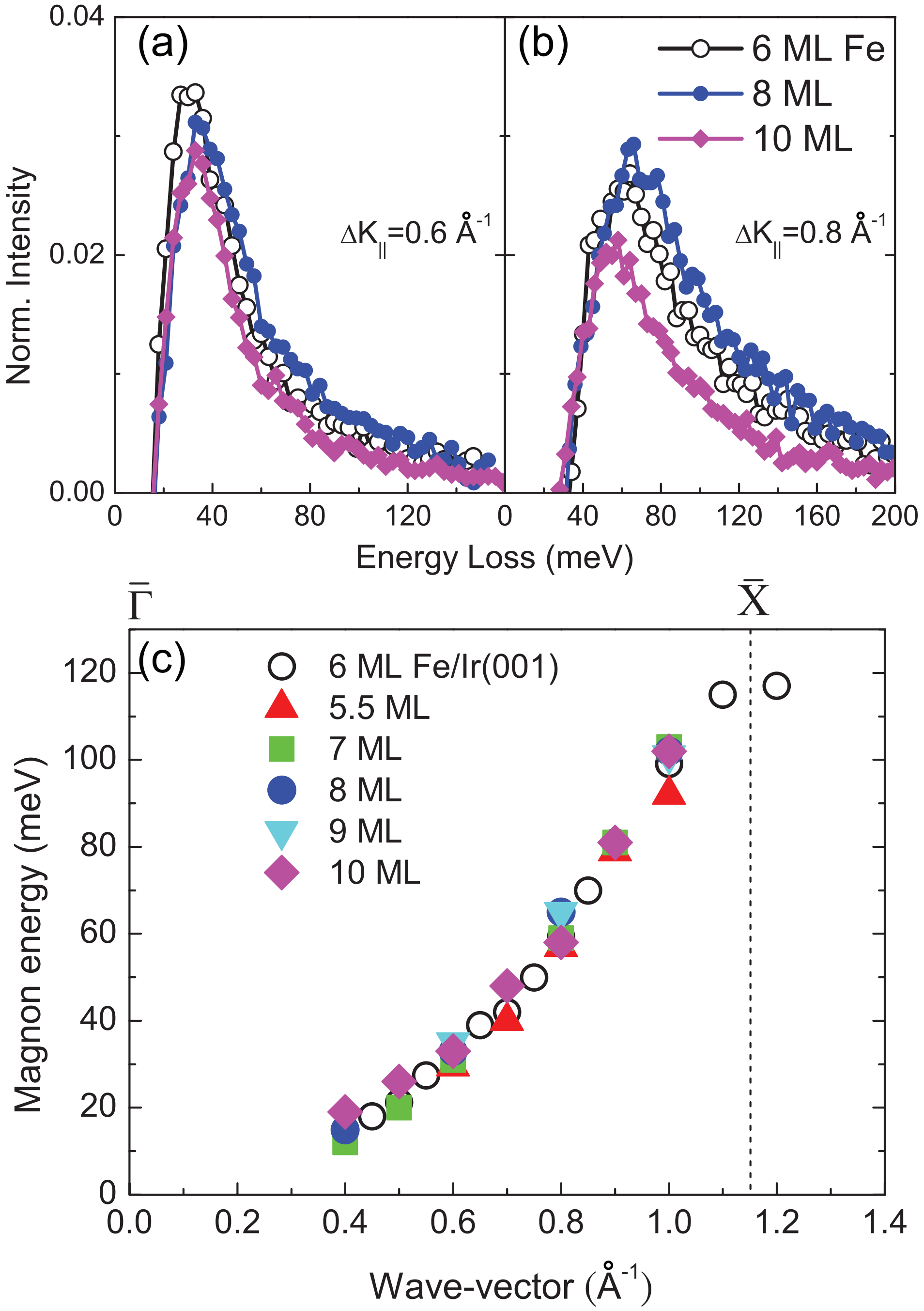

Figure 4.13: Normalized difference spectra measured at the in-plane wave-vector transfer of (a) $\Delta K_{||}$=0.6 Å^{-1} and (b) $\Delta K_{||}$=0.8 Å^{-1}. The normalization factor is the respective intensity of the quasi-elastic peak in the I_{sum} ($I_{\downarrow}$+$I_{\uparrow}$) spectrum. (c) The magnon dispersion relation measured along the $\bar{\Gamma}$-$\bar{X}$ direction on various thicknesses of Fe grown on Ir(001) in the pseudomorphic growth region (5-10 ML). The zone boundary is at 1.16 Å^{-1}.

This might be due to the fact that 10 ML is already the limit of the uniform strain region. The films have a tendency to relax to bulk-like films. This will be discussed in the next section.

4.3.6 SPEELS measurements: 10-27 ML Fe

According to the literature [16, 31, 32] and the LEED patterns shown in section 3.3.2, the Fe films start to relax when the thickness is above 10 ML. As seen in the MOKE measurements (Fig. 4.6), there may be a different domain structure on the film surface because of the relaxation of Fe films. The easy axis of some domains is perpendicular to the magnetization direction. This speculation is supported by the results of the SPEELS measurements. The 13 ML and 17 ML Fe grown on Ir(001) are measured by SPEELS, and the magnon intensity is almost zero. This may be due to the fact that the magnetization direction is no longer perpendicular to the scattering plane. Starting from 19 ML, the magnon intensity is gradually increased, but it is still very weak. We show the results only for 6 ML, 23 ML, and 27 ML in Fig. 4.14. The in-plane wave-vector transfer in this case is $\Delta K_{||}$=0.6 Å^{-1} [Fig. 4.14 (a)] and $\Delta K_{||}$=1.0 Å^{-1} [Fig. 4.14 (b)]. The magnon intensities on the relaxed films are much lower than the one of the 6 ML film. However, the magnon energies of the relaxed films are higher at $\Delta K_{||}$=0.6 Å^{-1} (middle of the surface Brillouin zone) and lower at $\Delta K_{||}$=1.0 Å^{-1} (close to the surface Brillouin zone boundary).

In Fig. 4.14 (c), the magnon dispersion relation measured on the thick Fe films from 19 ML to 27 ML is shown and compared to the one probed on 6 ML. The surface Brillouin zone boundary of the relaxed films is at 1.10 Å^{-1} if we take the lattice constant as the one of the bulk Fe (a_0 = 2.866Å). Starting from 19 ML, the Fe film is totally relaxed to a bulk-like film, therefore the magnon dispersion relation changes to a similar result of our previous measurements performed on thick Fe films (24 ML) grown on W(110) [19]. This observation and comparison will be discussed in detail in section 5.3.3.

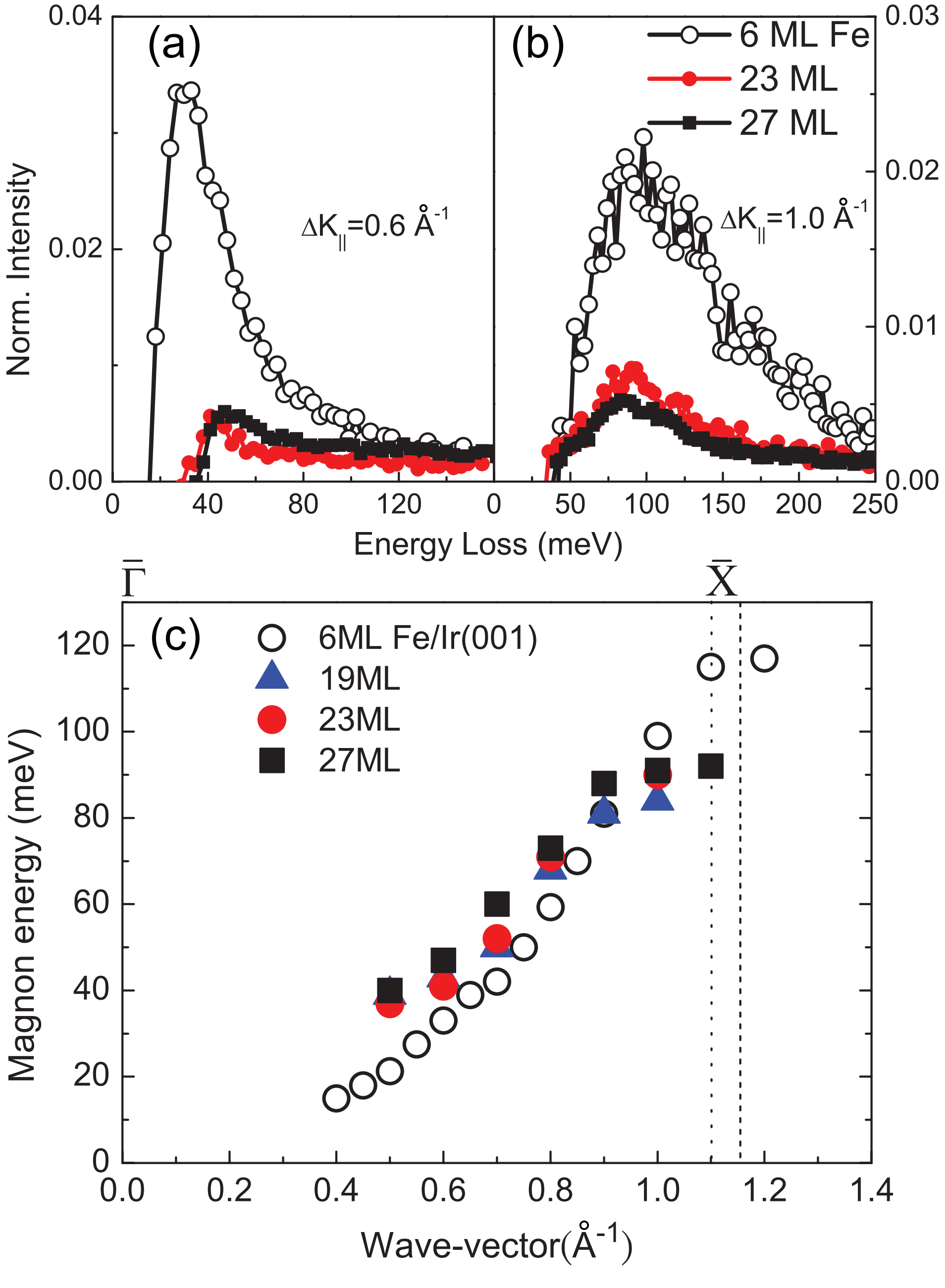

Figure 4.14: Normalized difference spectra obtained on 6 ML, 23 ML, and 27 ML Fe at an in-plane wave-vector transfer of (a) $\Delta K_{||}$=0.6 Å^{-1} and (b) $\Delta K_{||}$=1.0 Å^{-1}. The normalization factor is the respective intensity of the quasi-elastic peak in the I_{sum} ($I_{\downarrow}+I_{\uparrow}$) spectrum. (c) The magnon dispersion relation measured along the $\bar{\Gamma}$-$\bar{X}$ direction on thick Fe (>10ML) films grown on Ir(001) and compared to the one of 6 ML. The zone boundary of the relaxed film is at 1.10 Å^{-1} shown as the dotted line, and the one of the 6 ML film is at 1.16 Å^{-1} shown as the dashed line.

Chapter 5

Discussion

In this chapter, first, the magnon dispersion relation probed on 2 ML Fe grown on 2 ML Au/W(110) is compared to the one of 2 ML Fe directly grown on W(110). The Heisenberg model is applied to estimate the effective exchange parameter in both cases. The experimental results are compared to the first-principles adiabatic spin dynamics calculations based on density-functional theory (DFT) in order to better understand the role of the electronic structure on the magnetic exchange interaction. The calculations are performed by Arthur Ernst at Max Planck Institute in Halle. A quantitative analysis of the magnon lifetime in 2 ML Fe grown on W(110) with different thicknesses of Au overlayer is presented in section 5.2.

In section 5.3, the experimental results of Fe films grown on Ir(001) with different thicknesses are presented and discussed based on the Heisenberg model. We will also provide a comparison to the theoretical calculations within the adiabatic approach.

5.1 The Fe/Au/W(110) system

The signature of high wave-vector magnon excitations has been first observed by Kirschner, *et al.* [7] on an ultrathin Fe film with a thickness of 5 ML. Later on the magnon dispersion relation has been probed over the whole surface Brillouin zone on a 2 ML thick Fe(110)/W(110) film. [9, 19]. A nonmonotonic thickness dependence of magnon energy in Fe(110) films has also been discussed [25]. Here, we present the results of the magnon dispersion relation probed in a metastable phase of Fe with (111) surface orientation grown on Au(111)/W(110). We compare the results to the ones of the Fe(110)/W(110) system. Please note that in all samples discussed in this section the thickness of Fe layer is kept constant at 2 ML. The thickness of the Au film in Fe/Au/W(110) structure has also been chosen to be 2 atomic layers. (For further discussion concerning the reason of choosing this thickness, see section 3.3.1.)

5.1.1 Estimation of the effective exchange parameters

In Fig. 5.1, the magnon dispersion relation obtained on 2 ML Fe/Au/W(110) is illustrated as solid circles. The open circles are the experimental results on 2 ML Fe/W(110) [9]. It is obvious that the magnon energies in Fe(111)/Au(111)/W(110) are smaller than the ones in Fe(110)/W(110). In the measurements on Fe(110)/W(110),

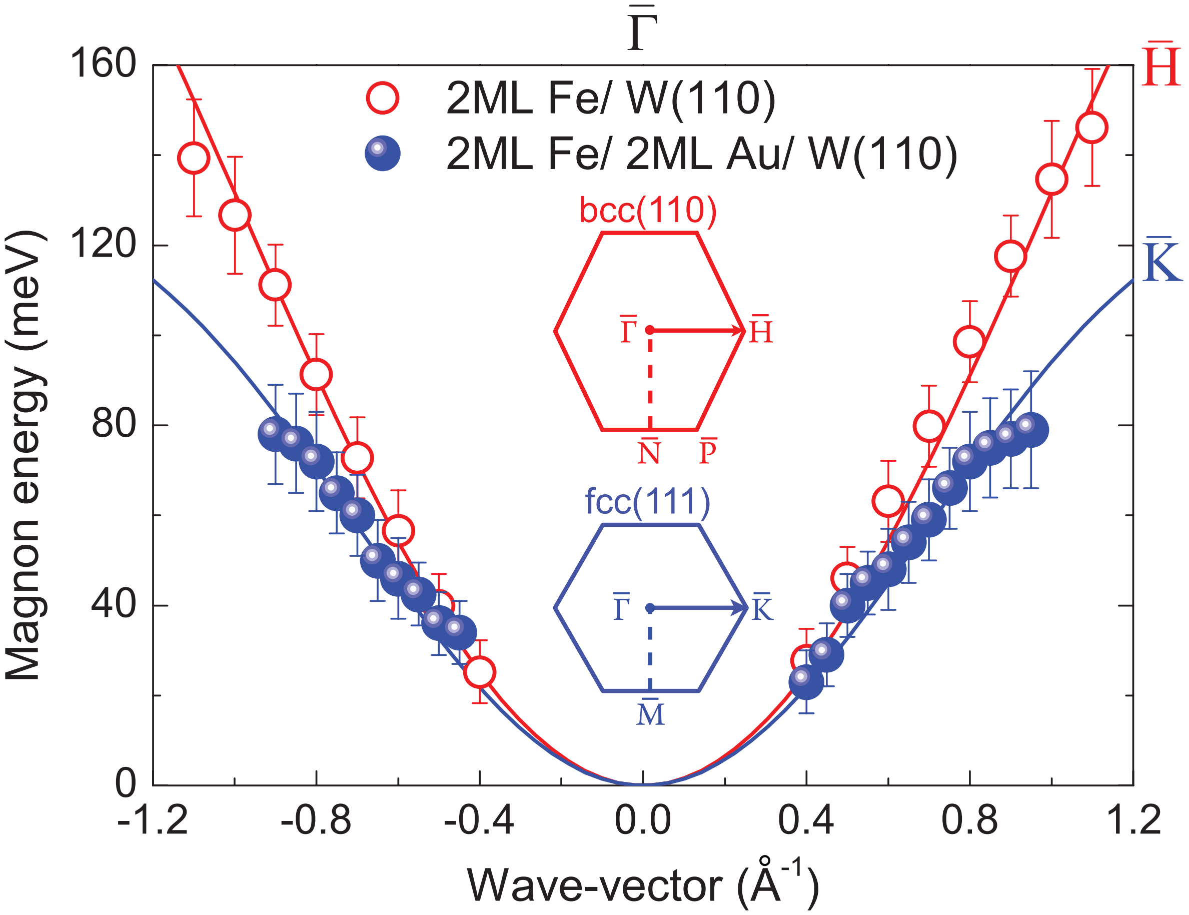

Figure 5.1: The magnon dispersion relation measured on a 2 ML Fe film on 2 ML Au on W(110) at room temperature along the $\bar{\Gamma}$-$\bar{\text{K}}$ direction is shown as blue solid circles. The results obtained on a 2 ML Fe film directly grown on W(110) along the $\bar{\Gamma}$-$\bar{\text{H}}$ direction are shown as red open circles [9]. The solid lines are the fits based on the nearest neighbor Heisenberg model. The fitting parameters are J_NS= 5.6 meV for the blue curve and J_NS=11.6 meV for the red curve. The surface Brillouin zones of a bcc crystal with (110)-surface and an fcc crystal with (111)-surface are shown in the inset. The surface Brillouin zone boundaries are both at 1.49 Å^{-1} along the $\bar{\Gamma}$-$\bar{\text{H}}$ and $\bar{\Gamma}$-$\bar{\text{K}}$ directions.

the magnon dispersion relation is probed along the $\bar{\Gamma}$-$\bar{\text{H}}$ direction. If one assumes that the Fe(110) film takes the same lattice parameters as W(110), the surface Brillouin zone boundary along the $\bar{\Gamma}$-$\bar{\text{H}}$ direction is at 1.49 Å^{-1}. This assumption is fairly valid, since Fe(110) films grow pseudomorphically on W(110) [102, 103]. In the case of Fe/Au/W(110), the surface orientation of Fe is (111)-surface and hence the magnon dispersion relation is probed along the $\bar{\Gamma}$-$\bar{\text{K}}$ direction. The surface Brillouin zone boundary along the $\bar{\Gamma}$-$\bar{\text{K}}$ direction is also at 1.49 Å^{-1} if we take the value of 2.82 Å as the in-plane nearest neighbor distance [93].

The effective exchange coupling constant may be estimated by using a simple Heisenberg model as discussed in section 2.1.1. The magnon dispersion relation can be obtained by finding the eigenvalues of the Heisenberg spin Hamiltonian. Starting from

Eq. 2.7, considering only the nearest neighbor interactions and taking a slab consists of two layers of Fe(111) in the same structure as Au(111) leads to the following dispersion relation for the acoustic magnon mode:

$$E = \hbar\omega = 4\mathrm{J_N S}[4 - \cos(\mathrm{qa_0}) - 3\cos(\frac{1}{2}\mathrm{qa_0})]. \tag{5.1}$$

In the case of 2 ML Fe(110), the acoustic mode of the magnon dispersion relation in the nearest neighbor Heisenberg model is expressed as [19]:

$$E = \hbar\omega = 12\mathrm{J_N S}[1 - \cos(\frac{1}{2}\mathrm{qa_0})]. \tag{5.2}$$

The fitting curves are shown in Fig. 5.1 as solid lines for both Fe(110) and Fe(111) surfaces.

We note that the simple Heisenberg model may not provide the right values for the effective exchange interaction. Nevertheless, it would provide a semi-classical description of the system in a comparative way. The fitting results are J_NS=5.6 meV and 11.6 meV for Fe/Au/W(110) and Fe/W(110), respectively. The effective exchange parameter measured for Fe(111) is smaller than the one of Fe(110). This means that the magnons on the Fe film with (111) surface are softer than the ones on (110) surface.

In this case, we only consider the nearest neighbor Heisenberg model in order to reduce the fit parameters. Considering both the first and the second nearest neighbors, one may obtain unrealistic exchange parameters.

The magnetic exchange interaction of bulk Fe has been calculated by Sabiryanov and Jaswal using a frozen-magnon frozen-phonon scheme [104]. They have predicted smaller values of the exchange constants in bulk fcc Fe with respect to the ones in bulk bcc Fe. The structure of Fe/Au/W(110) is a close-packed structure with (111) surface orientation. As the Fe film grows pseudomorphically on Au(111) film, it is the starting point of the formation of Fe film in fcc phase. However, the structure is a metastable structure and collapses into a bcc phase when the third layer of Fe is grown on top (see section 3.3.1). Interestingly, in the case of ultrathin Co films grown with different surface structures such as fcc [8] and hexagonal close-packed (hcp) [40] structure, the nearest neighbor exchange coupling constant has been found to be the same as the one of the bulk Co.

The exchange parameters are obtained based on the assumption of the free-standing film with perfect bcc(110) and fcc(111) structures. However, in the case of 2 ML Fe(110) grown on W(110), the interlayer distance between two Fe atomic layers is about 1.7 Å, which is much smaller than the one of tungsten (2.24 Å) [103]. In the case of 2 ML Fe(111) on 2 ML Au(111) on W(110), the *average* interlayer distance for different Fe thicknesses is measured by means of IV-LEED experiments as shown in Fig. 3.10. We do not have the information of the individual interlayer distances between different layers. This is due to the fact that by analyzing (00) spot in IV-LEED experiments only an average interlayer distance is obtained. In order to have an access to the individual interlayer distances, one has to do the full analysis of each spot [105, 106]. However, the slightly distorted LEED pattern shown in Fig. 3.10 is an indication that the surface structure is no longer a perfect fcc Fe(111) surface. Therefore, the real distances between the lattice sites are different from the ideal lattice which is the assumption of the simple

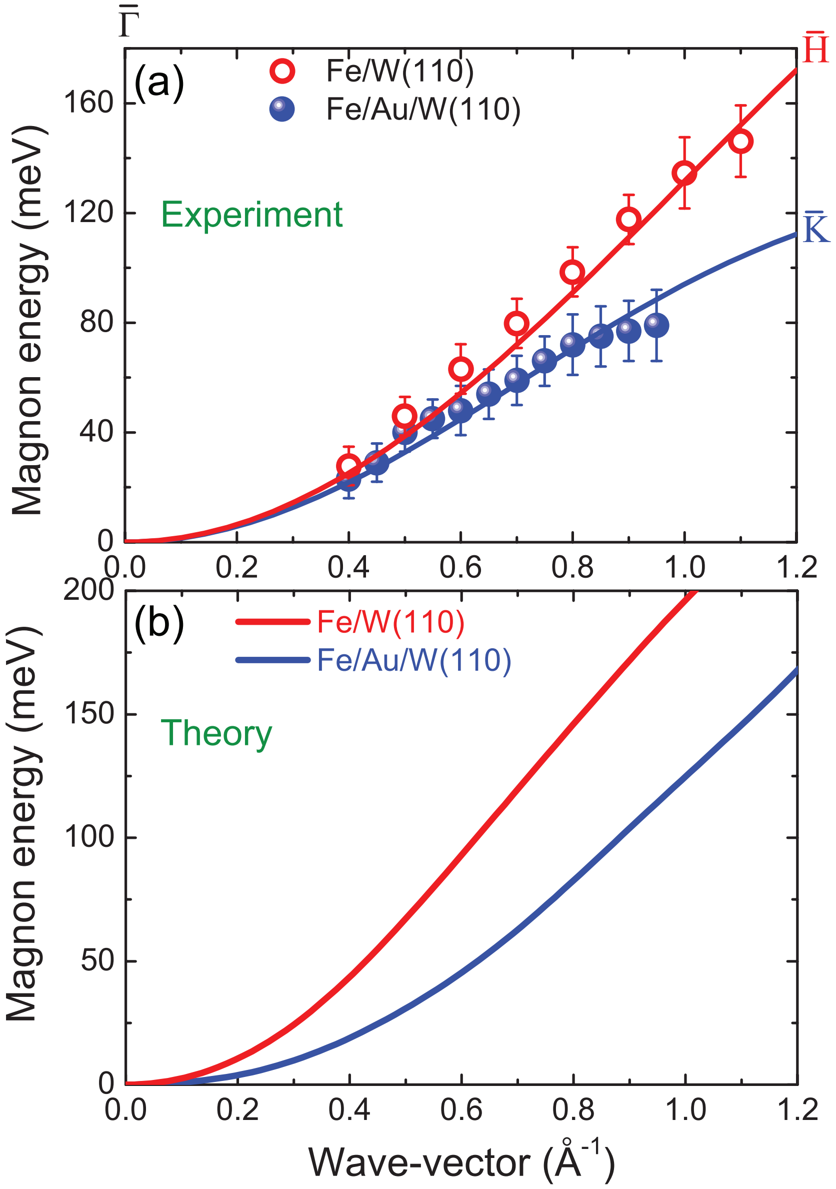

Figure 5.2: (a) The experimental magnon dispersion relation for Fe/W(110) (red open circles) and Fe/Au/W(110) (blue solid circles). The solid lines are the fits based on the nearest neighbor Heisenberg model. (b) The theoretical magnon dispersion relation based on spin dynamics calculations for Fe/W(110) and Fe/Au/W(110) shown as red and blue lines, respectively. Calculations are performed by Arthur Ernst.

Heisenberg model. Since the exchange interaction is sensitive to the distance between neighbors [107], the real exchange constants of the Fe atoms may be different from that obtained by using the simple Heisenberg model.

Furthermore, the magnetic moment of the Fe atoms in the interface layer is reported to be smaller than the one in the surface layer [108]. This is also not considered in this simple model. In order to shed light into the origin of the magnon softening observed for Fe/Au/W(110) structure, we performed first-principles adiabatic spin dynamics calculations based on DFT in collaboration with the colleagues in the theory department at Max Planck Institute of Microstructure Physics.

5.1.2 Description based on the first-principle spin dynamics calculations

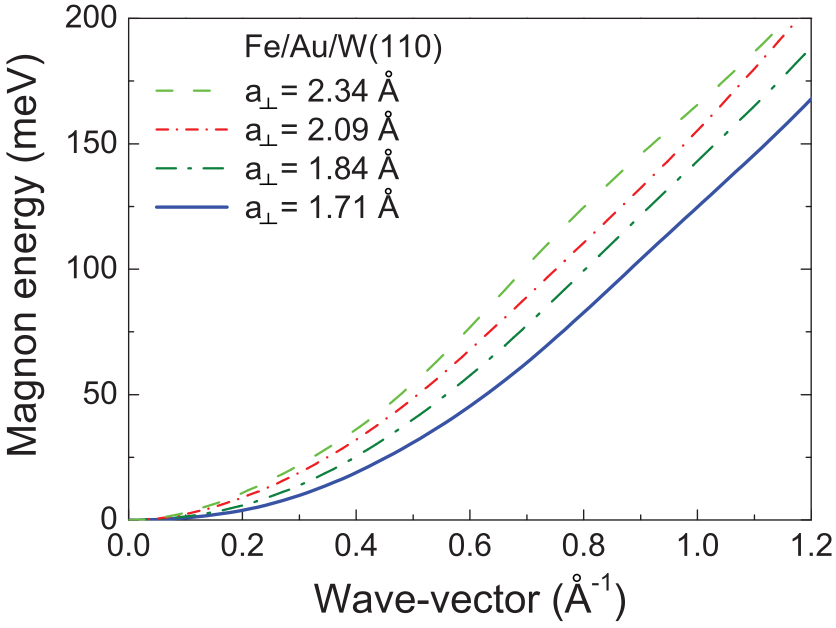

Figure 5.3: The theoretical magnon dispersion relation of Fe/Au/W(110) with different interlayer spacings obtained from spin dynamics calculations. Calculations are performed by Arthur Ernst.

The magnon dispersion relation is calculated for both Fe(111)/Au(111)/W(110) and Fe(110)/W(110) systems. The calculations are performed within the generalized gradient approximation of the DFT [109]. Usually in the adiabatic calculations, the atomic magnetic moments are treated as rigid entities, which precess around the direction of the ferromagnetic ground state. The excitation energies are obtained by means of parameter-free DFT calculations. Within this approach a mapping of the itinerant electron system onto a Heisenberg Hamiltonian is considered. The atomic positions in Fe/Au/W(110) were obtained using the VASP code, well-known for providing accurate total energy and forces [110, 111]. The structural information serves as an input for calculations of electronic and magnetic properties using a self-consistent Green function method, which is specially designed for layered semi-infinite systems [112]. The Heisenberg exchange parameters were determined employing the magnetic force theorem, likewise implemented within the Green function method [113]. The results of the calculations are presented in Fig. 5.2 (b). In the calculation, the Fe(110)/W(110) system is considered as pseudomorphic growth of Fe on W(110) with the relaxed interlayer distance (1.7 Å) [103]. In the case of the Fe(111)/Au(111)/W(110), the Fe film is assumed as pseudomorphic growth on Au(111) with the relaxed interlayer distance, being 1.61 Å. The absolute value of energies is not the same as the measured ones (see Fig. 5.2). For example, at $\Delta K_{||}$=1.0 Å^{-1}, the calculation results in 200 and 110 meV

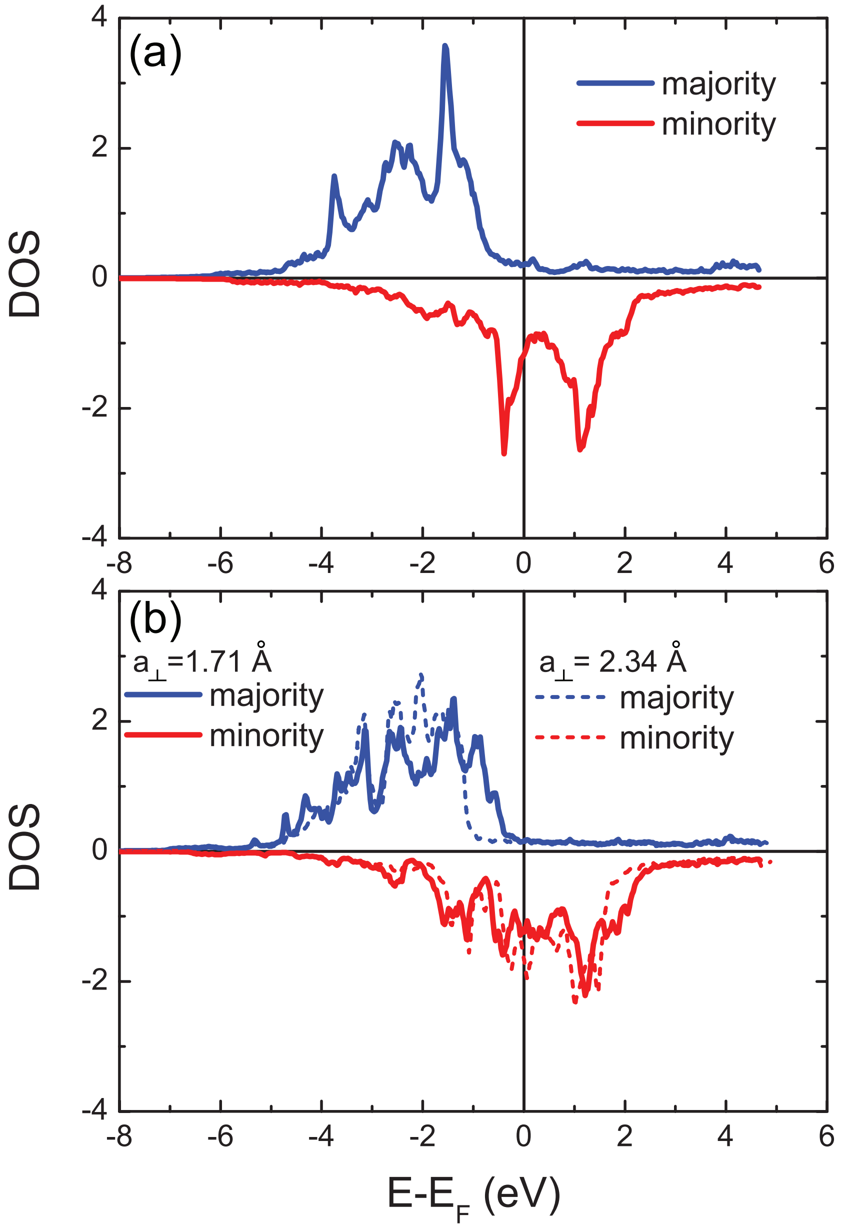

Figure 5.4: Spin-resolved density of states (DOS) calculated by density functional theory for (a) 2 ML Fe/W(110) and (b) 2 ML Fe/2 ML Au/W(110). The blue and red colors represent the DOS for majority and minority electrons, respectively. In (a), the DOS is calculated for the relaxed structure. The solid and dashed lines in (b) represent the DOS for relaxed ($a_\perp = 1.71$ Å) and extended ($a_\perp = 2.34$ Å) structure, respectively. This corresponds to the dashed and solid lines in Fig. 5.3. Calculations are performed by Arthur Ernst.

for Fe(110) and Fe(111), respectively, but the experimental results are 135 and 80 meV. However, the calculated results show the same trend as seen in the experiment. The magnon energies in the case of Fe/Au/W(110) are lower than the ones of Fe/W(110). The observed softening of the magnons in the case of Fe/Au/W(110) with respect to Fe/W(110) manifests the sensitivity of the magnetic exchange interaction of Fe to the change of its lattice structure. We also perform the calculations for the same structure (Fe/Au/W(110)) with different interlayer distances. These calculations reveal that the magnon energies increase when the interlayer distance increases (see Fig. 5.3). If the interlayer distance is 2.34 Å, where the volume of the unit cell is the same as the one in 2 ML Fe/W(110), the magnon dispersion relation is just slightly below the one of Fe/W(110). This indicates that the main contribution of the magnon softening is due to the contraction of the unit cell and changing its volume.

In order to illustrate the origin of the strong dependency of the magnon energies on the interlayer distance, we calculated the density of states (DOS) while changing the interlayer distance. In Fig. 5.4, the spin-resolved DOS calculated by DFT on the topmost Fe layer in Fe/W(110) and in Fe/Au/W(110) structures are shown. The blue color is for majority states and the red one is for minority states. In Fig. 5.4 (b), the solid lines are the DOS for Fe/Au/W(110) with the relaxed structure. The dashed lines are the DOS for Fe/Au/W(110) structure with the extended interlayer spacing. It corresponds to the calculation of the magnon dispersion relation of the dashed line in Fig. 5.3. We observe that the minority spin states do not show a drastic change when changing the interlayer spacing as shown in Fig. 5.4 (b). However, the majority spin states near the Fermi level shift downwards while increasing the interlayer spacing. In simple words, when the splitting of the majority and minority states increases, the energy needed for creation of an electron-hole pair across the Fermi level also increases. A shift downwards from the Fermi level in the majority states leads to an enormous increase of the magnon energies. This fact has a direct consequence on the magnon dispersion relation.

The calculated results of the exchange constants on different atomic sites in Fe/W(110) and Fe/Au/W(110) are presented in Fig. 5.5. The blue and the yellow balls represent the topmost and the second layer of Fe, respectively. The positive values of the exchange parameters are shown in red numbers and the negative ones are shown in blue. For the case of Fe(110) on W(110) the exchange interaction is predominantly positive. Only small negative values can be seen for larger distances away from the origin. In the case of Fe(111)/Au(111)/W(110), large negative exchange constants on some lattice sites close to the origin can be observed. The existence of the negative exchange constants diminishes the overall magnon energies. As it is shown, there is a tendency of an antiferromagnetic coupling between some neighbors in Fe/Au/W(110) system. However, the ground state of the system is ferromagnetic.

For a comparison, we also performed the experiments on the Au/Fe/W(110) system. We find out that the magnon dispersion relation does not change drastically compared to the one in Fe/W(110). It also reveals the importance of the surface structure on the magnon excitations. The Au overlayer does not influence the magnon dispersion relation, but effect the magnon lifetime, which will be discussed in the next section.

In summary, we present the magnon dispersion relation measured on the Fe(111) and Fe(110) surfaces. The softening of the magnons on Fe(111) surface is attributed to the fact that the magnetic interactions in Fe are strongly coupled to the lattice structure. Based on the theoretical calculations, the electronic structure changes while changing the interlayer spacing. These changes have a direct consequence on the magnetic interactions in the system and thereby on the magnon dispersion relation.

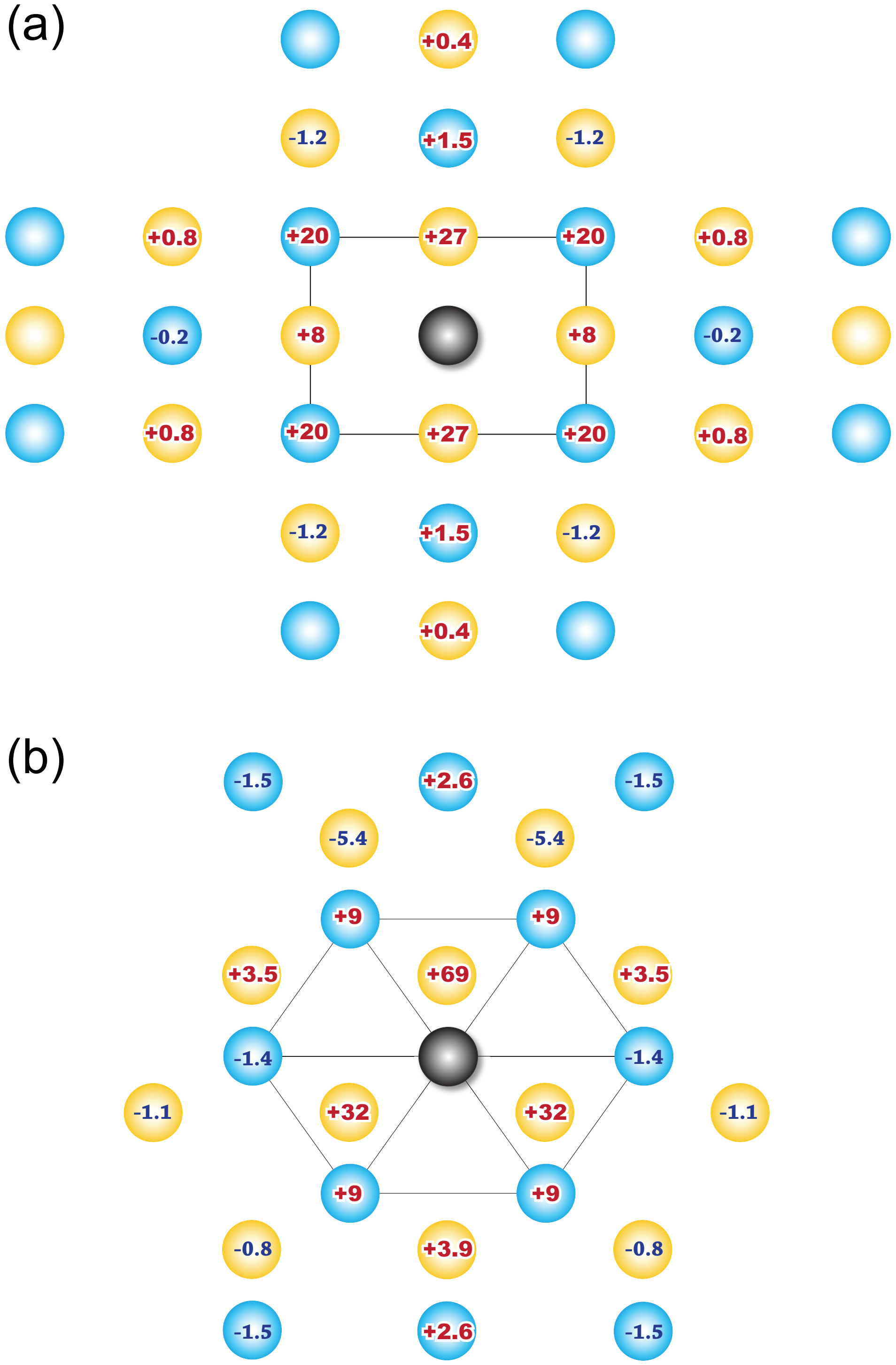
(a)
+0.4
-1.2
+1.5
-1.2
+0.8
+20
+27
+20
+0.8
-0.2
+8
+8
-0.2
+0.8
+20
+27
+20
+0.8
-1.2
+1.5
-1.2
+0.4
(b)
-1.5
+2.6
-1.5
-5.4
-5.4
+9
+9
+3.5
+69
+3.5
-1.4
-1.4
-1.1
+32
+32
-1.1
+9
+9
-0.8
+3.9
-0.8
-1.5
+2.6
-1.5

Figure 5.5: The configuration of the exchange coupling constants in the top 2 Fe layers in (a) Fe/W(110) and (b) Fe/Au/W(110) calculated by DFT. The balls in the figure represent the atom in the lattice. The black one represents the origin. The blue ones are at the first layer, and the yellow ones are at the second layer. The red numbers indicate the positive exchange constants and the blue ones denote the negative values. The unit of the exchange constants is in meV. Calculations are performed by Arthur Ernst.

5.2 The Au/Fe/W(110) system

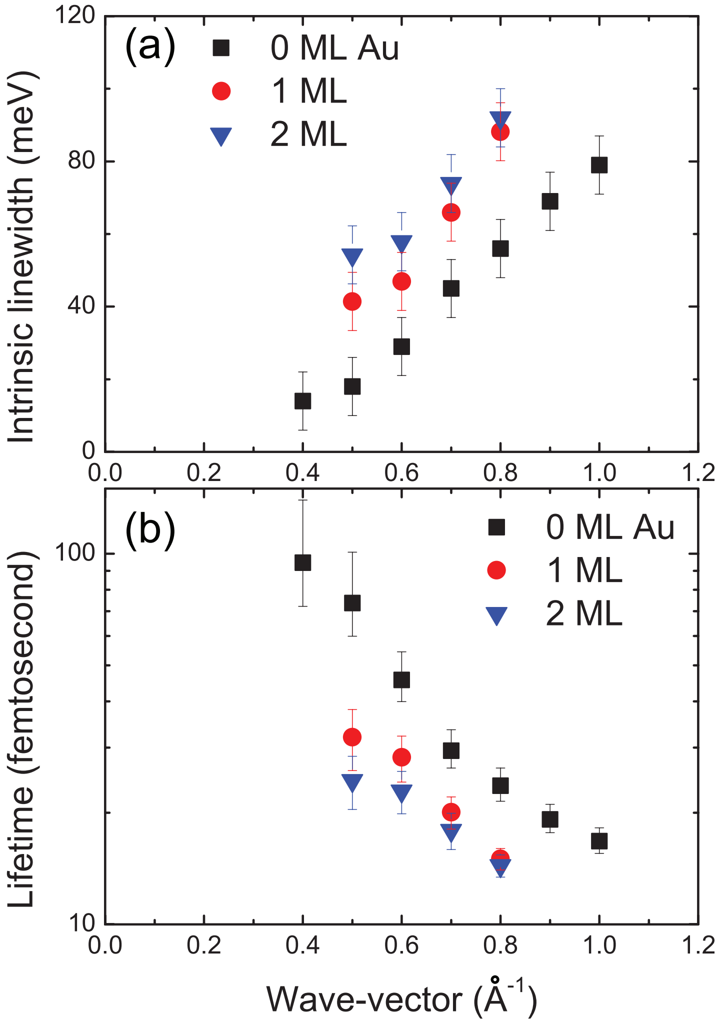

Figure 5.6: (a) The intrinsic linewidth of magnon peaks as a function of the wave-vector transfer obtained on 2 ML Fe/W(110) with 0, 1, and 2 ML Au overlayer. (b) The magnon lifetime as a function of the wave-vector on 2 ML Fe/W(110) with different thicknesses of Au overlayer.

In this section, we discuss the effect of a non-magnetic overlayer on the magnon lifetime excited in a ferromagnetic film. The temporal and spatial properties of magnons in 2 ML Fe/W(110) have been investigated by Zhang, *et al.* [19, 28]. The magnon lifetime is found to be in the range of 10 to 100 femtoseconds depending on the wave-vector. The lifetime for small wave-vectors is longer and decreases as the wave-vector increases (see Fig. 5.6). As we have mentioned in section 4.2, we obtained the SPEEL-spectra on 2 ML Fe/W(110) with different thicknesses of Au overlayer. The width of the difference spectra is getting broader when the thickness of Au is increased. Here, we provide a quantitative analysis of the magnon lifetime at different thicknesses of Au overlayer on 2 ML Fe/W(110).

In the difference spectrum, the excitation peaks give the energy distribution of the magnons. The magnon lifetime can be obtained from the excitation peak through the Fourier transform. However, the measured magnon peaks always include an instrumental response function which broadens the magnon peaks. Therefore, it is assumed that the intrinsic magnon peaks resemble a Lorentzian distribution in the spectra, and the instrumental broadening is a Gaussian distribution. Hence, the magnon peaks can be analyzed by fitting the experimental magnon peaks with a convolution of a Gaussian and a Lorentzian function (Voigt distribution). In the fitting procedure, the full width at half maximum (FWHM) of the instrumental broadening, represented by the Gaussian, is kept constant as 15 meV (the resolution of the experiments). The linewidth of the Lorentzian function gives the intrinsic energy width of the magnons.

In Fig. 5.6 (a), the intrinsic linewidths of magnon peaks are shown as a function of the wave-vector transfers for different thicknesses of Au overlayer on Fe/W(110). It is observed that the linewidth increases when the thickness of Au overlayer increases. As an example, the fit through the data shown in Fig. 4.5 reveals that the intrinsic linewidths at $\Delta K_{||}$=0.6 Å^{-1} are about 28, 47, and 58 meV for 0, 1, and 2 ML of Au overlayer, respectively. The instrumental broadening is about 15 meV. The large broadening indicates that magnons are strongly damped. The magnon lifetime can be obtained from the Fourier transform of the magnon signal. The Fourier transform of a Lorentzian function in energy or frequency domain is an exponential decay in time domain, $\exp(\frac{-t\Gamma}{2\hbar})$, where Γ represents the intrinsic linewidth of the Lorentzian peak in energy and $\hbar$ is the reduced Planck constant. The lifetime of a magnon is the time where the amplitude drops to its e^{-1} value (τ=$2\hbar/\Gamma$).

The magnon lifetime as a function of wave-vector transfers are shown in Fig. 5.6 (b) for n ML Au/2 ML Fe/W(110) (n=0, 1, and 2). Clearly, the magnon lifetime becomes shorter in the presence of a Au overlayer. In addition, the lifetime is getting shorter if the thickness of the overlayer increases (see the data for $\Delta K_{||}$=0.5 Å^{-1} and $\Delta K_{||}$=0.6 Å^{-1}). Finally it shows a saturation behavior. It is observed that this behavior is faster at rather higher wave-vectors, such as $\Delta K_{||}$=0.8 Å^{-1}.

In order to visualize the strong damping effects on the magnons in real time and space, the evolution of the magnon wave packets in n ML Au/2 ML Fe/W(110) is presented in Fig. 5.7. The black solid line is the magnon wave packet propagating on Fe/W(110) with no overlayer. The red dashed and blue dotted lines are the wave packets in Fe films with 1 ML and 2 ML Au overlayer, respectively. Each wave packet in Fig. 5.7 is a product of three components: (i) A moving Gaussian, $\exp[-(x-vt)^2/2\sigma^2]$, representing the motion of the wave packet. σ and τ are the broadening of the wave packet in space and lifetime, respectively. (ii) An exponential decay factor, $\exp(-t/\tau)$, for the evolution of the amplitude in time. (iii) A wave form, $\cos(\Delta K_{||}x-\omega t)$, representing its wavy nature. The velocity of the envelope function, v, is the group velocity of the wave packet, which can be obtained by the slope of the dispersion relation, $v = dE/d\Delta K_{||}$ at $\Delta K_{||}$=0.6 Å^{-1}. Since the magnon energies are not effected by the overlayer as seen in Fig. 4.5, the group velocity is the same for the films with and without overlayer. $\omega = E/\hbar$ is the angular frequency of the wave.

Figure 5.7 demonstrates that the magnons are strongly damped within a few tens of femtoseconds and spatially confined in a few nanometers. We demonstrate that the damping is influenced by the Au overlayer. It has been shown that the Stoner excitations in the surface states play an important role in the damping mechanism [24,

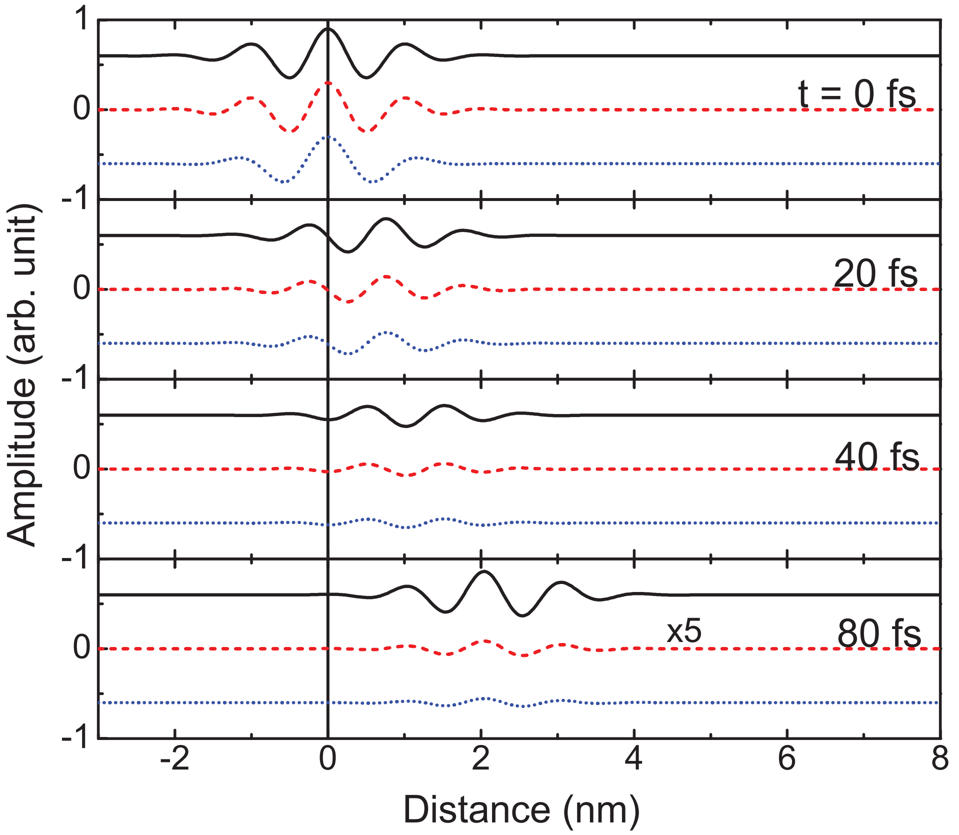

Figure 5.7: A real time and space representation of the magnon wave packets at $\Delta K_{||}$=0.6 Å^{-1} in 2 ML Fe/W(110) with 0 ML (black solid line), 1 ML (red dashed line), and 2 ML (blue dotted line) Au overlayer. The wave packets propagate along the [001]-direction. The amplitudes for the curves at t = 80 fs have been multiplied by a factor of 5.

114, 115]. The strong damping of high wave-vector magnons is regarded as the results of the strong decay of the collective magnons into the available Stoner states near the Fermi level. If the ferromagnetic film is grown on a metallic substrate, due to the strong hybridization of the bands of the ferromagnetic films and the metallic substrate, there are lots of Stoner states available near the Fermi level, which can contribute to the damping. It is reported that the formation of electronic complexes localized at the film-substrate interface leads to hot spots in the Landau maps and enhances the damping [24]. Buczek, *et al.*, have shown clearly the difference between the Landau maps of the free and supported films is dramatic. Similarly, a non-magnetic overlayer on top of the ferromagnetic Fe films may create more hot spots on the maps or enhance the intensity of the spots.

It is also shown that the decay effect may be imagined as the pumping of the spins of the magnetic film into the non-magnetic conductive substrate [65]. The decay of the collective excitations to the Stoner excitations leads to a decrease in the transverse magnetization associated with the spin motion in the ferromagnet. Therefore, the Au overlayer on the 2 ML Fe/W(110) may provide an additional channel or available states for damping from collective excitations into single particle Stoner excitations.

Consequently, the lifetime of the magnons propagating in the Fe films becomes shorter in the presence of Au overlayer.

5.3 The Fe/Ir(001) system

As it was mentioned in section 3.3.2, Fe films with thicknesses up to 10 ML grow pseudomorphically on Ir(001) with a constant in-plane film strain [16, 31, 32]. The room temperature ferromagnetic signal is only observed when the thickness is above 5 ML as presented in section 4.3.1. Here we divide our discussion into three parts. In the first part, the magnon dispersion relation in a typical uniformly strained ferromagnetic film, which was chosen to be 6 ML Fe, is discussed. A simple Heisenberg model is applied to estimate the exchange parameters. A comparison to the spin dynamics calculations is also presented. In the second part, the thickness dependence of the magnon dispersion relation within the uniformly strained region (6-10 ML) is illustrated. In the third part, we comment on the surface acoustic mode in thick Fe(001) films grown on Ir(001) and compare it to the one measured for thick Fe(110) films grown on W(110).

5.3.1 A typical ferromagnetic film: 6 ML Fe/Ir(001)

Starting from Eq. 2.7 and taking 6 layers of bcc Fe with (001) surface orientation, we can numerically calculate the magnon dispersion relation with certain exchange coupling constants (similar to the one demonstrated in section 2.1.1 for the case of 20 ML). Here we assume that the in-plane lattice constant is a_0= 2.72 Å, since the Fe layers grow pseudomorphically on Ir(001) up to 10 ML.

In Fig. 5.8, the experimentally obtained magnon dispersion relation along the $\bar{\Gamma}$-$\bar{\mathrm{M}}$ and $\bar{\Gamma}$-$\bar{\mathrm{X}}$ direction is fitted by using a Heisenberg model. The black open circles are the experimental data and the red solid lines are the fits. In principle, there should be 6 magnon modes in the Heisenberg model since there are 6 layers of Fe. Here only the surface acoustic mode is shown since the SPEELS experiments mainly probe the acoustic surface mode as discussed in section 2.3. First, the experimental data obtained along the $\bar{\Gamma}$-$\bar{\mathrm{M}}$ direction are fitted by the Heisenberg model considering the exchange interaction only between the first and the second nearest neighbors. The resulted exchange coupling constants are J_NS= 4.7 meV for the first nearest neighbors and J_{NN}S=2.8 meV for the second nearest neighbors. As seen in Fig. 5.8, the data along the $\bar{\Gamma}$-$\bar{\mathrm{M}}$ direction are well-fitted. Since the measurements are performed on the films with the same surface orientation, the exchange interaction along different directions should, in principle, be the same. However, the experimental data along the $\bar{\Gamma}$-$\bar{\mathrm{X}}$ direction are away from the fitting curve. The excitation energy obtained by the experiment around $\bar{\mathrm{X}}$-point is around 120 meV which is almost 2 times larger than the calculated curve based on the Heisenberg model.

At the first look, it is surprising that the exchange interaction is not isotropic along different directions. However, we also tried to fit the experimental data along the $\bar{\Gamma}$-$\bar{\mathrm{X}}$ direction. It turned out that the results cannot be well-described by this simple Heisenberg model. This fact may imply that there might be an exotic configuration of the exchange interaction in the system. In this model, we assume that all the

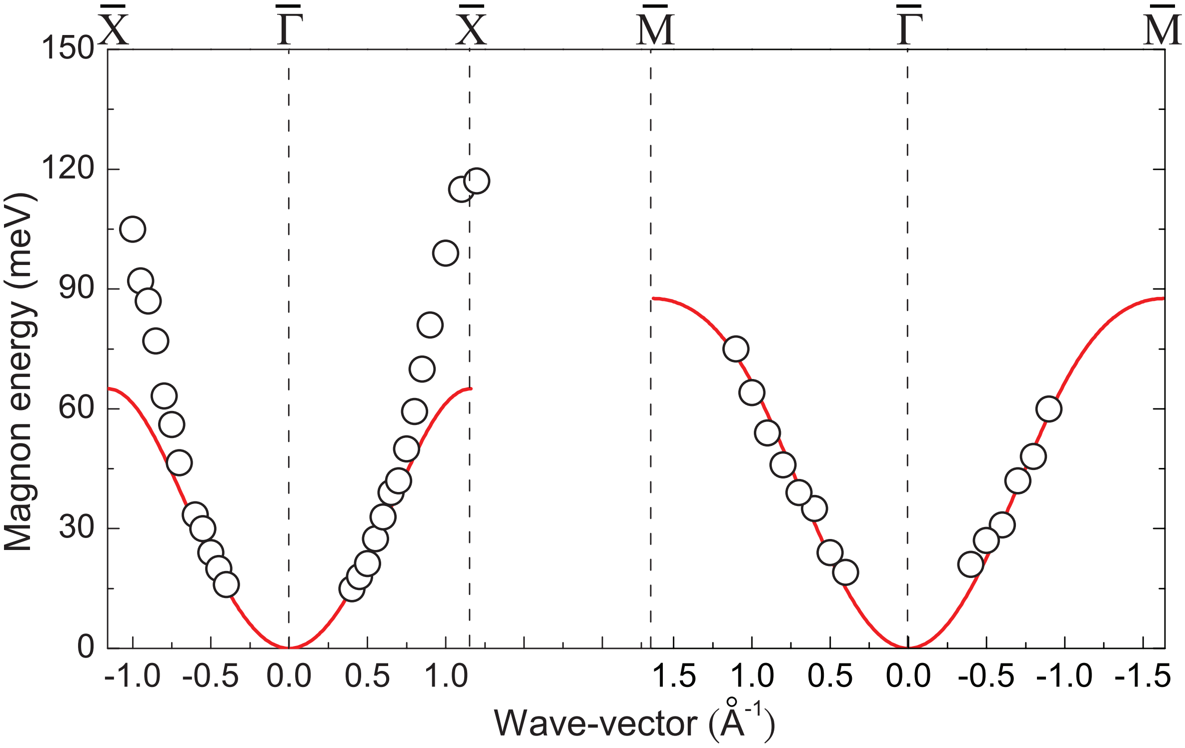

Figure 5.8: The magnon dispersion relation measured on 6 ML Fe/Ir(001) along the $\bar{\Gamma}$-$\bar{\mathrm{M}}$ and the $\bar{\Gamma}$-$\bar{\mathrm{X}}$ direction. The open circles are the experimental data, and the red solid lines are the the fits based on the Heisenberg model. The fitting parameters are: J_NS= 4.7 meV and J_{NN}S=2.8 meV. Here only the acoustic surface mode is shown.

exchange constants within the same distance from the origin are the same including the in-plane exchange couplings and the ones between layers. This may not be true in the real case. In addition, as seen in the literature [16, 31], the Fe films on Ir(001) grow as body-centered tetragonal (bct) structure from 2 ML to 10 ML. The perfect cubic structure is distorted because of the strain induced by the epitaxial growth. Careful structural analysis has been performed by LEED intensity analyses [31]. It has been shown that the ratio of the vertical lattice constant over the in-plane lattice constant is 1.14. An undistorted bcc material has the ratio of 1. We have shown that the exchange interaction is strongly coupled to the lattice structure in section 5.1.2. Therefore, the observed anisotropic dispersion relation might be due to the tetragonally distorted structure.

In order to have a better understanding of the system, we also performed spin dynamics calculations. The calculations are performed for 6 ML Fe on Ir(001) as shown in Fig. 5.9 (a) by the red line. The input parameters (interatomic distances) for the red line are taken from the experimental results by means of the IV-LEED analysis (1.60 Å) [31]. The results of calculations for 6 ML Fe are in good agreement with the experimental results. However, small deviations can be observed, which might be due to different reasons: (i) The relativistic effect is not considered in the theory. (ii) The interatomic distance for our case might be slightly different than the one of the literature value, since the Fe film is grown on a reconstructed Ir substrate rather than

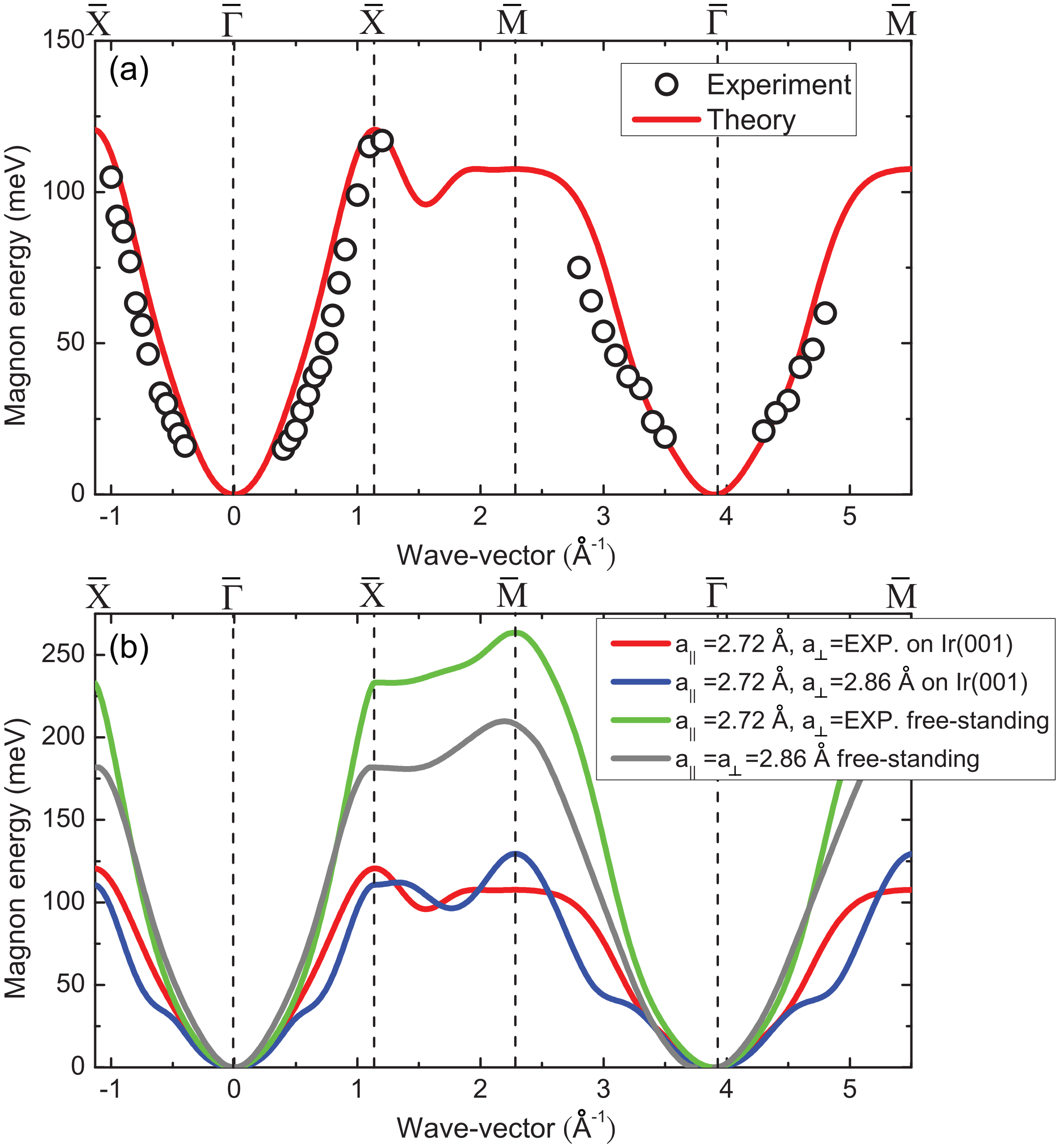

Figure 5.9: The experimental (open circles) and theoretical (solid lines) magnon dispersion relation of 6 ML Fe/Ir(001) over the whole surface Brillouin zone. Calculations are performed for four different structures: (*i*) A pseudomorphically grown Fe film on Ir(001) with the vertical lattice constant obtained by IV-LEED measurements [31] (red line), (*ii*) A pseudomorphically grown Fe film on Ir(001) with the vertical lattice constant of the bulk (blue line), (*iii*) free-standing Fe film with the in-plane and vertical lattice constants obtained by experiments (green line), (*iv*) free-standing Fe film with the in-plane and vertical lattice constants of the bulk Fe (gray line). Calculations are performed by Arthur Ernst.

a (1×1) surface.

The magnon energy at $\bar{\mathrm{X}}$-point is higher than the one at $\bar{\mathrm{M}}$-point in the calculation. Although there is no experimental data close to the $\bar{\mathrm{M}}$-point, a lower energy at $\bar{\mathrm{M}}$-point is still expected in the experiment, which is in agreement with the calculation. It is noted that a higher magnon energy at $\bar{\mathrm{M}}$-point is predicted in the Heisenberg model, which is in contradiction to the experimental results.

In order to find out the role of the hybridization with the substrate and the atomic relaxation on the magnon dispersion relation, we perform other calculations for three different cases. In Fig. 5.9 (b), the blue line presents the calculated results using the in-plane lattice constant the same as the nearest neighbor atomic distance of Ir(001) (2.72 Å) but using Fe bulk value (2.86 Å) as the vertical lattice constant. A characteristic change is observed. Close to the $\bar{\mathrm{X}}$-point, the energies are lower than the red curve, but larger near the $\bar{\mathrm{M}}$-point. It indicates that the tetragonal distortion indeed plays an important role in magnon dispersion relation. The green line presents the calculation for the free-standing 6 ML Fe with the same input parameters as the red one (experimental values). There is a huge enhancement on the energy for the free-standing film. This demonstrates that the effect of hybridization of the Fe film and the Ir substrate on the magnon dispersion relation is of major importance. The gray line represents the calculation for a free-standing film with the in-plane and vertical lattice constants of the bulk Fe. The magnon energies are lower than the one of the distorted free-standing Fe film (green curve), but much larger than the ones of the Fe films grown on Ir substrate (red and blue curves). It is noted that the magnon energies at the $\bar{\mathrm{X}}$-point are all lower than the one at the $\bar{\mathrm{M}}$-point for blue, green, and gray curves. Only in the case where all experimental parameters are taken into consideration, one can have a good agreement between the experimental data and the calculations. Therefore, not only the strain induced distorted lattice structure but also the hybridization of the Fe films and the Ir substrate influence the magnetic excitations in the Fe film.

In order to visualize the effects of tetragonal distortion and the hybridization with the substrate on the magnetic exchange interaction within the Fe film, the exchange coupling constants calculated for each atomic sublattice of 6 ML Fe grown on Ir(001) are shown in Fig. 5.10. Figure 5.10 (a) and (b) show the exchange couplings on the Fe surface from the top, and (c) and (d) show the ones on the Fe/Ir interface from the bottom. The black ball represents the origin. Since the surface structure is bcc(001), the first nearest neighbors are the 4 atoms at $(\frac{a_0}{2}, \frac{a_0}{2}, \frac{a_\perp}{2})$, which are at the second layer. a_0 is the in-plane lattice constant, and $a_\perp$ is the vertical lattice constant. The first nearest neighbors show a strong ferromagnetic coupling. The second nearest neighbors in the same layer at $(a_0, 0, 0)$ show a weak ferromagnetic coupling. The most interesting point is that the neighbors at larger distances like $(2a_0, 0, 0)$ shows a relative stronger antiferromagnetic coupling than the closer sites in the same layer (an antiferromagnetic coupling is preferred within the layers).

Since the Fe films grown on Ir(001) are tetragonally distorted, the distance between $(0, 0, -a_\perp)$ to the origin site is 0.48 Å longer than the one of $(a_0, 0, 0)$. Hence, the respective exchange couplings are totally different. The in-plane second nearest neighbors $(a_0, 0, 0)$ are weakly ferromagnetically coupled, but the vertical second nearest ones $(0, 0, -a_\perp)$ are strongly ferromagnetically coupled as shown in Fig. 5.10 (b) and (d). This small deviation from a perfect bcc lattice in the perpendicular direction results in

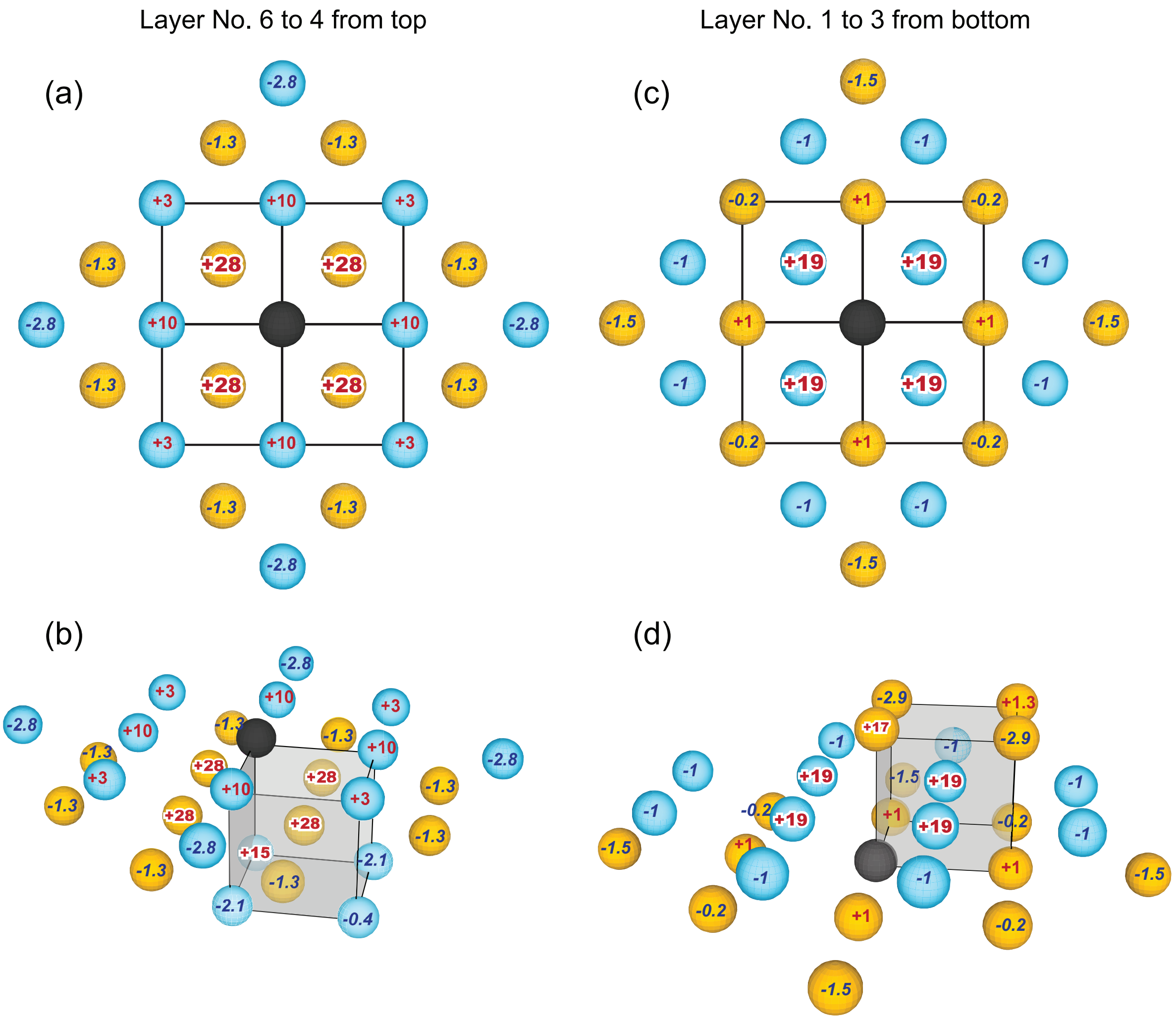
Layer No. 6 to 4 from top
Layer No. 1 to 3 from bottom
(a)
-2.8
-1.3
+3
+10
+28
-1.3
(c)
-1.5
-1
-0.2
+1
+19
(b)
+15
-2.1
-0.4
(d)
-2.9
+1.3
+17
-0.2
+1

Figure 5.10: The configuration of the exchange coupling constants close to (a)-(b) the surface and (c)-(d) the interface of 6 ML Fe grown on Ir(001) calculated by DFT. Layer No.1 to No.6 denotes the layer from the interface to the surface. The blue balls represent the No. 2, 4, and 6 layers and the yellow balls are located in the No. 1, 3, and 5 layers. For simplicity, only two layers are sketched in top views (a) and (c). The black ball represents the origin site. The red numbers indicate the positive exchange constants and the blue ones denote the negative values. The unit of the exchange constants is in meV. The unit cell is shown by the square in the top view and the cube in the side view. Calculations are performed by Arthur Ernst.

a large effect on the exchange interaction. This is another evidence that the magnetic interactions in Fe are strongly coupled to the lattice structure. However, the role of the substrate should not be neglected.

Although the couplings at most of the sites in Fig. 5.10 are antiferromagnetic, due to the strong ferromagnetic coupling on the first nearest neighbors and the vertical second nearest neighbors, the net exchange coupling is still ferromagnetic. Hence, in this particular system, only considering the first and the second nearest neighbors is not sufficient to well-describe the exchange interaction in the overall thin films. Comparing the configuration of the exchange couplings on the surface and the interface, both have tendency to be antiferromagnetic coupling in the plane, but more sublattices close to the interface between Fe and Ir show antiferromagnetic coupling. It suggests that 1 ML Fe on Ir(001) might be an antiferromagnet. However, the relativistic effects are not considered in this calculation. It has been shown in theoretical calculation that including relativistic corrections in the case of ultrathin (1 to 4 ML) Fe films on Ir(001) leads to the appearance of complex non-collinear spin structures [33]. Since in this thickness regime, the results of our experiments show no spin contrast as shown in section 4.3.4, we do not have access to verify the results of this calculation. However, without considering the relativistic effects, the theoretical results fit quite well to the experiment. It suggests that the relativistic effects may not influence the magnon energies too much when the thickness is thicker than 5 ML.

In summary, by comparing the experimental and theoretical results, the strain induced by the pseudomorphic growth and the hybridization of the Fe film and Ir substrate are both crucial on the magnetic excitations in ultrathin Fe films on Ir(001).

5.3.2 Thickness dependence within the uniformly strained region: 6-10 ML Fe

The magnon dispersion relation does not change drastically when the thickness of the Fe film changes from 6 to 10 ML (the thickness ranges where the films are grown epitaxially and are uniformly strained). In the case of Fe films on W(110), a nonmonotonic thickness dependence of magnon energy has been reported [25]. Combining the experimental and theoretical investigations, it is found that the hybridization with the substrate and the atomic relaxation in the film are both crucial for description of the experimental results. In that work, the atomically relaxed structure has been first considered, and then the case of atomically unrelaxed structure has been also calculated for comparison. It turned out that the relaxed one has a maximum of energy at 2 ML and gradually decreases, which is in the best agreement with the experimental observations. On the other hand, it is noticed that for the unrelaxed structure the magnon energy drastically increases from 1 to 2 ML but varies just slightly beyond 2 ML. The results of calculations for such cases are in agreement with the experiments on epitaxially grown Fe films on Ir(001). We observe a similar magnon dispersion relation on the uniformly strained Fe films from 6 to 10 ML.

In Fig. 5.11, the magnon dispersion relation on the 6 ML to 10 ML Fe films grown on Ir(001) along the $\bar{\Gamma}$-$\bar{\mathrm{X}}$ direction is shown. The symbols are the experimental data and the solid lines are the calculated results. The magnon dispersion relation obtained from the experiments is similar within this thickness range. The theoretical results also

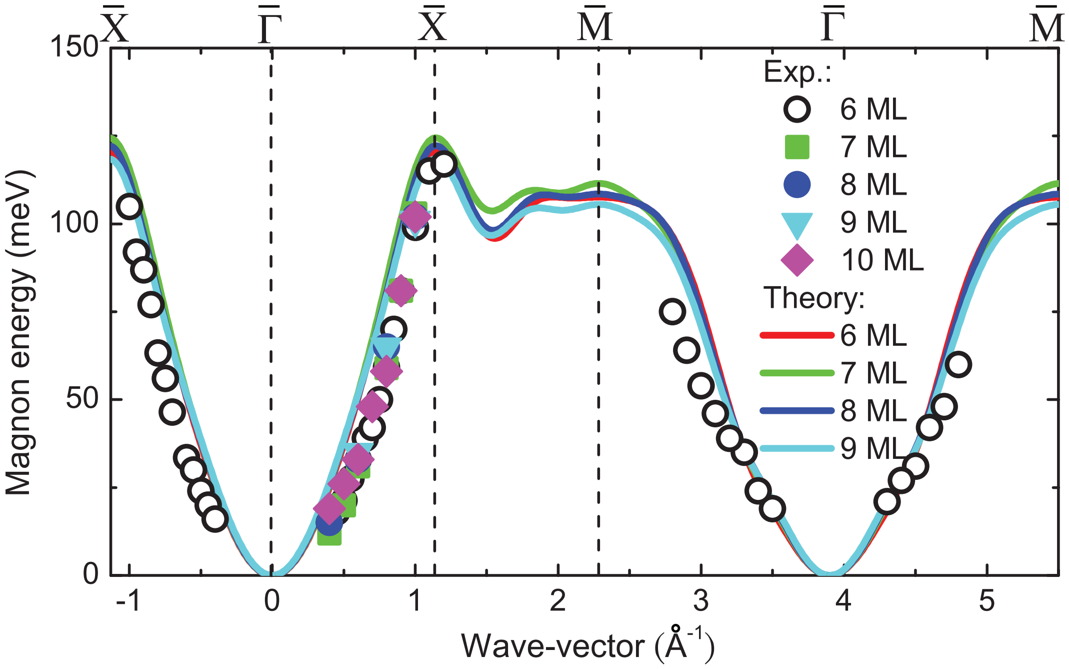

Figure 5.11: The magnon dispersion relation of 6 ML to 10 ML Fe grown on Ir(001) obtained at room temperature. The symbols represent the experimental data. The solid lines show the calculation results. Calculations are performed by Arthur Ernst.

show the same trend with only small differences at the zone boundary in the range within our experimental error. The hybridization with the substrate and the tetragonal distortion in the film lead to an exotic configuration of the exchange coupling. Since Fe film is uniformly strained up to 10 ML, the structure stays the same. Therefore, a similar magnon dispersion relation from 5 to 10 ML is expected.

We also observe the change of the magnon dispersion relation when the Fe films on Ir(001) are relaxed. As shown in Fig. 5.12, the dispersion relation of 27 ML Fe on Ir(001) is different from the one of the uniformly strained films. Since the structure of the Fe film is changed to a bulk-like film when the film is relaxed, the exchange interaction in the film is also changed. In addition, the film is thick enough and the effects caused by the substrate/film interface can be neglected. Hence, the magnon dispersion relation is thus changed to the surface acoustic mode measured on a bulk-like Fe film, which will be discussed in the following.

5.3.3 A typical relaxed ferromagnetic film: 27 ML Fe

As shown in section 4.3.6, the magnon dispersion relation measured on the relaxed Fe films grown on Ir(001) is investigated. It is observed that the magnon dispersion relation on the relaxed films is different than the uniformly strained films (see Fig. 4.14). It is also illustrated that the dispersion relation measured within the pseudomorphic growth region cannot be well-described by the simple Heisenberg model, which only the first and the second nearest neighbors are considered. However, the magnon dispersion relation measured on the thick Fe films on Ir(001) can be well-fitted by the simple Heisenberg model. In Fig. 5.13, the magnon dispersion relation obtained on 27 ML Fe on Ir(001)

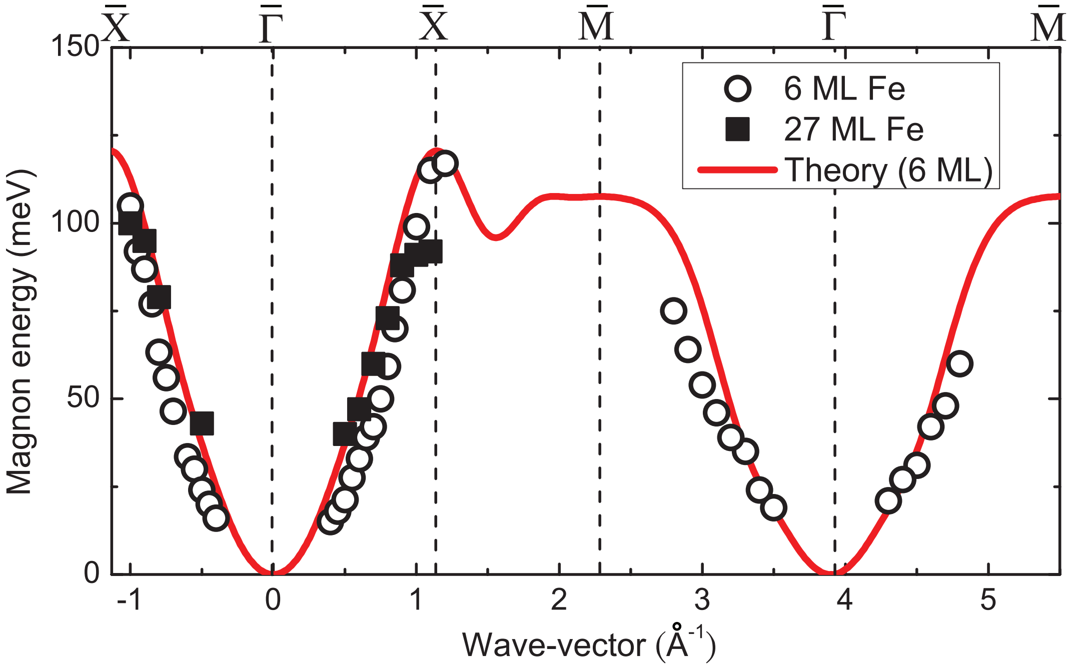

Figure 5.12: The magnon dispersion relation of a thick Fe films (27 ML) grown on Ir(001) are shown as black squares. For comparison, the experimental and theoretical results of 6 ML Fe are also presented. Calculations are performed by Arthur Ernst.

and 24 ML Fe on W(110) [19] is shown as black squares and red circles, respectively. The magnon excitations in Fe films on Ir(001) are probed along the $\bar{\Gamma}$-$\bar{X}$ direction and the ones in Fe films on W(110) are probed along the $\bar{\Gamma}$-$\bar{H}$ direction. The zone boundary is at 1.10 $Å^{-1}$ for the $\bar{\Gamma}$-$\bar{X}$ direction and at 1.64 $Å^{-1}$ for the $\bar{\Gamma}$-$\bar{H}$ direction. Two solid lines in Fig. 5.13 are the acoustic surface mode in the Heisenberg model, where only the first and the second nearest neighbors are considered. Interestingly, dispersion relation in both cases can be well-fitted by using the same exchange parameters. The exchange constants for the first nearest neighbors and the second nearest neighbors are 6.8 meV and 4.1 meV, respectively. In both cases, the effective exchange parameters are smaller than the ones expected for the bulk Fe according to the experimental data obtained from inelastic neutron scattering experiments [116]. This suggests that the effective exchange parameters at the surface of an Fe film is smaller than the ones in the bulk Fe. It has been predicted by Turek based on the Heisenberg model that the layer-resolved on-site exchange parameter of bcc Fe has a minimum at the top surface layer [117]. The reduction of the exchange couplings in the top surface layer is due to the reduced coordination. However, it is in contrast to the results of ab initio electronic structure calculations, which predict that the interlayer exchange couplings derived from total-energy differences are enhanced at the surface [117].

The observation of the same effective exchange parameters on the thick Fe films grown on different substrate (W and Ir) is in agreement with previous discussion. Since we mainly probe the surface magnons, the thickness of the Fe film is large enough to neglect the effects caused by the film/substrate interface. It should be noted that the surface orientations of the Fe film is different between these two cases. Turek, *et al.*,

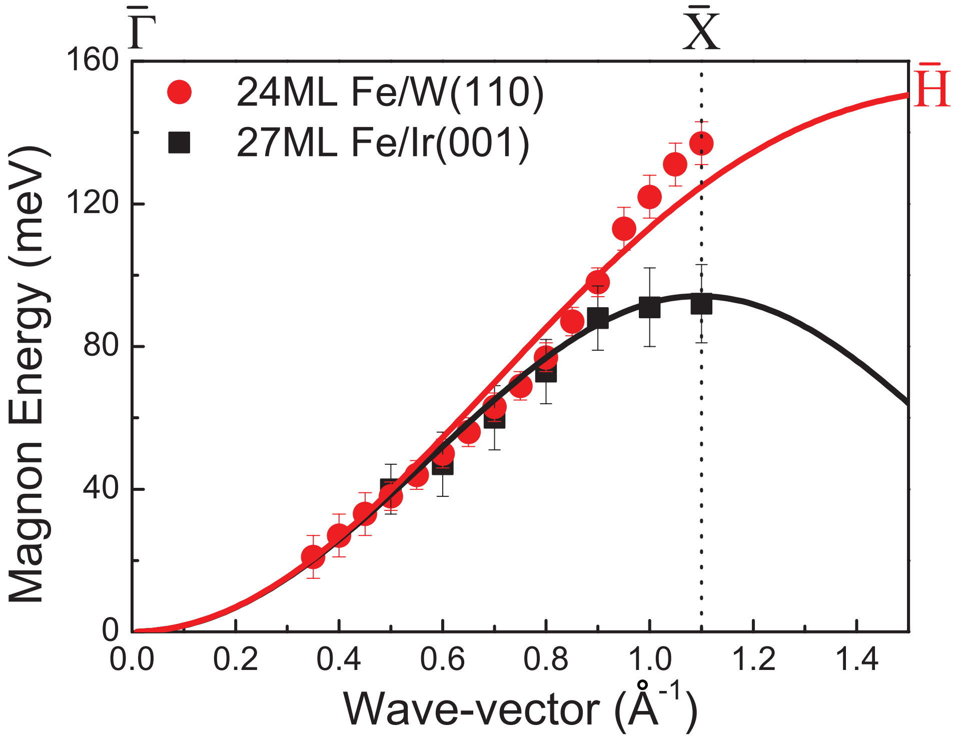

Figure 5.13: The magnon dispersion relation obtained on thick Fe films grown on different substrates with different surface orientations. The red circles are the experimental data measured on 24 ML Fe(110) grown on W(110) [19]. The black squares are the results obtained on 27 ML Fe(001) on Ir(001) as shown in section 4.3.6. In the Heisenberg model, the dispersion relation can be well described by the surface mode using the same exchange parameters. The fit parameters are $J_N S = 6.8$ meV and $J_{NN} S = 4.1$ meV.

have also calculated the layer-resolved magnetic moments and the on-site exchange parameters on Fe(001) and Fe(110) surfaces [117]. It is found that the magnetic moment on the top surface layer of Fe(001) is larger than the one on Fe(110) surface. However, the exchange parameter on the surface layer of Fe(001) is smaller than the one on Fe(110). Since we can only extract the quantity JS from our experimental results, a reduction of J may compensate the enhancement of S, and vice versa. Therefore, a similar JS would be expected on Fe(001) and Fe(110) surfaces.

The magnon dispersion relation of thick Fe films with different orientation show similar energies at low wave-vector region, i.e. lower than 0.7 Å^{-1}. The energies start to deviate at about 0.8 Å^{-1}. This observation is in agreement with the Heisenberg model which predicts similar excitation energies for bcc Fe at low wave-vectors. The difference appears close to the zone boundary. For bulk Fe, this has been observed by Mook, *et al.*, by using inelastic neutron scattering [11]. In their measurements, the magnon dispersion relation is found to be similar for three main symmetry directions in bulk Fe up to 0.7 Å^{-1}. At high wave-vectors, the magnon intensity is too low to be recognized. The low intensity is ascribed to the magnon damping into the Stoner continuum. In our experiments, the dispersion relation is measured up to 1.1 Å^{-1} in both directions. Although the magnons at high wave-vectors are strongly damped, the data quality is still very good and the energy difference between two directions for $\Delta K_{||} > 0.9\text{Å}^{-1}$ is clearly visible.

Chapter 6

Conclusions and outlook

In this work, we present our experimental results on high wave-vector magnon excitations in Fe(111) and Fe(001) thin films by means of spin-polarized electron energy loss spectroscopy.

- In order to investigate how the magnon dispersion relation changes when the lattice structure changes, a metastable phase of Fe composed of a 2 ML Fe film with (111) surface orientation grown on 2 ML Au(111)/W(110) is probed. The results are compared to the one of the Fe(110)/W(110) system. It is observed that the magnon energies in Fe(111)/Au(111)/W(110) are smaller than the ones in Fe(110)/W(110). The softening of the magnons in Fe(111) surface is due to the fact that the magnetic interactions in Fe are strongly coupled to the lattice structure. In order to find out the origin of the strong dependency of the magnon energies on the lattice structure, first-principles adiabatic spin dynamics calculations based on density-functional theory are performed. It is found that the electronic structure is changed by changing the interlayer spacing and the configuration of atoms within the unit cell. The main contribution of the magnon softening is due to the contraction of the Fe unit cell and changing its volume. These changes have a direct consequence on the electronic structure and thereby on the magnetic interactions in the system, which then modify the magnon dispersion relation.

- The effect of a non-magnetic overlayer on the magnon lifetime excited in a ferromagnetic film is investigated in the Au/Fe(110)/W(110) system. It is observed that the intrinsic linewidth of the magnon peaks increases when the thickness of Au overlayer increases. At the wave-vector of $\Delta K_{||}$=0.6 Å^{-1}, the intrinsic linewidth is increased from 28 to 47 meV by adding 1 ML of Au overlayer. The Au overlayer on the 2 ML Fe/W(110) provide an additional channel for damping of collective excitations into single particle Stoner excitations. It is noted that the magnon dispersion relation in Au/Fe(110)/W(110) is very similar to the one in Fe(110)/W(110). Only the magnon lifetime is effected by the overlayer.

- To investigate the Fe(001) surface the Fe(001)/Ir(001) system is chosen. The first experimentally measured magnon dispersion relation on Fe(001) surface within the whole surface Brillouin zone and along different symmetry directions is measured. The results show that the magnon dispersion relation along different symmetry directions is different, suggesting an exotic configuration of the exchange interaction. The experimental results are in agreement with the theoretical spin dynamics calculations. Based on our theoretical calculations, we conclude that the strained induced distortion and the hybridization of the film and substrate are both crucial to understand the magnetic excitation in this system.

- The magnon dispersion relation is measured on different thicknesses of Fe film where the film is uniformly strained (5-10 ML). It is found that the magnon dispersion relation does not change drastically when the film thickness is changed within the uniformly strained region.
- The SPEELS measurements are performed in the vicinity of the thickness of room temperature ferromagnetic order. The room temperature ferromagnetic hysteresis loop only appears when the Fe thickness is above 5 ML. While going across the thickness of room temperature ferromagnetic order, the magnon energy stays nearly constant. But the magnon intensity strongly decreases when the ferromagnetic signal disappears.
- The magnon dispersion relation of a relaxed thick (27 ML) Fe(001) film grown on Ir(001) is compared to the one of a thick (24 ML) Fe(110) film grown on W(110). For both surfaces, the magnon dispersion relation shows similar energies at low wave-vectors and starts to deviate close to the zone boundary. However, the dispersion relation measured on two systems can be well-fitted by using the same exchange parameters and taking the Heisenberg model. It may imply that if the Fe films are bulk-like films, the exchange interaction at the surface is independent of the substrate. The influence of the substrate can be neglected.

In this study, the magnon dispersion relation in an Fe(111) surface was investigated in a metastable 2 ML Fe(111)/Au(111)/W(110) system. It is worthwhile to probe the magnons in an Fe film grown on a crystal with (111) surface orientation for a comparison to these results. However, such measurements may require the sensitivity to the out-of-plane magnetization direction. The magnon dispersion relation in an ultrathin film has not been probed in film with an out-of-plane magnetization. If it is possible, it would allow one to investigate the mechanism of the magnetic excitation in out-of-plane magnetized films.

A better understanding of the additional damping effect for a Au overlayer on top of a ferromagnetic film is still missing. One way would be performing the experiments on a ferromagnetic film grown on an insulating substrate.

The mystery of the magnetic properties in the first 4 ML of Fe grown on Ir(001) is still a puzzle, since no ferromagnetic signal is observed in the SPEELS spectra below 4 ML. We hope that the presented work will stimulate further experimental and theoretical investigation in the field of magnetic excitations.

Bibliography

[1] F. Bloch, Z. Phys. **61**, 206 (1930).

[2] C. Herring and C. Kittel, Phys. Rev. **81**, 869 (1951).

[3] B. Heinrich and J. A. C. Bland, *Ultrathin Magnetic Structures II*, Springer Verlag, Berlin Heidelberg New York, 1994.

[4] M. Farle, Rep. Prog. Phys. **61**, 755 (1998).

[5] P. A. Grünberg, Prog. Surf. Sci. **18**, 1 (1985).

[6] B. Hillebrands, P. Baumgart, and G. Güntherodt, Phys. Rev. B **36**, 2450 (1987).

[7] M. Plihal, D. L. Mills, and J. Kirschner, Phys. Rev. Lett. **82**, 2579 (1999).

[8] R. Vollmer, M. Etzkorn, P. S. Anil Kumar, H. Ibach, and J. Kirschner, Phys. Rev. Lett. **91**, 147201 (2003).

[9] W. X. Tang, Y. Zhang, I. Tudosa, J. Prokop, M. Etzkorn, and J. Kirschner, Phys. Rev. Lett. **99**, 087202 (2007).

[10] B. N. Brockhouse, Phys. Rev. **106**, 859 (1957).

[11] H. A. Mook and R. M. Nicklow, Phys. Rev. B **7**, 336 (1973).

[12] A. Schreyer, T. Schmitte, R. Siebrecht, P. Bödeker, H. Zabel, S. H. Lee, R. W. Erwin, C. F. Majkrzak, J. Kwo, and M. Hong, J. Appl. Phys. **87**, 5443 (2000).

[13] T. Balashov, A. F. Tak*á*cs, W. Wulfhekel, and J. Kirschner, Phys. Rev. Lett. **97**, 187201 (2006).

[14] C. L. Gao, A. Ernst, G. Fischer, W. Hergert, P. Bruno, W. Wulfhekel, and J. Kirschner, Phys. Rev. Lett. **101**, 167201 (2008).

[15] T. Balashov, *Inelastic scanning tunneling spectroscopy: magnetic excitations on the nanoscale*, Dissertation, Universität Karlsruhe (TH), 2009.

[16] Z. Tian, *Magnetoelastic Coupling in Ferromagnetic Films and Surface Stress Studies on Ir(100)*, Dissertation, Universität Halle-Wittenberg, 2008.

[17] R. Vollmer, M. Etzkorn, P. S. Anil Kumar, H. Ibach, and J. Kirschner, J. Magn. Magn. Mater. **272-276**, 2126 (2004).

[18] R. Vollmer, M. Etzkorn, P. S. Anil Kumar, H. Ibach, and J. Kirschner, Thin Solid Films **464-465**, 42 (2004).

[19] Y. Zhang, *High wave vector spin waves in ultrathin Fe films on W(110) studied by spin-polarized electron energy loss spectroscopy*, Dissertation, Universität Halle-Wittenberg, 2008.

[20] J. Prokop, W. X. Tang, Y. Zhang, I. Tudosa, T. R. F. Peixoto, K. Zakeri, and J. Kirschner, Phys. Rev. Lett. **102**, 177206 (2009).

[21] L. Udvardi and L. Szunyogh, Phys. Rev. Lett. **102**, 207204 (2009).

[22] A. T. Costa, R. B. Muniz, S. Lounis, A. B. Klautau, and D. L. Mills, Phys. Rev. B **82**, 014428 (2010).

[23] A. Bergman, A. Taroni, L. Bergqvist, J. Hellsvik, B. Hjörvarsson, and O. Eriksson, Phys. Rev. B **81**, 144416 (2010).

[24] P. Buczek, A. Ernst, and L. M. Sandratskii, Phys. Rev. Lett. **106**, 157204 (2011).

[25] Y. Zhang, P. Buczek, L. Sandratskii, W. X. Tang, J. Prokop, I. Tudosa, T. R. F. Peixoto, K. Zakeri, and J. Kirschner, Phys. Rev. B **81**, 094438 (2010).

[26] Y. Zhang, P. A. Ignatiev, J. Prokop, I. Tudosa, T. R. F. Peixoto, W. X. Tang, K. Zakeri, V. S. Stepanyuk, and J. Kirschner, Phys. Rev. Lett. **106**, 127201 (2011).

[27] K. Zakeri, Y. Zhang, J. Prokop, T.-H. Chuang, N. Sakr, W. X. Tang, and J. Kirschner, Phys. Rev. Lett. **104**, 137203 (2010).

[28] K. Zakeri, Y. Zhang, T.-H. Chuang, and J. Kirschner, Phys. Rev. Lett. **108**, 197205 (2012).

[29] M. R. Vernoy and H. Hopster, Phys. Rev. B **68**, 132403 (2003).

[30] T. Komesu, G. D. Waddill, and J. G. Tobin, J. Phys.: Condens. Matter **18**, 8829–8836 (2006).

[31] V. Martin, W. Meyer, C. Giovanardi, L. Hammer, K. Heinz, Z. Tian, D. Sander, and J. Kirschner, Phys. Rev. B **76**, 205418 (2007).

[32] Z. Tian, D. Sander, and J. Kirschner, Phys. Rev. B **79**, 024432 (2009).

[33] A. Deák, L. Szunyogh, and B. Ujfalussy, Phys. Rev. B **84**, 224413 (2011).

[34] D. L. Mills, in *Surface excitations*, edited by M. Aranovich and R. Loudon, page Chap. 3, Elesevier Science Publishers B. V., 1984.

[35] W. Heisenberg, Z. Phys. **27**, 411 (1926).

[36] M. G. Cottam and A. N. Slavin, in *Linerar and nonlinear spin waves in Magnetic films and superlattices*, edited by M. Aranovich and R. Loudon, page Chap. 1, World Scientific, Singapore New Jersey London Hong Kong, 1994.

[37] J. Stöhr, *Magnetism, From Fundamentals to Nanoscale Dynamics*, Springer series in solid-state sciences 152, Springer Verlag, Berlin Heidelberg, 2006.

[38] C. Kittel, *Introduction to Solid State Physics, seventh edition*, John Wiley and Sons Inc., New York Chichester Brisbane Toronto Singapore, 1996.

[39] M. Etzkorn, *Spin waves with high energy and momentum in ultrathin Co-films studied by spin-polarized electron energy loss spectroscopy*, Dissertation, Universität Halle-Wittenberg, 2005.

[40] M. Etzkorn, P. S. Anil Kumar, W. X. Tang, Y. Zhang, and J. Kirschner, Phys. Rev. B **72**, 184420 (2005).

[41] R. Vollmer, M. Etzkorn, P. S. Anil Kumar, H. Ibach, and J. Kirschner, J. App. Phys. **95**, 7435 (2004).

[42] E. C. Stoner, Proc. Roy. Soc. A **154**, 656 (1936).

[43] E. C. Stoner, Proc. Roy. Soc. A **165**, 372 (1938).

[44] J. C. Slater, Phys. Rev. **52**, 198 (1937).

[45] D. H. Martin, *Magnetism in solids*, MIT Press, Cambrigde, 1967.

[46] C. Herring, in *Exchange interactions among itinerant electrons*, edited by G. T. Rado and H. Suhl, page Vol. IV of Magnetism, Academic Press, New York London, 1966.

[47] D. R. Penn and P. Apell, Phys. Rev. B **38**, 5051 (1988).

[48] J. Kirschner, D. Rebenstorff, and H. Ibach, Phys. Rev. Lett. **53**, 698 (1984).

[49] J. Kirschner and S. Suga, Surf. Sci. **178**, 327 (1986).

[50] J. Kirschner and E. Langenbach, Solid State Commun. **66**, 761 (1988).

[51] H. Tang, M. Plihal, and D. L. Mills, J. Magn. Magn. Mater. **187**, 23 (1998).

[52] C. Herring, Phys. Rev. **87**, 60 (1952).

[53] D. M. Edwards, Proc. R. Soc. A **235**, 305 (1962).

[54] D. M. Edwards and E. P. Wohlfarth, J. phys. et radium **20**, 136 (1959).

[55] D. M. Edwards, Proc. R. Soc. A **300**, 373 (1967).

[56] D. M. Edwards and J. A. Hertz, J. Phys. F. **3**, 2191 (1973).

[57] D. M. Edwards and M. A. Rahman, J. Phys. F. **8**, 1501 (1978).

[58] D. M. Edwards and R. B. Muniz, J. Phys. F. **15**, 2339 (1985).

[59] D. L. Mills, Phys. Rev. B **34**, 6099 (1986).

[60] M. P. Gokhale and D. L. Mills, Phys. Rev. B **49**, 3880 (1994).

[61] M. Plihal and D. L. Mills, Phys. Rev. B **58**, 14407 (1998).

[62] R. B. Muniz, A. T. Costa, and D. L. Mills, J. Phys.: Condens. Matter **15**, S495 (2003).

[63] R. B. Muniz and D. L. Mills, Phys. Rev. B **66**, 174417 (2003).

[64] A. T. Costa, R. B. Muniz, and D. L. Mills, Phys. Rev. B **68**, 224435 (2003).

[65] A. T. Costa, R. B. Muniz, and D. L. Mills, Phys. Rev. B **74**, 214403 (2006).

[66] P. Buczek, A. Ernst, P. Bruno, and L. M. Sandratskii, Phys. Rev. Lett. **102**, 247206 (2009).

[67] P. Buczek, A. Ernst, and L. M. Sandratskii, Phys. Rev. Lett. **105**, 097205 (2010).

[68] P. Buczek, A. Ernst, and L. M. Sandratskii, Phys. Rev. B **84**, 174418 (2011).

[69] S. Y. Savrasov, Phys. Rev. Lett. **81**, 2570 (1998).

[70] R. Feder, *Polarised electrons in surface physics*, World Scientific, Singapore, 1985.

[71] H. Ibach and D. L. Mills, *Electron energy loss spectroscopy and surface vibrations*, Academic Press, New York London Paris, 1982.

[72] J. Kessler, Polarized Electrons, in *Springer series on Atoms and Plasmas, secound edition*, edited by G. Ecker, P. Lambropoulos, and H. Walther, Springer Verlag, Berlin Heidelberg New York Tokyo, 1985.

[73] J. Kirschner, Polarized Electrons at Surfaces, in *Springer Tracts in Modern Physics, vol. 106*, Springer Heidelberg, 1985.

[74] J. Kirschner, Inelastic electron scattering by ferromagnets, in *Polarized Electrons in Surface Physics*, edited by R. Feder, World Scientific, Singapore, 1985.

[75] J. Kirschner, Phys. Rev. Lett. **55**, 973 (1985).

[76] A. Taroni, A. Bergman, L. Bergqvist, J. Hellsvik, and O. Eriksson, Phys. Rev. Lett. **107**, 037202 (2011).

[77] J. Rajeswari, H. Ibach, and C. M. Schneider, Deutschen Physikalischen Gesellschaft **MA 49.2**, Berlin (2012).

[78] H. Ibach, J. Electron Spectrosc. Relat. Phenom. **64/65**, 819 (1993).

[79] H. Ibach, M. Balden, and S. Lehwald, J. Chem. Soc., Faraday Trans. **92**, 4771 (1996).

[80] H. Ibach, D. Bruchmann, R. Vollmer, M. Etzkorn, P. S. Anil Kumar, and J. Kirschner, Rev. Sci. Instrum. **74**, 4089 (2003).

[81] D. T. Pierce and F. Meier, Phys. Rev. B **13**, 5484 (1976).

[82] P. Drescher and *et al.*, Appl. Phys. A **63**, 203 (1996).

[83] R. Feder and J. Kirschner, Surf. Sci. **103**, 75 (1981).

[84] M. Plihal, D. L. Mills, H. J. Elmers, and U. Gradmann, Phys. Rev. B **51**, 8193 (1995).

[85] D. Venus, S. Cool, and M. Plihal, Surf. Sci. **446**, 199 (2000).

[86] K. Zakeri, T. Peixoto, Y. Zhang, J. Prokop, and J. Kirschner, Surf. Sci. **604**, L1–L3 (2010).

[87] B. Voigtlaender, G. Meyer, and N. M. Amer, Surface Science Letters **255**, L529–535 (1991).

[88] J. A. Stroscio, D. T. Pierce, R. A. Dragoset, and P. N. First, J. Vac. Sci. Technol. A **10(4)**, 1981 (1992).

[89] T. Allmers and M. Donath, New Journal of Physics **11**, 103049 (2009).

[90] T. Allmers and M. Donath, Phys. Rev. B **81**, 0644055 (2010).

[91] J. Xu, A. Howson, P. Hucknall, B. J. Hickey, R. Venkataraman, C. Hammond, M. J. Walker, and D. Greig, J. Appl. Phys. **81**, 3908 (1997).

[92] O. Toulemonde, V. Petrov, A. Nait Abdi, and J. P. Bucher, J. Appl. Phys. **95**, 6565 (2004).

[93] E. Bauer, H. Poppa, G. Todd, and P. R. Davis, J. Appl. Phys. **48**, 3773 (1977).

[94] R. Zdyb, A. Pavlovska, and E. Bauer, J. Phys.: Condens. Matter **21**, 314012 (2009).

[95] R. Zdyb, T. O. Mentes, A. Locatelli, M. A. Nino, and E. Bauer, Phys. Rev. B **80**, 184425 (2009).

[96] K. Heinz, G. Schmidt, L. Hammer, and K. Mueller, Phys. Rev. B **32**, 6214 (1985).

[97] L. Hammer, W. Meier, A. Klein, P. Landfried, A. Schmidt, and K. Heinz, Phys. Rev. Lett. **91**, 156101 (2003).

[98] J. Zarestky and C. Stassis, Phys. Rev. B **35**, 4500 (1987).

[99] M. Kottcke and K. Heinz, Surf. Sci. **376**, 352 (1997).

[100] H. Ibach, J. Rajeswari, and C. M. Schneider, Rev. Sci. Instrum. **82**, 123904 (2011).

[101] H. Ibach and J. Rajeswari, J. Electron Spectrosc. Relat. Phenom. **185**, 61–70 (2012).

[102] D. Sander, A. Enders, and J. Kirschner, Europhys. Lett. **45(2)**, 208 (1999).

[103] H. L. Meyerheim, D. Sander, R. Popescu, J. Kirschner, P. Steadman, and S. Ferrer, Phys. Rev. B **64**, 045414 (2001).

[104] R. F. Sabiryanov and S. S. Jaswal, Phys. Rev. Lett. **83**, 2062 (1999).

[105] J. B. Pendry, *Low Energy Electron Diffraction*, Academic Press, New York, 1974.

[106] M. A. Van Hove, W. H. Weinberg, and C.-M. Chan, *Low-Energy Electron Diffraction Experiment, Theory and Surface Structure Determination*, Springer-Verlag, Berlin, 1986.

[107] M. Pajda, J. Kudrnovský, I. Turek, V. Drchal, and P. Bruno, Phys. Rev. B **64**, 174402 (2001).

[108] X. Qian and W. Hübner, Phys. Rev. B **60**, 16192 (1999).

[109] J. P. Perdew, K. Burke, and M. Ernzerhof, Phys. Rev. Lett. **77**, 3865 (1996).

[110] G. Kresse and J. Hafner, Phys. Rev. B **49**, 14251 (1994).

[111] G. Kresse and J. Furthmüller, Phys. Rev. B **54**, 11169 (1996).

[112] M. Luders, A. Ernst, W. M. Temmerman, Z. Szotek, and P. J. Durham, J. Phys.: Condens. Matter **13**, 8587 (2001).

[113] A. I. Liechtenstein, M. I. Katsnelson, V. P. Antropov, and V. A. Gubanov, J. Magn. Magn. Mater. **67**, 65 (1987).

[114] T. Balashov, T. Schuh, A. F. Takacs, A. Ernst, S. Ostanin, J. Henk, I. Mertig, P. Bruno, T. Miyamachi, S. Suga, and W. Wulfhekel, Phys. Rev. Lett. **102**, 257203 (2009).

[115] A. A. Khajetoorians, S. Lounis, B. Chilian, A. T. Costa, L. Zhou, D. L. Mills, J. Wiebe, and R. Wiesendanger, Phys. Rev. Lett. **106**, 037205 (2011).

[116] J. W. Lynn, Phys. Rev. B **11**, 2624 (1975).

[117] I. Turek, J. Kudrnovský, G. Bihlmayer, and P. Weinberger, Czechoslovak Journal of Physics **53**, 81 (2003).

Acknowledgments

I would like to extend my sincere gratitude to my supervisor, Prof. Dr. Jürgen Kirschner, for giving me an opportunity to be a member of MPI in Halle and for his valuable suggestions, kind support, and warm encouragement during my stay. I truly benefit a lot from his attitude to the scientific research.

I would also like to express my thanks to Dr. Khalil Zakeri Lori for his continuous guidance and training throughout this work. I have learned a lot from him.

Many thanks to Dr. Yu Zhang for the fruitful discussions and countless suggestions for experiments, data analysis, and some ways of interpretation within my thesis. He also helps me a lot for the life in Halle.

Special thanks to my wife, Liang-Chen Wei, for coming along from Taiwan, staying with me and giving me mental support and technical assistance in many figures within this work.

I would like to thank Bi-Lin Ho, Eric Yau, Dr. Cheng-Tien Chiang, and Dr. Ping Yu for the warm help in many aspects of living in Germany.

I am also grateful to the colleagues, Y.-J. Chen, Dr. H.J. Qin, Dr. Y. Meng, Dr. A. Ernst, Prof. Dr. W. Keune, Dr. Z. Tian, M. Dabrowski, Dr. Z. Wei, Dr. M. Takada, Dr. H. Oka, C.-H. Li, and Dr. K. Tao for the pleasant collaboration and discussion.

I would like to show my appreciation to the coordinators of the International Max Planck Research School, Dr. C. Winkler, Dr. K. Boldyreva, Ms. M. Santo, and Dr. A. Ernst, for their assistance during my study.

I wish to thank Mr. H. Engelhard and the colleagues in the electronic and mechanical workshops for the high-quality technical support.

I appreciate Ms. D. Röder and the colleagues in the administration office, Ms. K. Pohlink, Ms. B. Frankenstein, Ms. A. Schneider, Ms. A. Amm and Ms. M. Witzig for their assistance in several administrative manners.

Last but not least, thanks also to my family and friends in Taiwan. Their encouragement is one of the source of my power to face difficulties and the pressure.

Erklärung an Eides statt

Hiermit erkläre ich, dass ich die vorliegende Dissertation

High wave-vector magnon excitations in ultrathin Fe(111) films grown on Au/W(110) and Fe(001) films grown on Ir(001)

selbständig und ohne fremde Hilfe verfasst und keine anderen als die von mir angegebenen Quellen und Hilfsmittel benutzt habe. Die den benutzten Werken wörtlich oder inhaltlich entnommenen Stellen sind als solche kenntlich gemacht.
Ich erkläre, dass ich mich früher nicht um den Doktorgrad beworben habe.

Halle, den 16.08.2012

Tzu-Hung Chuang

Curriculum vitae

First Name	Tzu-Hung
Family Name	Chuang
Date of Birth	August 20, 1982
Place of Birth	Taipei, Taiwan
Nationality	Taiwan
E-mail	thchuang@mpi-halle.mpg.de

EDUCATION

Sep. 2000 - Jun. 2004	National Chiao-Tung University (Hsinchu, Taiwan) Department of Electro-Physics Bachelor of Science
Sep. 2004 - Jul. 2006	National Taiwan University (Taipei, Taiwan) Institute of Electronics Engineering Master of Science
Jan. 2008 - Jun. 2009	Academia Sinica (Taipei, Taiwan) Institute of Atomic and Molecular Sciences Research Assistant
Since Jul. 2009	Max Planck Institute of Microstructure Physics and Martin-Luther-Universität Halle-Wittenberg Ph. D. candidate (Supervisor: Prof. Dr. Jürgen Kirschner)

Tzu-Hung Chuang

Halle (Saale), August 2012